
# Dynamic Effective Elastic Constants for Perforated Plates with Square or Triangular Penetration Patterns

DL Kaap

August 1997

UWFDM-1035

FUSION TECHNOLOGY INSTITUTE

UNIVERSITY OF WISCONSIN

MADISON WISCONSIN

# Dynamic Effective Elastic Constants for Perforated Plates with Square or Triangular Penetration Patterns

DL Kaap

Fusion Technology Institute
University of Wisconsin
1500 Engineering Drive
Madison, WI 53706

http://fti.neep.wisc.edu

August 1997

UWFDM-1035

# Dynamic Effective Elastic Constants for Perforated Plates with Square or Triangular Penetration Patterns

by

**Dustin Lamont Kaap**

A thesis submitted in partial fulfillment of the requirements for the degree of

**MASTER OF SCIENCE**

(Mechanical Engineering)

at the

**UNIVERSITY OF WISCONSIN – MADISON**

1997

# Abstract

Quantifying mechanical response characteristics of perforated plate structures supports the design of products such as heat exchangers, injection nozzles, sieves and sound suppressors. The size and pattern of regular perforations influence a plate's flexural stiffness. For static applications, widely accepted design guidelines exist. In these procedures replacing the plate's elastic modulus by an artificial or effective modulus accommodates the average decrease in stiffness. Similar procedures do not exist for the dynamic design of perforated plates. This thesis addresses the issue, reporting results for natural frequencies and mode shapes for common configurations. Uniform square or triangular patterns of identical circular holes were modeled for square plates with outer edges either all simply supported (hinged) or all clamped. Finite element methods were used, first to verify established static effective stiffnesses, and then to analyze vibrational characteristics. It was found that frequencies calculated using static effective stiffnesses do not correlate well with the FEM dynamic results. These discrepancies are quantified and new dynamic effective stiffnesses are proposed. In addition, experimental results are included which substantiate the FEM data.

# Acknowledgments

I want to thank my advisor Professor Roxann Engelstad for her guidance and encouragement throughout the course of my research. As deeply involved in her work as she is, she has had time to share her involvement and enthusiasm as a researcher, which has inspired and motivated me. I sincerely believe that the most valuable part of my education was the opportunity to participate as a member of her lab, which she maintains as a leading-edge finite element modeling and analysis facility.

I also want to extend a very special thanks to Professor Edward Lovell for his very important involvement in my graduate studies. I never doubted that Professor Lovell would be available. His knowledge in the area of structural mechanics is phenomenal and my respect for him as an expert in his area continues to grow. I also must say that the humor we have shared was a pleasant outlet for stress and frustration.

Outside of my academic work there was Dr. Frederick Elder who always showed a keen interest in my endeavors. It was his advice as an engineer and as a friend that inspired me to complete this thesis and to find a job. Over the past two years Dr. Elder has remained a solid fixture in my life because he is a man of his word and for that alone he deserves thanks.

To my Dad I am forever indebted. Keith Kaap is not only well respected in his career, working as a professional ethics consultant for lawyers, but he is well respected by me for giving everything he had to make my life a success. As a UW graduate himself, my father understood the challenges I faced and he never missed an opportunity to support my activities or to sit at my side as we cheered on our fellow Badgers. Thank you "Bup."

Computer support for this research has been provided in part by the National Science Foundation.

# Table of Contents

Abstract ..... i
Acknowledgments ..... ii
Table of Contents ..... iii
List of Figures ..... vi
List of Tables ..... xii
List of Symbols ..... xiii
Chapter 1 ..... 1
Introduction ..... 1
1.1 Background ..... 1
1.2 General Approach ..... 2
1.3 Thesis Outline ..... 2
Chapter 2 ..... 4
Previous Investigations on Perforated Plates ..... 4
2.1 Introduction ..... 4
2.2 Perforation Geometry and Terminology ..... 6
2.3 History of Perforated Plates – Static ..... 7
2.3.1 Loading Orientation ..... 9
2.3.2 Thick to Thin Transition Range ..... 10
2.3.3 Numerical and Experimental Data ..... 11
2.4 History of Perforated Plates – Modal ..... 13
2.5 References ..... 16
Chapter 3 ..... 20
Specific Application for Perforated Plates and Shells ..... 20
3.1 Introduction ..... 20
3.2 Nuclear Fusion Chamber ..... 20
3.3 References ..... 24

Chapter 4 ..... 26
Finite Element Benchmark ..... 26
4.1 Introduction ..... 26
4.2 Solid Plate Theory ..... 26
4.2.1 Thin Plate Theory ..... 26
4.2.2 Classical Plate Theory – Static Analysis ..... 26
4.2.3 Classical Plate Theory – Modal Analysis ..... 28
4.3 Solid Plate Analysis ..... 30
4.3.1 Geometric Modeling and Meshing ..... 30
4.3.2 Nodal Loading ..... 33
4.3.3 Finite Element Results ..... 34
4.4 Perforated Plate Theory ..... 38
4.5 Perforated Plate Analysis ..... 38
4.5.1 Geometric Modeling and Meshing ..... 38
4.5.2 Nodal Loading ..... 40
4.5.3 Finite Element Results ..... 41
4.6 References ..... 42
Chapter 5 ..... 44
Dynamic Behavior of Perforated Plates ..... 44
5.1 Dynamic Effective Elastic Constants ..... 44
5.1.1 Simply Supported Plate with Square Penetration Pattern ..... 45
5.1.2 Clamped Plate with Square Penetration Pattern ..... 50
5.1.3 Simply Supported Plate with Triangular Penetration Pattern ..... 55
5.2.4 Clamped Plate with Triangular Penetration Pattern ..... 60
5.2 Poisson's Ratio ..... 65
5.3 Number of Perforations ..... 67
5.4 Plate Thickness ..... 68
5.5 Material Density ..... 69
5.6 References ..... 71

Chapter 6 ..... 72
Experimental Modal Analysis ..... 72
6.1 Plate Specimens and Plate Fixture ..... 72
6.2 Procedure for Impulse Testing ..... 76
6.3 Procedure for Optical Vibrometer Testing ..... 77
6.4 Resonant Frequency Results ..... 80
6.5 Mode Shape Results ..... 84
6.6 References ..... 85
Chapter 7 ..... 86
Summary and Conclusions ..... 86

# List of Figures


Fig. 2.1. Heat exchanger with cutaway view showing tube sheet ..... 5

Fig. 2.2. Tube sheet from heat exchanger ..... 5

Fig. 2.3. Geometry for square perforation pattern ..... 6

Fig. 2.4. Geometry for triangular perforation pattern ..... 7

Fig. 2.5. Variation of Sampson effective elastic modulus with thickness for a plate in bending ($\nu = 0.50$) ..... 10

Fig. 2.6. Variation of Sampson effective Poisson's ratio with thickness for a plate in bending ($\nu = 0.50$) ..... 11

Fig. 2.7. Static effective stiffness, $D^*$, versus ligament efficiency for simply supported plate with a square perforation pattern ..... 12

Fig. 2.8. Static effective stiffness, $D^*$, versus ligament efficiency for simply supported plate with a triangular perforation pattern ..... 12

Fig. 2.9. Variation in frequency with hole size for a simply supported, square plate. The frequency parameter is a function of Poisson's ratio ..... 14

Fig. 2.10. Variation in frequency with hole size for a clamped square plate. The frequency parameter is a function of Poisson's ratio ..... 14

Fig. 2.11. Variation in critical hole ratio with Poisson's ratio for both clamped and simply supported plates ..... 15

Fig. 2.12. Illustration of mechanisms for strain energy reduction and mass reduction effects on frequency of plate ..... 15

Fig. 3.1. Diagram of nuclear reactions – fusion vs. fission ..... 20

Fig. 3.2. Diagram showing four steps of the ICF process ..... 21

Fig. 3.3. View of the laser and target area building for NIF, the world's most powerful neodymium laser system. The $1-billion facility is 200 m × 85 m ..... 22

Fig. 3.4. Enlarged view looking into NIF's target area with the spherical target chamber located at the center of the diagram ..... 22
Fig. 3.5. NIF target chamber ..... 23
Fig. 3.6. Light Ion Microfusion Facility ..... 23
Fig. 3.7. Perforated cylindrical target chamber from LMF ..... 24
Fig. 4.1. Schematic of simply supported plate with uniform edge moments ..... 27
Fig. 4.2. Mode shapes for simply supported square plate, generated with the numerical software Mathematica® ..... 29
Fig. 4.3. Solid square plate model meshed with ANSYS® ..... 32
Fig. 4.4. Deflection contours for consistent nodal loading using full plate model. Edges are simply supported ..... 33
Fig. 4.5. Consistent nodal loading for 4-node and 8-node elements ..... 34
Fig. 4.6. Mesh convergence for static loading of solid plate ..... 35
Fig. 4.7. Mesh convergence for fundamental mode of solid plate ..... 35
Fig. 4.8. Mesh convergence for mode 4 (1,3) of solid plate ..... 36
Fig. 4.9. Discrete mode shapes generated in ANSYS® ..... 37
Fig. 4.10. Square and triangular pattern perforated plate models meshed with ANSYS® ..... 40
Fig. 4.11. Deflection contours for consistent nodal loading using perforated plate model. Edges are simply supported ..... 40
Fig. 4.12. Mesh convergence for static loading of plate perforated with square pattern and meshed with 4-node element (ANSYS® SHELL63) ..... 41
Fig. 4.13. Mesh convergence for static loading of plate perforated with triangular pattern and meshed with 4-node element (ANSYS® SHELL63) ..... 42
Fig. 5.1. Effective stiffness for square simply supported plate with a square perforation pattern ($\nu = 0.20$) ..... 45

Fig. 5.2. Effective stiffness for square simply supported plate with a square perforation pattern ($\nu = 0.30$) ..... 46

Fig. 5.3. Effective stiffness for square simply supported plate with a square perforation pattern ($\nu = 0.45$) ..... 46

Fig. 5.4. ANSYS® output for square simply supported plates with square perforation patterns ($\nu = 0.20$, $P = 2.0$) ..... 47

Fig. 5.5. ANSYS® output for square simply supported plates with square perforation patterns ($\nu = 0.30$, $P = 2.0$) ..... 48

Fig. 5.6. ANSYS® output for square simply supported plates with square perforation patterns ($\nu = 0.45$, $P = 2.0$) ..... 49

Fig. 5.7. Effective stiffness for square clamped plate with a square perforation pattern ($\nu = 0.20$) ..... 50

Fig. 5.8 Effective stiffness for square clamped plate with a square perforation pattern ($\nu = 0.30$) ..... 51

Fig. 5.9. Effective stiffness for square clamped plate with a square perforation pattern ($\nu = 0.45$) ..... 51

Fig. 5.10. ANSYS® output for square clamped plates with square perforation patterns ($\nu = 0.20$, $P = 2.0$) ..... 52

Fig. 5.11. ANSYS® output for square clamped plates with square perforation patterns ($\nu = 0.30$, $P = 2.0$) ..... 53

Fig. 5.12. ANSYS® output for square clamped plates with square perforation patterns ($\nu = 0.45$, $P = 2.0$) ..... 54

Fig. 5.13. Effective stiffness for square simply supported plate with a triangular perforation pattern ($\nu = 0.20$) ..... 55

Fig. 5.14. Effective stiffness for square simply supported plate with a triangular perforation pattern ($\nu = 0.30$) ..... 56

Fig. 5.15. Effective stiffness for square simply supported plate with a triangular perforation pattern ($\nu = 0.45$) ..... 56
Fig. 5.16. ANSYS® output for square simply supported plates with triangular perforation patterns ($\nu = 0.20$, $P = 2.0$) ..... 57
Fig. 5.17. ANSYS® output for square simply supported plates with triangular perforation patterns ($\nu = 0.30$, $P = 2.0$) ..... 58
Fig. 5.18. ANSYS® output for square simply supported plates with triangular perforation patterns ($\nu = 0.45$, $P = 2.0$) ..... 59
Fig. 5.19. Effective stiffness for square clamped plate with a triangular perforation pattern ($\nu = 0.20$) ..... 60
Fig. 5.20. Effective stiffness for square clamped plate with a triangular perforation pattern ($\nu = 0.30$) ..... 61
Fig. 5.21. Effective stiffness for square clamped plate with a triangular perforation pattern ($\nu = 0.45$) ..... 61
Fig. 5.22. ANSYS® output for square clamped plates with triangular perforation patterns ($\nu = 0.20$, $P = 2.0$) ..... 62
Fig. 5.23. ANSYS® output for square clamped plates with triangular perforation patterns ($\nu = 0.30$, $P = 2.0$) ..... 63
Fig. 5.24. ANSYS® output for square clamped plates with triangular perforation patterns ($\nu = 0.45$, $P = 2.0$) ..... 64
Fig. 5.25. Effective stiffnesses based upon the fundamental frequencies for simply supported square plates with square perforation patterns ..... 65
Fig. 5.26. Effective stiffnesses based upon the fundamental frequencies for clamped square plates with square perforation patterns ..... 66
Fig. 5.27. Effective stiffnesses based upon the fundamental frequencies for simply supported square plates with triangular perforation patterns ..... 66

Fig. 5.28. Effective stiffnesses based upon the fundamental frequencies for clamped square plates with triangular perforation patterns ..... 67
Fig. 5.29. Sensitivity of effective stiffness for fundamental mode to number of holes for a clamped perforated square plate with a square perforation pattern ($\nu = 0.30$, $\mu = 0.70$) ..... 68
Fig. 5.30. Effective stiffness sensitivity to material density for fundamental mode of a plate with a square penetration pattern ($\nu = 0.30$, $\mu = 0.70$) ..... 70
Fig. 5.31. Effective stiffness sensitivity to material density for fundamental mode of a plate with a triangular penetration pattern ($\nu = 0.30$, $\mu = 0.70$) ..... 70
Fig. 6.1. Photograph of Bridgeport® R2G4 CNC horizontal mill ..... 74
Fig. 6.2. Photograph of CNC mill cutting 1.6 in. holes in a square pattern ..... 74
Fig. 6.3. Photograph of CNC mill using circular interpolation to cut an accurate perforation pattern ..... 75
Fig. 6.4. Photograph of experimental specimens and clamping fixture. ..... 75
Fig. 6.5. Schematic of impact analysis setup ..... 77
Fig. 6.6. Photograph of a perforated plate, clamped in the fixture, with an accelerometer attached ..... 77
Fig. 6.7. Schematic of experimental modal analysis setup ..... 79
Fig. 6.8. Photograph of laser vibrometer test setup ..... 80
Fig. 6.9. Comparison of dynamic and static effective stiffnesses for a clamped plate with a square perforation pattern. Experimental data is based upon the fundamental frequency ..... 81
Fig. 6.10. Comparison of dynamic and static effective stiffnesses for a clamped plate with a triangular perforation pattern. Experimental data is based upon the fundamental frequency ..... 81

Fig. 6.11. Experimental and FEM dynamic effective stiffness results for the fundamental mode of clamped plates with square perforation patterns ..... 82

Fig. 6.12. Experimental and FEM dynamic effective stiffness results for the fundamental mode of a clamped plates with triangular perforation patterns ..... 82

Fig. 6.13. Experimental and FEM dynamic effective stiffness results for the first two modes of a clamped plate with square perforation pattern. ..... 83

Fig. 6.14. Experimental and FEM dynamic effective stiffness results for the first two modes of a clamped plate with triangular perforation pattern. ..... 83

Fig. 6.15. Experimentally scanned mode shape for all clamped square plates tested ..... 85

# List of Tables

Table 4.1. Frequency constants for clamped plate ..... 30
Table 4.2. Properties for a solid plate model ..... 31
Table 4.3. Comparison of ANSYS® shell elements ..... 32
Table 4.4. FEM error convergence for solid plate models ..... 36
Table 4.5. Variation in ligament efficiency ($P = 2.0$) ..... 39
Table 5.1. Sensitivity of fundamental mode to plate thickness for a clamped perforated square plate with a square perforation pattern ($\nu = 0.3$, $\mu = 0.7$) ..... 69
Table 6.1. Experimental test specimens using 6061-T6 aluminum (geometric and material properties listed in Table 4.2) with clamped boundary conditions ..... 72
Table 6.2. List of experimental equipment for impact tests ..... 75
Table 6.3. List of experimental equipment for optical tests ..... 77
Table 6.4. Fundamental frequency data for a clamped solid plate ..... 82
Table 6.5. Mode 2 (1,2) frequency data for a clamped solid plate ..... 82

# List of Symbols

| | |
|---|---|
| $a$ | plate width (in) |
| $b$ | plate length (in) |
| $D$ | bending stiffness $\left[\frac{Eh^3}{12(1-\nu^2)}\right]$ (lb-in) |
| $D^*$ | effective bending stiffness (lb-in) |
| $E$ | Young's modulus (lb/in$^2$) |
| $E^*$ | effective Young's modulus (lb/in$^2$) |
| $f_{FEM}$ | frequency data from ANSYS finite element analysis (Hz) |
| $f_{theory}$ | frequency data from theory (Hz) |
| $g$ | gravitational acceleration |
| $h$ | minimum ligament width (in) |
| $l$ | plate length or width for square plate (in) |
| $m,n$ | modal half waves corresponding to directions $x$ and $y$ |
| $\bar{m}$ | mass per unit area (lb-s$^2$/in$^3$) |
| $M_o$ | edge moment per unit length (lb-in/in) |
| $[N]^T$ | element shape function |
| $P$ | pitch (in) |
| $q$ | force per unit length |
| $R$ | radius of perforations (in) |
| $R_c$ | critical ratio $\left[\frac{2r_o}{l}\right]$ |
| $\{r_e\}$ | load vector for consistent nodal loading |
| $r_o$ | radius of perforation for a single-hole plate (in) |
| $R_{shell}$ | mean radius of shell (in) |
| $t$ | plate or shell thickness (in) |
| $T(t)$ | characteristic time function |
| $\nu$ | Poisson's ratio for plate material |

| | |
|---|---|
| $\nu^*$ | effective Poisson's ratio |
| $W(x,y)$ | shape function |
| $w(x,y,t)$ | transverse deflection of plate (in) |
| $w_{FEM}$ | deflection data from ANSYS finite element analysis (in) |
| $W_{mn}$ | amplitude coefficient |
| $w_{theory}$ | deflection data from theory (in) |
| $x,y,z$ | Cartesian coordinates |
| $\mu$ | ligament efficiency $\left[1-\frac{2R}{P}\right]$ |
| $\gamma$ | specific weight (lb/in$^3$) |
| $\rho$ | mass density (lb-s$^2$/in$^4$) |
| $\omega_{mn}$ | natural circular frequency (rad/s) |
| $\omega^*$ | frequency parameter $\left[\omega^* = \omega l^2 \sqrt{\frac{\rho}{D}}\right]$ |

# Chapter 1
# Introduction

## 1.1 Background

Mechanical engineers, aerospace engineers, and civil engineers all design structures and structural components with plates and shells. Fortunately, the design and analysis of solid plates and shells is well established. Structural designs often deliberately incorporate cutouts or perforations to reduce the materials, lighten the loads, allow for ventilation, or provide functional openings. Accounting for these perforations in the analysis can be an integral part of determining the correct deflections, stresses, modal frequencies, and mode shapes of a particular structure. In cases where a plate is perforated with a number of circular holes, assembled in a pattern, the structural changes have traditionally been accounted for by using effective material constants. Usually, the perforated plate is equivalent to a uniform solid plate of the same thickness but having new modulus and Poisson ratio values established by an equal global stiffness criterion.

Effective material constants have been developed for plates rather than for shells. To the best of the author's knowledge, there is no documented research detailing their applicability to shells. This is partially because the behavior of a shell is much more complex than that of a plate. In addition, industry has had numerous engineering applications involving plates. For example the heat exchanger industry, focusing on tube sheet behavior, has supported perforated plate research for over fifty years. As a result, there is an abundance of numerical and experimental work on the static behavior of perforated plates.

This study is intended to take the next logical step in understanding the behavior of a perforated structure, i.e., characterizing the dynamic behavior of a perforated plate.

The work is intended to answer three questions. First, are effective material constants developed for statically loaded plates applicable to dynamically loaded plates? Next, what are the values of these "dynamic" effective material constants? Finally, can one gain any insight as to whether "dynamic" effective material constants are applicable to dynamically loaded shells?

## 1.2 General Approach

To compare and contrast the applicability of statically developed material properties in a dynamic analysis, finite element (FE) methods and experimental methods are utilized to predict the dynamic behavior of perforated plates. In the case of a static analysis this behavior is quantified as a deflection, and for a dynamic analysis, this behavior is quantified as a natural frequency and the associated mode shape.

The theoretical behavior of a perforated plate, as determined by statically developed material properties, was determined by applying effective material properties to response equations for a solid plate. This approach was compared to the results obtained by analyzing a perforated plate model with FE software, as well as experimental vibration measurements.

## 1.3 Thesis Outline

Previous studies have been completed on the effective material properties generated from plates with statically applied loads and various perforation patterns. In addition, work has been done on the dynamic behavior of plates with a single hole. These previous investigations are reviewed in Chapter 2. Chapter 3 gives some applications for the dynamic loading of perforated plates. Chapter 4 describes how the FE models were developed and benchmarked against previous work. Chapters 5 and 6 present the results of the modal analysis of perforated plates. In Chapter 5, FE results identify the effective stiffness parameters as a function of perforation size. In Chapter 6,

experimental data is presented to support the results of Chapter 5. Finally, Chapter 7 summarizes the findings and provides conclusions.

# Chapter 2

# Previous Investigations on Perforated Plates

## 2.1 Introduction

There are two distinct areas of study associated with the analysis of perforated plates, i.e., the static analysis of a plate with multiple uniform perforations and the dynamic analysis of a plate with a single perforation.

The static analysis of perforated plates has been a topic of interest for years because of the many industrial applications. Some examples include nozzles, material or fluid strainers, and heat exchangers. Each of these applications incorporates a design based on classical plate theory and static loading. Of these, the heat exchanger (Fig. 2.1) is the most documented. The tubes in a heat exchanger are held in place by a perforated plate called a tube sheet (Fig. 2.2). The increased compliance caused by the perforations in this sheet are accounted for by using equivalent plate theory. Equivalent plate theory was developed to replace the actual drilled plate by an equivalent undrilled one of the same dimensions, for which the classical solid plate theory in the elastic range is applicable. This equivalent plate must have the appropriate elastic constants so as to present the same behavior as the actual one when subjected to the same loading.

The dynamic analyses of perforated plates has been limited to a single perforation, and as far as the author knows there have been no studies completed that investigate dynamic effective material constants. However, there are a countless number of applications in industry, which require the dynamic analysis of perforated plates. Identification of the effective material properties for such cases would be a significant contribution to the field.

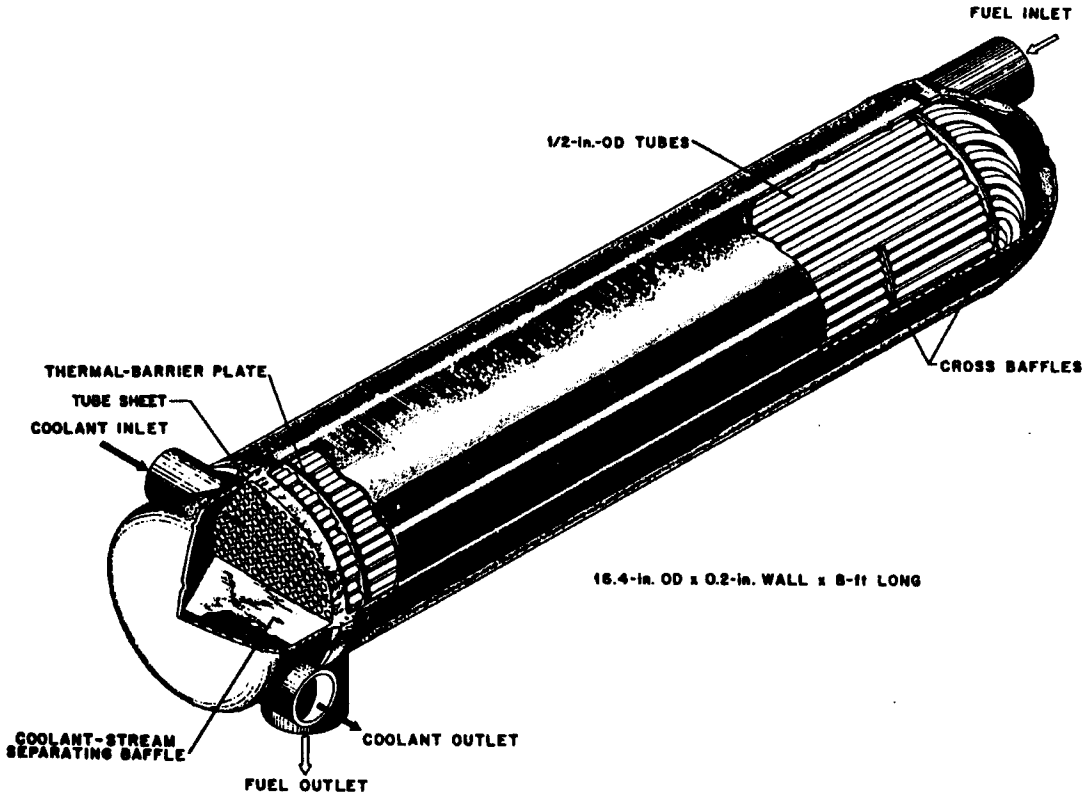


Fig. 2.1. Heat exchanger with cutaway view showing tube sheet [2.1].

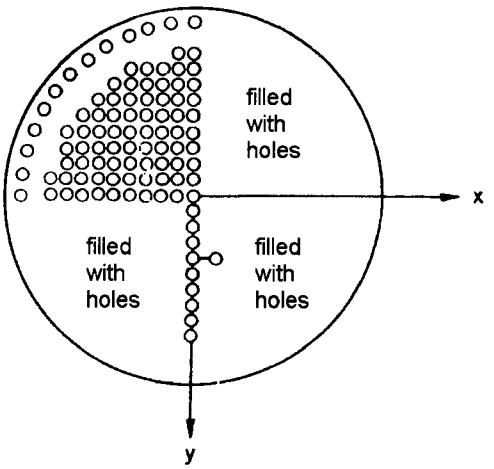


Fig. 2.2. Tube sheet from heat exchanger [2.2].

## 2.2 Perforation Geometry and Terminology

Two perforation patterns, square and triangular, are most common in industry (see Figs. 2.3 and 2.4). Both patterns are geometrically defined by one parameter, $\mu$, referred to as the ligament efficiency, i.e.,

$$\mu = \frac{h}{P} = \left[1 - \frac{2R}{P}\right] \tag{2.1}$$

Ligament efficiency is the ratio of ligament width to the perforation center-to-center distance, defined in Fig. 2.3 as the pitch, $P$. The most fundamental cells for the square and triangular patterns are a square and a pentagon, respectively. These basic shapes, containing a single hole, are used in conjunction with solid modeling and FE meshing methods to generate a uniform perforation pattern.

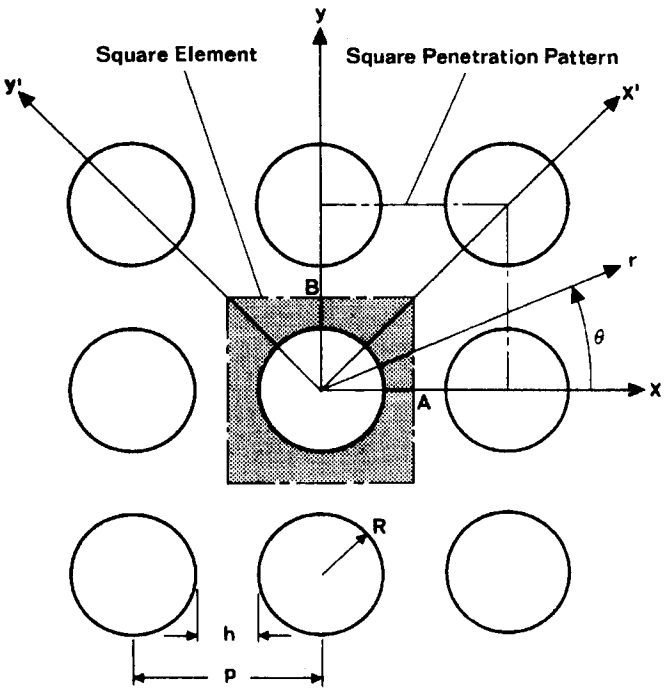


Fig. 2.3. Geometry for square perforation pattern [2.3].

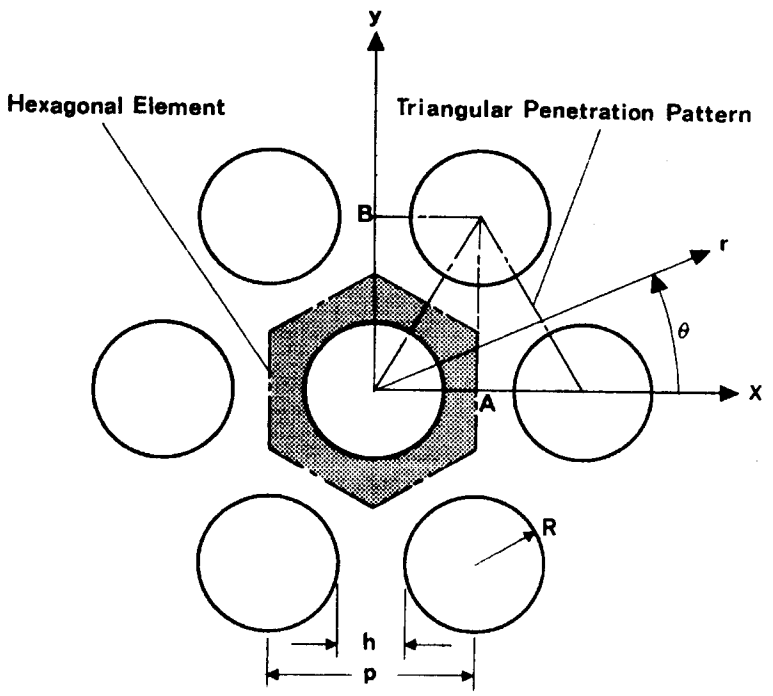


Fig. 2.4. Geometry for triangular perforation pattern [2.3].

## 2.3 History of Perforated Plates – Static

Over the past fifty years there have been a large number of technical publications dealing with stress and stiffness calculations for perforated plates. With the development of industrial applications in tubesheet heat exchangers and other similar equipment, this was an active research area that continued to evolve through 1985. By 1985 most issues had been resolved and solutions to these problems have since been incorporated into modern pressure vessel codes. "Evolution and Synthesis of Effective Elastic Constants Concept for the Design of Tubesheets" by Osweiller [2.4] outlines the evolution of equivalent plate theory. This paper is an excellent reference that summarizes about 60 other papers and codes. One of the key findings discussed in Osweiller's paper is the transition range from thick to thin plates, which is relevant to this thesis because it focuses on thin plates.

Osweiller breaks the evolution down into three generations: 1948-1959, 1960-1962, and 1963-1985. The first generation, as Osweiller calls it, marks the introduction of equivalent solid plate theory. In 1948 Gardner [2.5] proposed equivalent solid plate theory. He suggested that the flexural rigidity, $D$, of the plate before drilling be reduced by factor $\lambda$ which he refers to as "deflection efficiency." This factor allows for the calculation of the flexural rigidity, $D^*$, of the equivalent plate where $D^*=\lambda D$ ($\lambda \leq 1$). In 1954 Duncan [2.6] experimentally determined $\lambda$ by measuring the deflections of tubesheets loaded in bending. He measured the deflection of the plate before drilling, $w_{np}$, and after drilling, $w_p$. The ratio of the two gave the deflection efficiency, $\lambda = \frac{w_{np}}{w_p}$.

The second generation, 1960-1962, marks the introduction of equivalent material constants. As a refinement of the effective flexural rigidity, second generation constants defined Young's modulus, $E^*$, and Poisson's ratio, $v^*$, for a perforated plate. Curves for $\frac{E^*}{E}$ were preferred over curves for $\frac{D^*}{D}$ because the ratio of $\frac{E^*}{E}$ is material independent. These effective material constants were first investigated experimentally. In 1960 Sampson [2.7] performed experimental tests using photo-elastic techniques. The tests, performed with rectangular plates, perforated with a triangular penetration pattern and loaded in bending, showed the following:

a) $\frac{E^*}{E}$ does not vary with material

b) $\frac{E^*}{E}$ and $v^*$ are independent of loading direction (isotropic behavior)

c) $\frac{t}{P} = 2$ is a transition value for thin-to-thick perforated plates, where $t$ is the thickness of the plate

d) $\frac{E^*}{E}$ and $\nu^*$ vary markedly with plate thickness when $\frac{t}{P} \leq 2$

In 1962 O'Donnell [2.8] synthesized Sampson's results to propose a single set of curves to determine $\frac{E^*}{E}$ and $\nu^*$ as a function of ligament efficiency. These curves, however, were for thick plates ($t > 2P$). The ASME Boiler and Pressure Vessel Codes [2.9] also cite curves for effective elastic constants, but they too are only for thick plates.

The third generation, 1963-1985, marks the introduction of doubly periodic stress distribution theory. Using this theory in conjunction with computational methods, effective elastic constants for triangular and square patterns were determined. The theory was applied to infinite plates evenly perforated in two directions and loaded in bending (also loaded in plane stress). Meijers' published papers in 1960 and 1980 focused on thin plates in bending [2.10 and 2.11]. His work for thin plates has been adopted into the French Pressure Vessel Code CODAP [2.12]. The CODAP curves, for both triangular and square perforation patterns, are used in this paper.

### 2.3.1 Loading Orientation

Experimental work done by Sampson [2.7] and confirmed by O'Donnell [2.8] shows that effective elastic constants for triangular patterns are independent of loading direction (isotropic) for bending problems. O'Donnell [2.2, 2.13, 2.14] also shows, however, that elastic constants for square patterns depend on the loading direction (anisotropic) for bending. Fortunately, the two sets of effective elastic constants for square perforation patterns have been converted (an approximation) into one set of "isotropic" effective elastic constants. The approximation simplifies this study by enabling a direct comparison between finite element data and classical isotropic theory applied to an equivalent plate.

### 2.3.2 Thick to Thin Transition Range

Studies done by Sampson [2.7] showed that values of $\frac{E^*}{E}$ (Fig. 2.5) and $\nu^*$ (Fig. 2.6) can vary significantly with plate thickness. For $t \geq 2P$ this variation is very gradual, and as the plate gets thicker the bending values approach the plane stress values for a solid plate. In this region, the effective elastic constants are determined by equating strains in the equivalent solid material to the average strains in the perforated material. For $t < 2P$, the variation in effective material properties is rapid, and highly dependent on plate thickness. In the "thin plate" region, plane stress conditions are approximated.

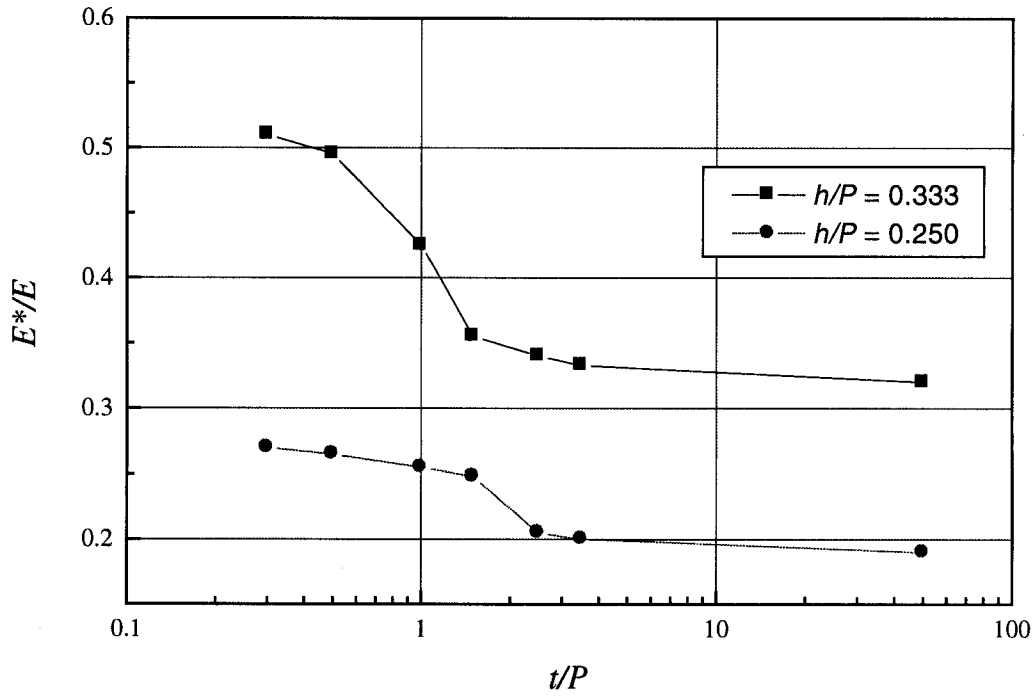


Fig. 2.5. Variation of Sampson effective elastic modulus with thickness for a plate in bending ($\nu = 0.50$) [2.7].

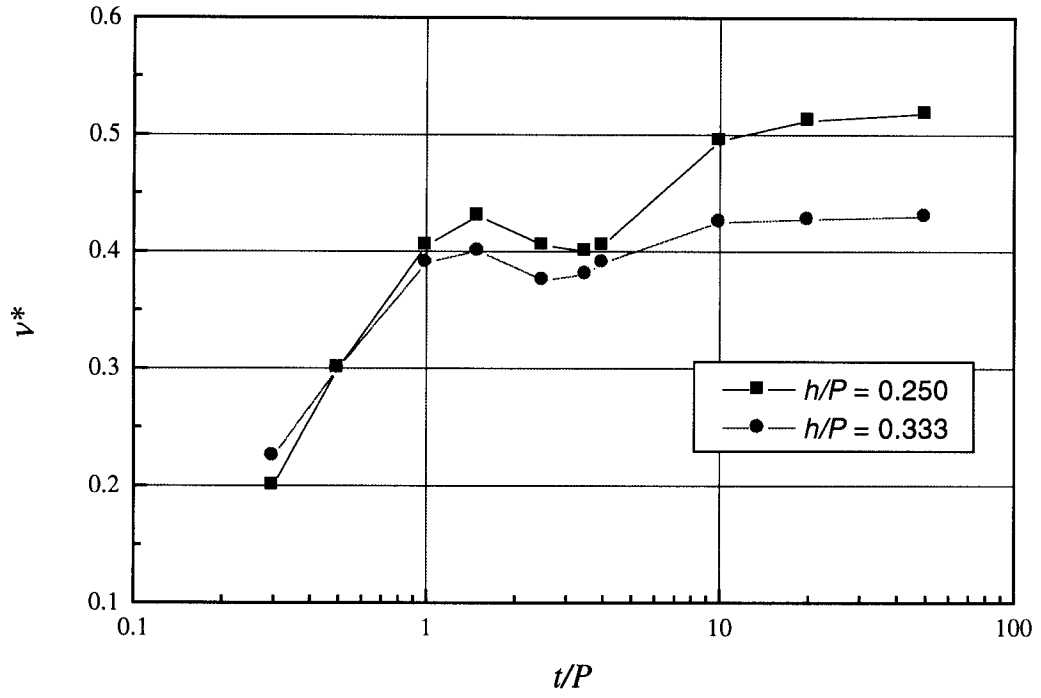


Fig. 2.6. Variation of Sampson effective Poisson's ratio with thickness for a plate in bending ($\nu = 0.50$) [2.7].

### 2.3.3 Numerical and Experimental Data

Theoretical and experimental data for effective material properties have been fused together in the design curves used today. The resulting curves are complete over the full range of ligament efficiencies. Theoretical data incorporated into these curves is based on doubly periodic stress distribution theory. Experimental data comes from deflection data of thin plates statically loaded in bending.

The CODAP curves (Figs. 2.7 and 2.8), used as a static benchmark in this thesis, are applicable over a wide range of plate thickness ($0.25 < t/P < 50$). The data is for simply supported thin plates ($t/P \leq 1$) loaded in bending. Osweiller [2.4] explains that they are constructed using a combination of Meijers' theoretical values and other experimental values.

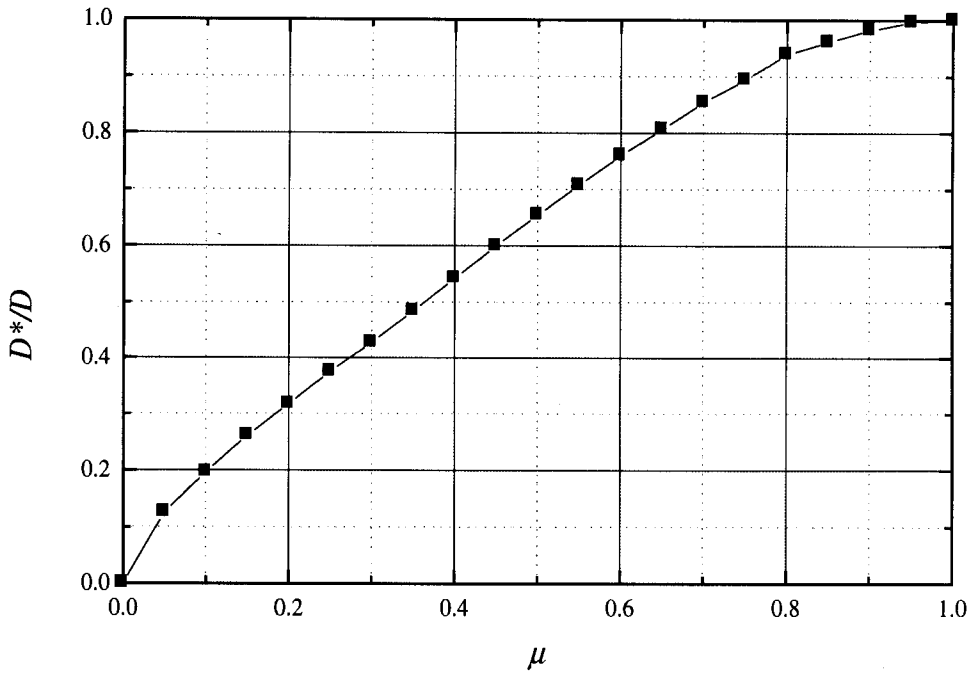


Fig. 2.7. Static effective stiffness, $D^*$, versus ligament efficiency for simply supported plate with a square perforation pattern.

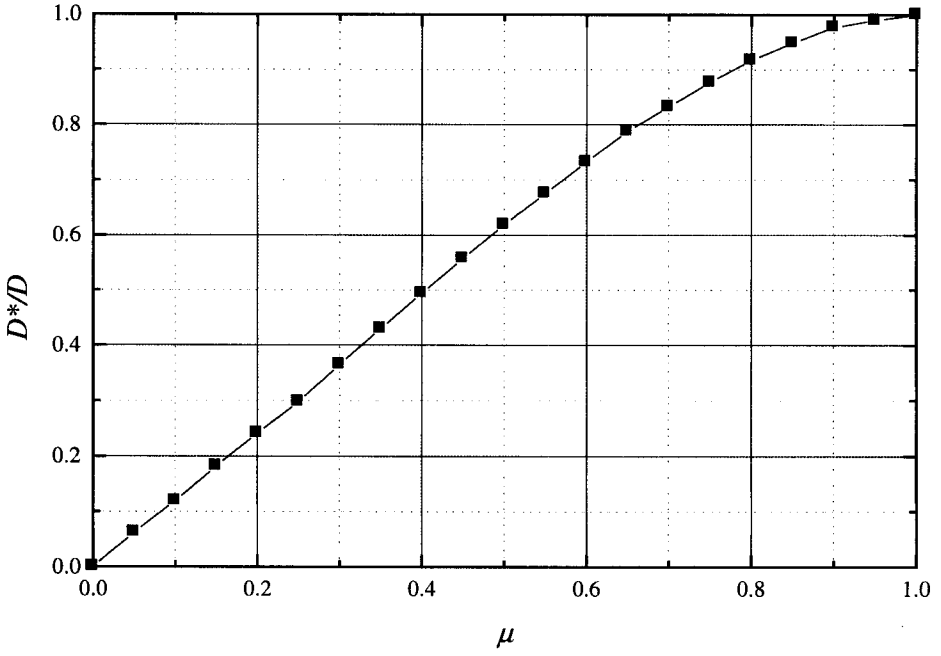


Fig. 2.8. Static effective stiffness, $D^*$, versus ligament efficiency for simply supported plate with a triangular perforation pattern.

## 2.4 History of Perforated Plates – Modal

Free-vibration data for perforated plates is only available for square, single-hole plates. As far as the author knows there are no special effective material constants for the free-vibration of plates, or shells, having multiple perforations. However, some researchers doing work with multiple perforations, such as Powers [2.15], have assumed that effective material constants developed through statically applied loading apply to a dynamic analysis.

Vibration studies on square, single-hole elastic plates date back to the middle 1900's. In 1975, Hegarty and Ariman [2.16] published the first paper of practical significance, which identified trends caused by perforations. They investigated the free vibration of simply supported and clamped plates with a single, centrally located hole using a least-squares point-matching method. Their work focused on thin, homogenous, isotropic, linearly elastic plates with a uniform thickness $t$. The geometric variables were edge length, $l$, and the hole radius, $r_o$. Their results show that the fundamental frequency of a plate depends on boundary conditions and Poisson's ratio. For example, Figs. 2.9 and 2.10 illustrate how the frequency decreases with Poisson's ratio. The point where the frequency ratio is a minimum is referred to as the critical ratio, $R_c = \frac{2r_o}{l}$. Figure 2.11 shows how the theoretical ratio varies as a function of Poisson's ratio for the simply supported and clamped boundary conditions. Hegartly and Ariman [2.16] proposed a two-fold mechanism of strain relief and mass reduction to explain to the existence of the critical ratio (Fig. 2.12). Here Hegartly and Ariman use the parameter $\omega^*$, defined as the frequency parameter $\omega^* = \omega l^2 \sqrt{\frac{\rho}{D}}$ where $\rho$ denotes the mass density.

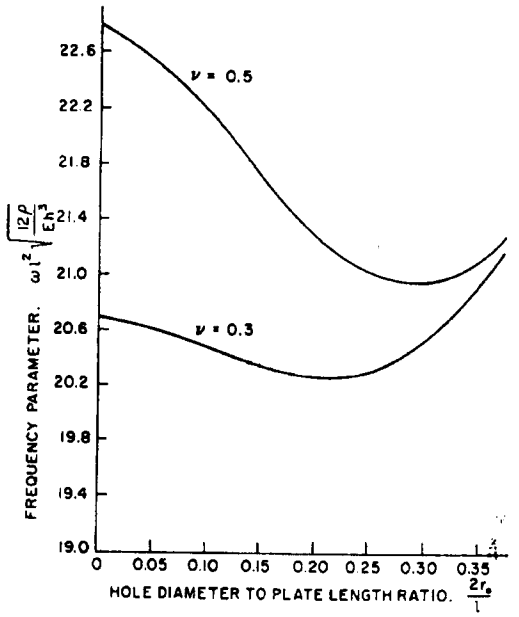


Fig. 2.9. Variation in frequency with hole size for a simply supported, square plate. The frequency parameter is a function of Poisson's ratio [2.16] (note that in the figure *h* refers to plate thickness).

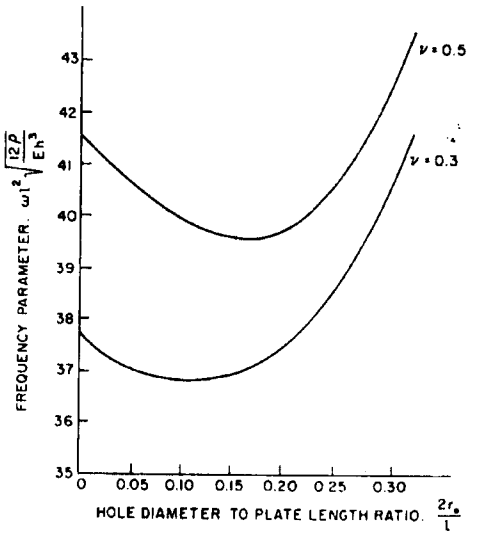


Fig. 2.10. Variation in frequency with hole size for a clamped square plate. The frequency parameter is a function of Poisson's ratio [2.16] (note that in the figure *h* refers to plate thickness).

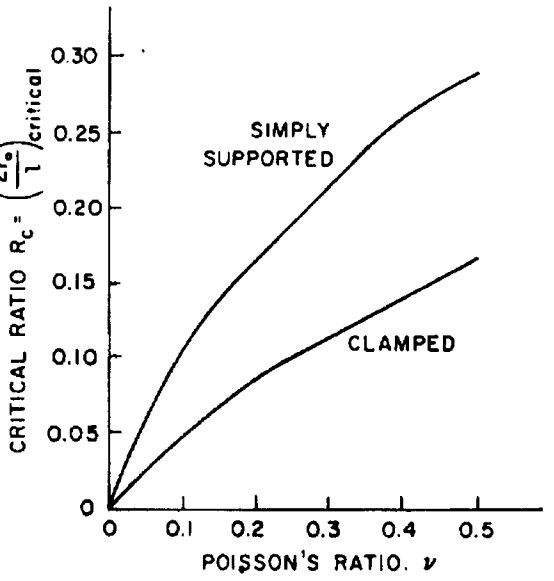


Fig. 2.11. Variation in critical hole ratio with Poisson's ratio for both clamped and simply supported plates [2.16].

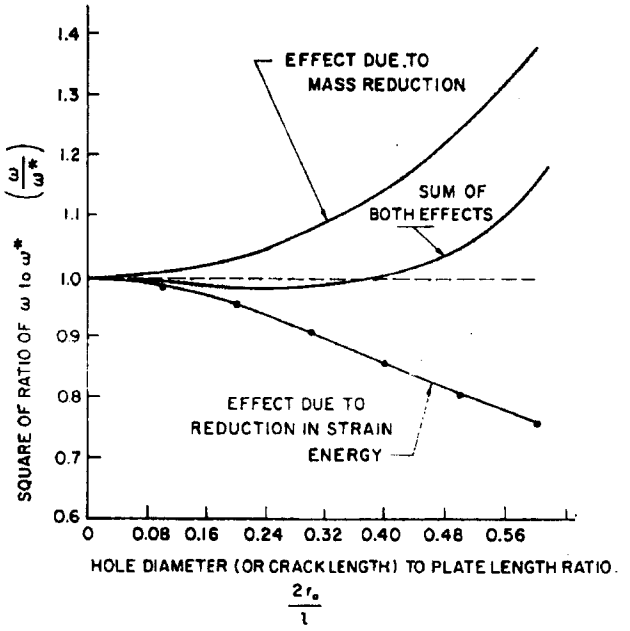


Fig. 2.12. Illustration of mechanisms for strain energy reduction and mass reduction effects on frequency of plate [2.16].

In 1981 Nagaya [2.17] presented a solution to the problem of vibrating plates of doubly connected arbitrarily shapes. Using a "simplified approximate method" Nagaya derived boundary dependent equations for eigenfrequencies and mode shapes.

In 1988 Bicos and Springer [2.18] presented a method for analyzing the free damped vibration characteristics of plates and cylinders with circular cutouts. They claimed to have a computer code that calculates natural frequencies and mode shapes for simply supported and clamped plate models.

In 1995 Lim and Liew [2.19] performed a vibration analysis on a continuum-plate domain rather than using discretization methods. Employing the global Ritz minimization procedure, with a set of orthogonally generated polynomials as admissible function, they derived a governing eigenvalue equation. By applying this equation they developed a comprehensive set of first-known vibration frequencies and mode shapes for perforated plates.

## 2.5 References

[2.1] Nelms, H. A., "Flow-Induced Vibrations: A Problem in the Design of Heat Exchangers for Nuclear Service," Flow-Induced Vibration in Heat Exchangers, Winter Annual Meeting of ASME, New York, NY, p. 10, 1970.

[2.2] O'Donnell, W. J., "A Study of Perforated Plates with Square Penetration Patterns," *Welding Research Council Bulletin* No. 124, pp. 1-13, 1967.

[2.3] Slot, T., *Stress Analysis of Thick Perforated Plates*, Technomic Publishing, Westport, CT, 1972.

[2.4] Osweiller, F., "Evolution and Synthesis of the Effective Elastic Constants Concept for the Design of Tubesheets," *Journal of Pressure Vessel Technology*, Vol. 111, pp. 209-217, 1989.

[2.5] Gardner, K. A., "Heat-Exchanger Tubesheet Design," *Journal of Applied Mechanics*, Vol. 15, No. 4, pp. 377-385, 1948.

[2.6] Duncan, J. P., "The Structural Efficiency of Tube-Plates for Heat Exchangers," Proceedings of the Institution of Mechanical Engineers, Vol. 169, pp. 789-810, 1955.

[2.7] Sampson, R. C., "Photoelastic Frozen Stress Study of the Effective Elastic Constants of Perforated Materials," WARD-DLE-319, Office of Technical Service, Dept. of Commerce, Washington, D.C., 1959.

[2.8] O'Donnell, W. S., and Langer, B. F., "Design of Perforated Plates," *Journal of Engineering for Industry*, Vol. 84B, pp. 307-319, August 1962.

[2.9] "Stresses in Perforated Flat Plates," Article A-8000, Section III – Division 1 Appendices, *ASME Boiler and Pressure Vessel Code*, The American Society of Mechanical Engineers, New York, NY, pp. 210-223, 1995.

[2.10] Meijers, P., "Plates with a Doubly-Periodic Pattern of Circular Holes Loaded in Plane Stress or in Bending," ASME Publication on First International Conference on Pressure Vessel Technology, Part I, Design and Analysis, 1969.

[2.11] Meijers, P., "Refined Theory for Bending and Torsion of Perforated Plates," Pressure Vessel Components Design and Analysis, *Proceedings of the 1985 Pressure Vessels and Piping Conference*, Vol. 98-2, ASME, New York, NY, pp. 11-19, 1985.

[2.12] CODAP, Code Francais de Construction des Appa reils a Pression, 1985.

[2.13] O'Donnell, W. J., "Further Theoretical Treatment of Perforated Plates with Square Penetration Patterns," *Welding Research Council Bulletin*, No. 151, pp. 1-12, 1970.

[2.14] O'Donnell, W. J., "Effective Elastic Constants for the Bending of Thin Perforated Plates With Triangular and Square Penetration Patterns," *Journal of Engineering for Industry*, Vol. 95, pp. 121-128, 1973.

[2.15] Powers, J. P., "Structural and Fatigue Analysis of the Sandia Laboratory Microfusion Reaction Chamber," M.S. Thesis, Department of Mechanical Engineering, University of Wisconsin—Madison, 1991.

[2.16] Hegarty, R. F., and Ariman, T., "Elasto-Dynamic Analysis of Rectangular Plates with Circular Holes," *International Journal of Solids and Structures*, Vol. 11, pp. 895-906, 1975.

[2.17] Nagaya, K., "Simplified Method for Solving Problems of Vibrating Plates of Doubly Connected Arbitrary Shape, Part I: Derivation of the Frequency Equation," *Journal of Sound and Vibration*, Vol. 74, pp. 543-551, 1981.

[2.18] Bicos, A. S., and Springer, G. S., "Vibrational Characteristics of Composite Panels with Cutouts," *American Institute of Aeronautics and Astronautics Journal*, Vol. 27, No. 8, pp. 1116-1122, 1988.

[2.19] Lim, C. W., and Liew, K. M., "Vibrations of Perforated Plates with Rounded Corners," *Journal of Engineering Mechanics*, Vol. 121, No. 2, pp. 203-213, 1995.

# Chapter 3

# Specific Application for Perforated Plates and Shells

## 3.1 Introduction

There are a large number of perforated structures in use that are dynamically loaded. Some examples include auto bodies, aircraft bodies, screens, strainers, and nuclear fusion reaction chambers. In some applications, such as the nuclear fusion chamber, there is more emphasis on structural analysis. This is partially because the harsh loading cycles amplify the detrimental effects caused by perforations. In addition, the safety and reliability of the fusion chamber are critical.

## 3.2 Fusion Chambers

The process of nuclear fusion (Fig. 3.1) is the source of energy for the sun and all other stars. Reproducing this process on earth is a potentially safer way to produce cost-effective electricity. For example, the fission process produces dangerous by-products and is always at risk of a runaway reaction while the fusion process is clear of these hazards.

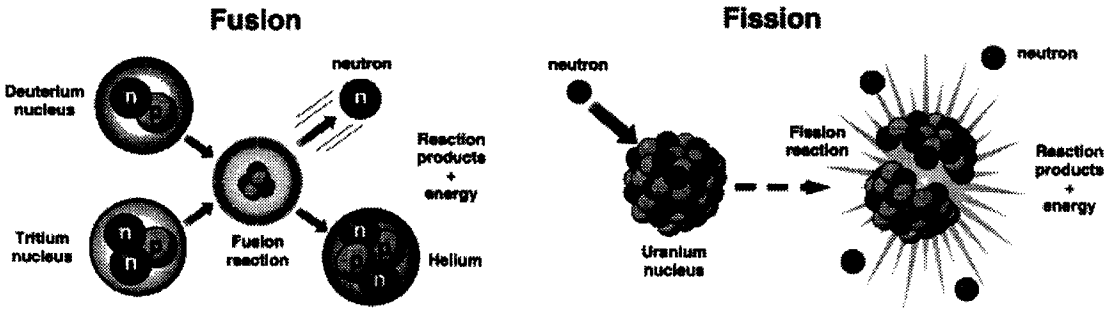


Fig. 3.1. Diagram of nuclear reactions - fusion vs. fission [3.1]

There are three ways of confining fusion fuel reactions: gravitational confinement, magnetic confinement, and inertial confinement. Of these only the later two can be achieved in a laboratory. Inertial confinement, in particular, is interesting because of the perforated confinement chamber. The chambers are indirectly related to this study because of their perforations, yet they are more complex than the plates because of the different geometry.

The Department of Energy supports research for developing fusion energy using inertial confinement fusion (ICF) (Fig. 3.2). The program is currently involved with a number of different projects. The Nova Laser Facility is the world's primary research tool in this area while the newer National Ignition Facility (NIF) (Fig. 3.3), currently under construction, is envisioned as a large step forward from Nova. Both of these facilities incorporate spherical chambers (Figs. 3.4 and 3.5).

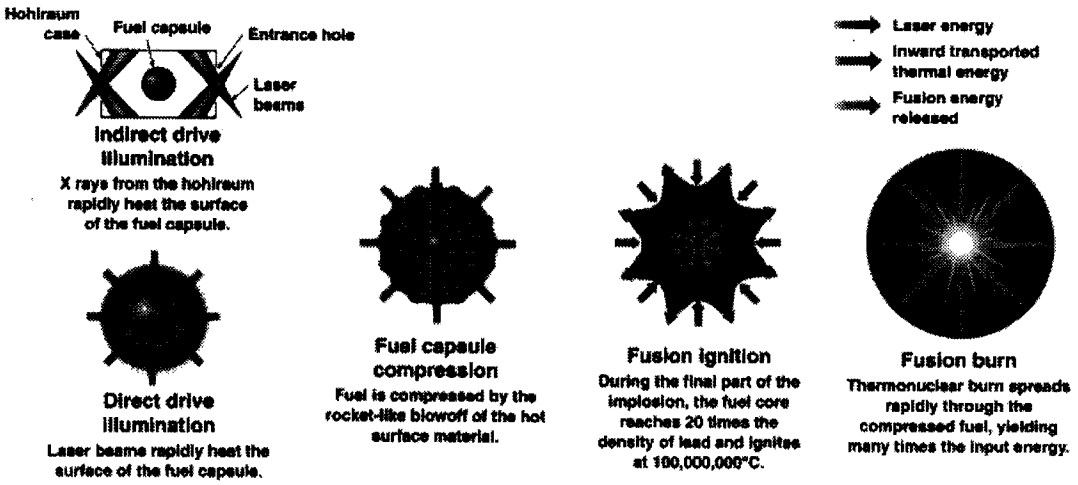


Fig. 3.2. Diagram showing four steps of the ICF process [3.1].

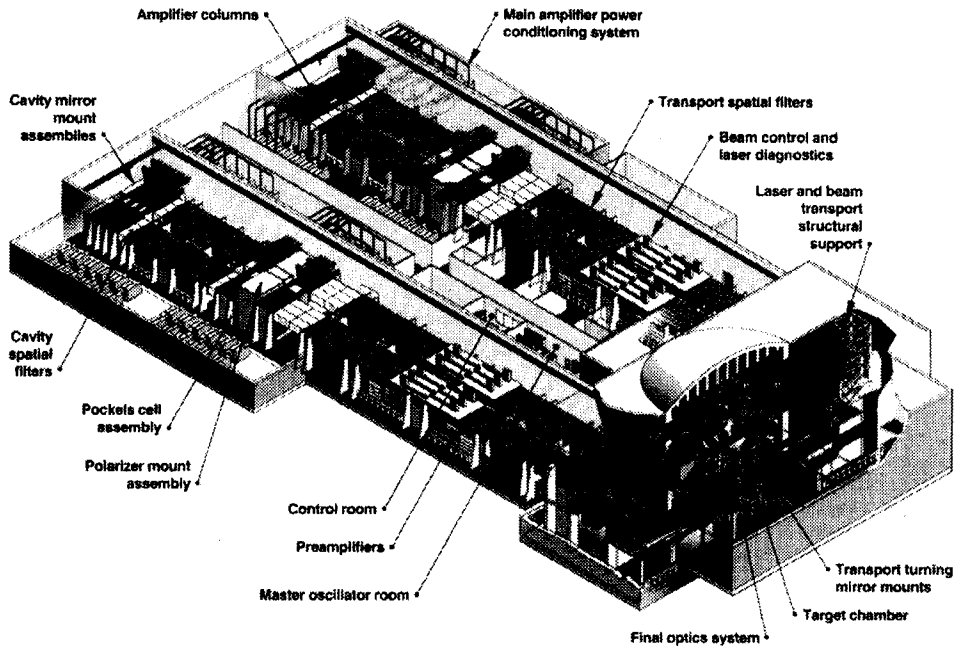


Fig. 3.3. View of the laser and target area building for NIF, the world's most powerful neodymium laser system. The $1-billion facility is 200 m × 85 m [3.2].

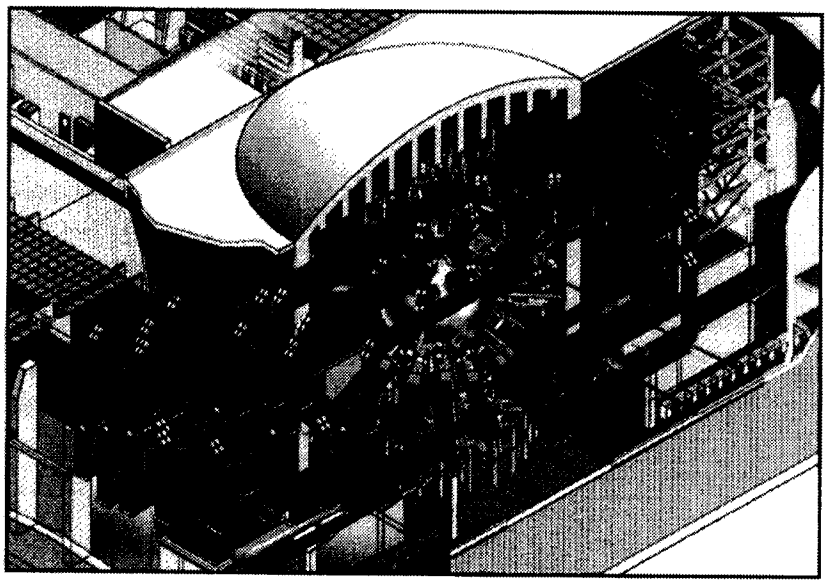

Fig. 3.4. Enlarged view looking into NIF's target area with the spherical target chamber located at the center of the diagram [3.2].

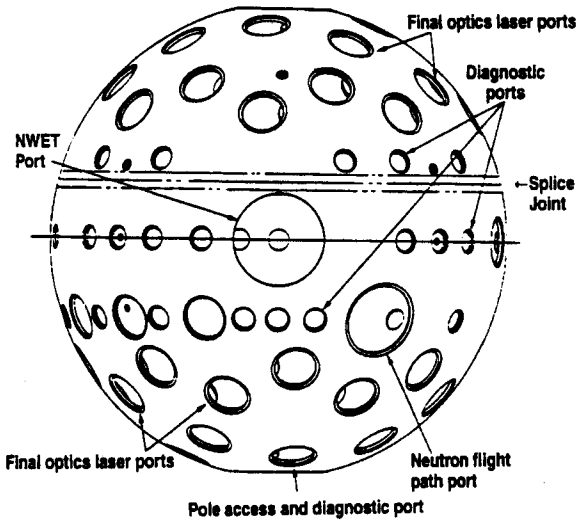


Fig. 3.5. NIF target chamber [3.3].

A facility that the ICF program proposed but failed to complete was the Light Ion Microfusion Facility (LMF) (Fig. 3.6). This proposed facility utilized a cylindrical chamber rather than the traditional sphere (Fig. 3.7). Powers [3.4] analyzed this chamber using effective material constants to account for the perforations.

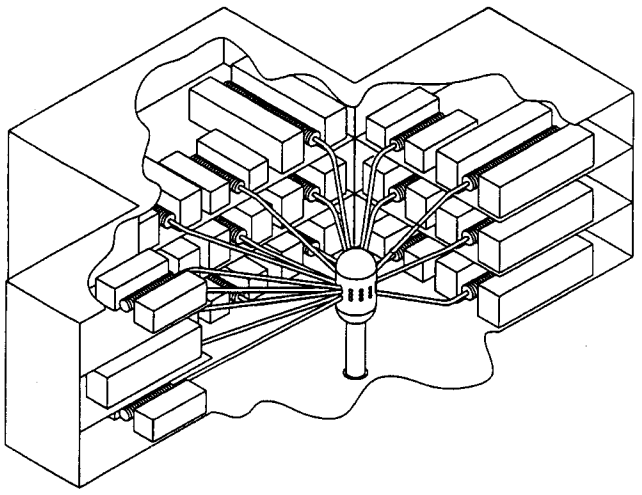

Fig. 3.6. Light Ion Microfusion Facility [3.5].

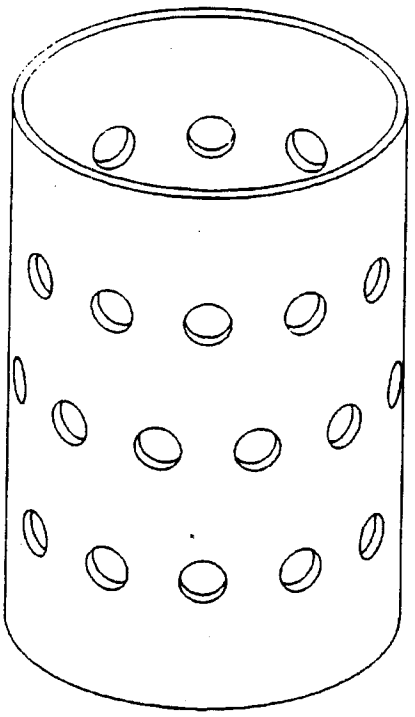

Fig. 3.7. Perforated cylindrical target chamber from LMF [3.4].

ICF target chambers, no matter what their geometry, must withstand large structural loads. The initial fusion blast and the dynamic cycling through repeated blasts cause these loads. For a chamber design to endure these shocks the designer must be able to model the chamber and predict its response. Analytically modeling chamber perforations is a challenge, especially in light of the incredible number of holes in some of these chambers. In the NIF, for example, there are over 100 laser ports [3.3].

## 3.3 References

[3.1] Nova Laser Facility Poster, completed under contract No. W-7405-ENG-48, Lawrence Livermore National Laboratory, 1996.

[3.2] Energy & Technology Review, The National Ignition Facility, University of California, Lawrence Livermore National Laboratory, 1994.

[3.3] "National Ignition Facility Conceptual Design Report," UCRL-PROP-11709, L-16973-1, Lawrence Livermore National Laboratory, 1994.

[3.4] Powers, J. P., "Structural and Fatigue Analysis of the Sandia Laboratory Microfusion Reaction Chamber," M.S. Thesis, Department of Mechanical Engineering, University of Wisconsin—Madison, Madison, WI, 1991.

[3.5] Engelstad, R. L., Cousseau, P. L., Kulcinski, G. L., "Near Term ICF Target Chambers," Fusion Power Associates, FPA-96-2, Madison, Wisconsin, 1996.

# Chapter 4

# Finite Element Benchmark

## 4.1 Introduction

Simply supported perforated plates have been used in the past to generate "static-plate" effective material constants and thus are used here as a benchmark for "dynamic-plate" effective material constants. A benchmark, such as this, is used to validate a model. In this case the model is a finite element (FE) representation of a simply supported perforated plate. Comparing the FE static-deflection results to the deflection values calculated with the effective material constants enables model refinement.

## 4.2 Solid Plate Theory

### 4.2.1 Thin Plate Theory

The work done in this thesis focuses on plates but the intent is to transfer the knowledge gained to the dynamic analysis of a shell. Such a transfer of information requires as much similarity as possible between the shell and the plate. For example, thin plates are used because the previously mentioned shells are thin-walled, e.g., $\frac{t}{R_{shell}} \leq \frac{1}{20}$, where $t$ denotes the shell thickness and $R_{shell}$ is the mean radius of the shell. Thin plate theory requires that $\frac{t}{l} \leq \frac{1}{20}$, where $t$ denotes the plate thickness and $l$ the minimum edge length.

### 4.2.2 Classical Plate Theory – Static Analysis

The following analysis utilizes a simply supported rectangular plate of dimensions $a \times b \times t$ subjected to symmetrically distributed edge moments at $y = \pm\frac{b}{2}$ (Fig. 4.1). The

uniformly distributed edge moments per unit length, $M_o$, are statically applied, resulting in a transverse deflection $w$. Ugural [4.1] represents the solution with an infinite series, i.e.,

$$w(x,y)=\frac{2M_o a}{\pi^2 D}\sum_{m=1,3,\ldots}^{\infty}\frac{\sin(m\pi x/a)}{m^2\cosh\alpha_m}\left(\frac{b}{2}\tanh\alpha_m\cosh\frac{m\pi y}{a}-y\sinh\frac{m\pi y}{a}\right) \tag{4.1}$$

where the flexural stiffness, $D$, and dimensional parameter, $\alpha_m$, are given by:

$$D=\frac{Eh^3}{12(1-\nu^2)} \tag{4.2}$$

$$\alpha_m=\frac{m\pi b}{2a} \tag{4.3}$$

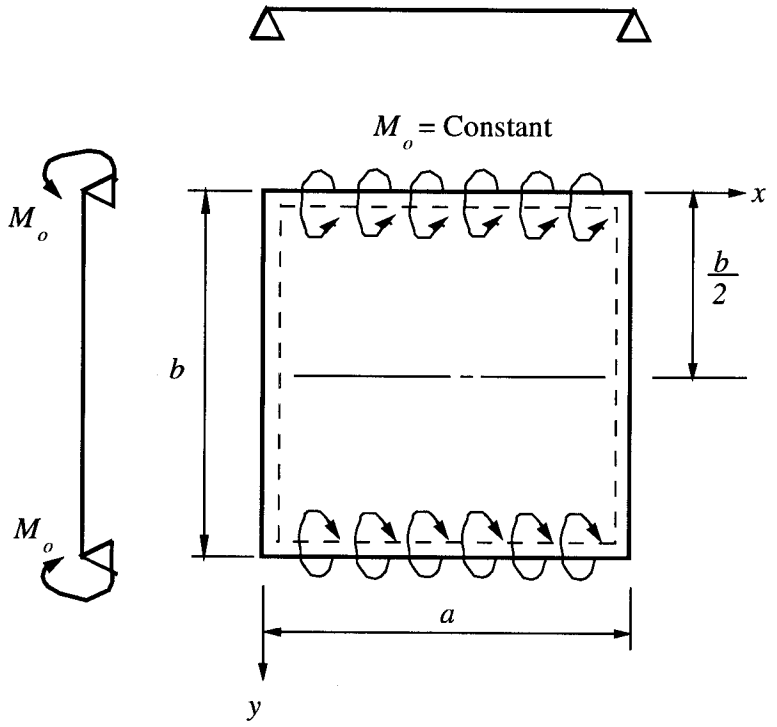


Fig. 4.1. Schematic of a simply supported plate with uniform edge moments.

### 4.2.3 Classical Plate Theory - Modal Analysis

The dynamic response of thin, simply supported plates (Fig. 4.1) can be described by the following series [4.2]:

$$w(x,y) = W(x,y)\,T(t) = \sum_{m=1}^{\infty}\sum_{n=1}^{\infty} W_{mn}\cos(\omega_{m,n}t)\sin\left\{\frac{m\pi x}{a}\right\}\sin\left\{\frac{m\pi x}{b}\right\}$$

$$(m = 1,2,3,\ldots \text{ and } n = 1,2,3,\ldots) \qquad (4.4)$$

$$\omega_{mn} = \pi^2\left[\frac{m^2}{a^2}+\frac{n^2}{b^2}\right]\sqrt{\frac{D}{\bar{m}}} \qquad (m = 1,2,3,\ldots \text{ and } n = 1,2,3,\ldots) \qquad (4.5)$$

where $W(x,y)$ is the shape function, $T(t)$ is the characteristic time function, $W_{mn}$ is the amplitude coefficient determined from initial conditions, and $\bar{m}$ is the mass per unit area. The mass per unit area can be defined as follows:

$$\bar{m} = \frac{\gamma\, t}{g} = \rho\, t \qquad (4.6)$$

where $\gamma$ is the specific weight of the material, $g$ is the gravitational acceleration, $\rho$ is the mass density, and $t$ is the plate thickness.

A shape function, $W(x,y)$, contains information about the relative displacements of the structure at a particular frequency. The relative displacements, often referred to as mode shapes, are always a function of position. In the case of a plate the relative out-of-plane displacements are a function of coordinates $x$ and $y$. The theoretical mode shapes for the first seven modes, in order of frequency, of a simply supported plate were generated using the numerical software Mathematica® [4.3]. Figure 4.2 shows each of these shapes in both a three-dimensional and a two-dimensional contour plot.

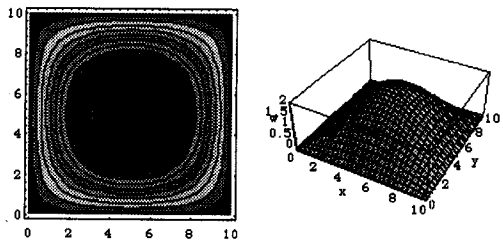

Mode 1 ($m = 1, n = 1$)

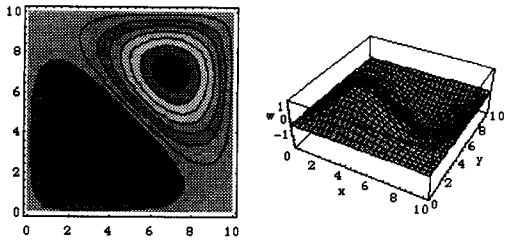

Mode 2 ($m = 1, n = 2$)

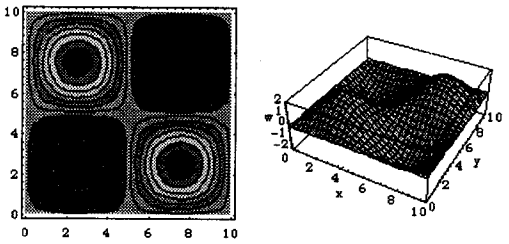

Mode 3 ($m = 2, n = 2$)

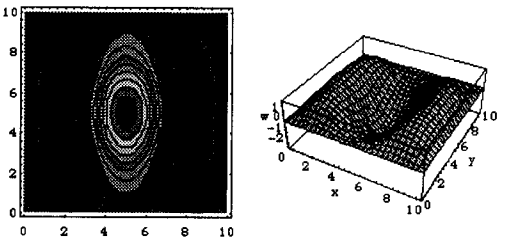

Mode 4 ($m = 1, n = 3$)

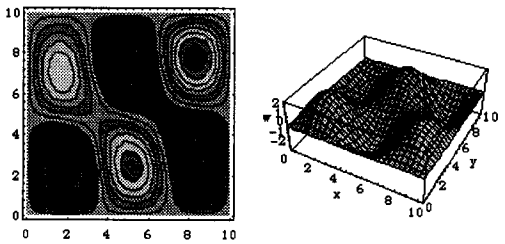

Mode 5 ($m = 2, n = 3$)

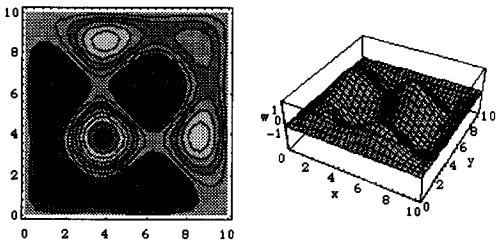

Mode 6 ($m = 1, n = 4$)

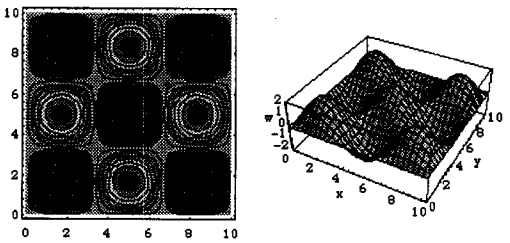

Mode 7 ($m = 3, n = 3$)

Fig. 4.2. Mode shapes for simply supported square plate, generated with the numerical software Mathematica® [4.3].

The frequency response of thin clamped plates can be described by the following [4.4]:

$$\omega_{mn} = \frac{\lambda_{mn}}{b^2}\sqrt{\frac{D}{\bar{m}}} \qquad (m = 1,2,3,\ldots \text{ and } n = 1,2,3,\ldots) \tag{4.7}$$

where $\lambda_{mn}$ is a frequency constant and is listed in Table 4.1. The dynamic deflection response is more complex than the simply supported equation (see Eqn. 4.4) but the general shape is similar (see Fig. 4.2). Since the deflection equation, $w(x,y,t)$, for a clamped plate is not used in this thesis the equation has been omitted.

Table 4.1. Frequency constants for clamped plate [4.4].

| $(m, n)$ | $\lambda_{mn}$ |
|---|---|
| 1,1 | 35.975 |
| 1,2 | 73.363 |
| 2,2 | 108.126 |
| 1,3 | 131.51 |
| 2,3 | 164.821 |
| 1,4 | 210.383 |
| 3,3 | 219.69 |

## 4.3 Solid Plate Analysis

### 4.3.1 Geometric Modeling and Meshing

Solid plate models were constructed within the finite element (FE) software package ANSYS® [4.5]. The material properties and geometry used to generate each model were the same and are defined in Table 4.2.

Table 4.2. Properties for a solid plate model [4.6].

| Material | 6061-T6 Aluminum |
|---|---|
| Poisson's ratio, $\nu$ | 0.32 |
| Young's Modulus, $E$ | $10.0 \times 10^6$ lb/in$^2$ |
| Density, $\rho$ | $2.536 \times 10^{-4}$ lb-s$^2$/in$^4$ |
| Thickness, $t$ | 0.125 in |
| Plate width, $a$ | 10 in |
| Plate length, $b$ | 10 in |

Meshing the solid plate models was also done within ANSYS®. Of the 120 different elements available only a few were considered. By using thin plates, as discussed previously, the number of possible elements applicable to this analysis was reduced to two shell elements (see Table 4.3). Both of these elements can be meshed over two-dimensional geometry and both can have the same mesh. The difference between the two is the number of nodes, and thus, the shape functions used in the analysis. A solid square plate, possibly meshed with either element, is shown in Fig. 4.3. Figure 4.3 does not necessarily display an optimum mesh density.

Table 4.3. Comparison of ANSYS® shell elements.

| Element name | No. of nodes | No. of nodal D.O.F | Deformation shape | Important characteristics |
|---|---|---|---|---|
| SHELL63 | 4 | 6 | Linear in both in-plane directions | Includes bending and membrane capabilities. |
| SHELL93 | 8 | 6 | Quadratic in both in-plane directions | Mid-side node makes this element well suited to model curvature around holes. It includes bending and membrane capabilities. Non-linear capabilities include stress stiffening and large deflection theory. |

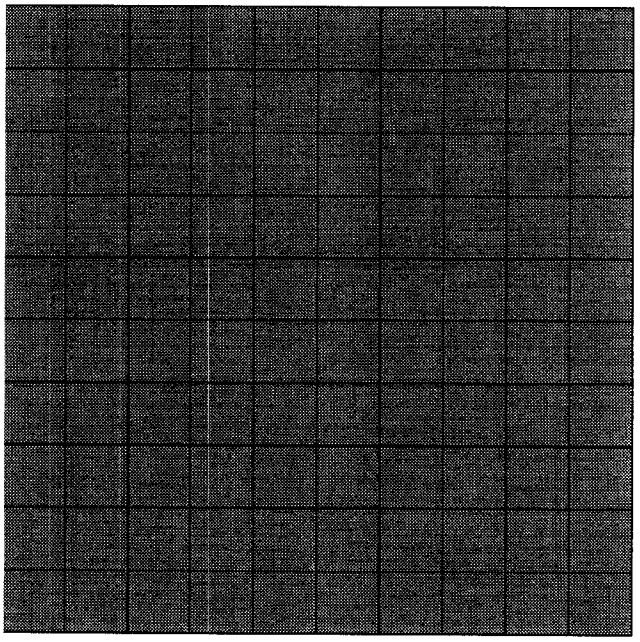

Fig. 4.3. Solid square plate model meshed with ANSYS®.

### 4.3.2 Nodal Static Loading

Moment distributions on parallel edges must be applied at nodes in such a way as to simulate a uniform edge moment. Consistent nodal loading does this. When used correctly the deflection contours for the simply supported plate will look like the ones in Fig. 4.4. Consistent nodal loading for 4-node and 8-node elements is shown in Fig. 4.5. They are calculated using the following relationship [4.7]:

$$\{r_e\} = \int_0^L [N]^T q ds \tag{4.8}$$

where the loading per unit length $q$ is $M_o$, $[N]^T$ is the element shape function, and $\{r_e\}$ is the load vector for consistent nodal loading.

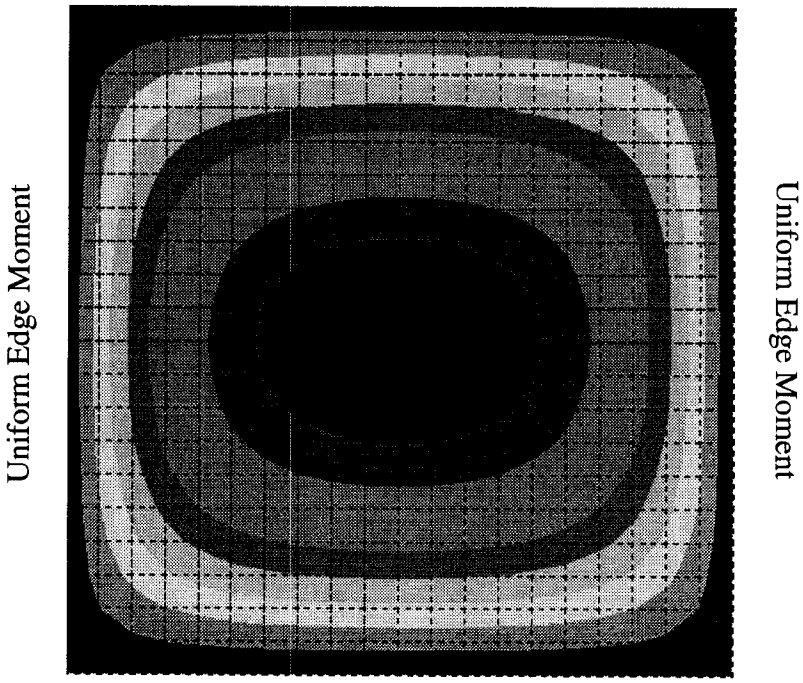


Fig. 4.4. Deflection contours for consistent nodal loading using full plate model. Edges are simply supported.

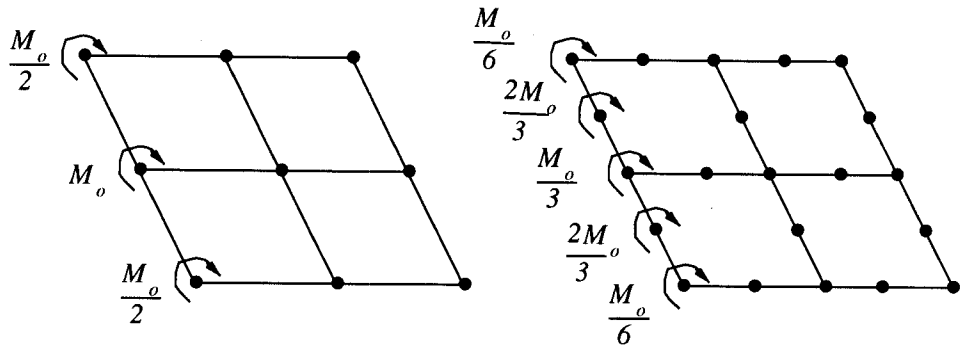


Fig. 4.5. Consistent nodal loading for 4-node and 8-node elements [4.7].

### 4.3.3 Finite Element Results

Solid plate models, based on the properties listed in Table 4.2, were analyzed using the FE software ANSYS®. Results show that SHELL63, the 4-node elastic shell element, more nearly approximates theory for the maximum static deflection (Fig. 4.6), the dynamic mode 1,1 (Fig. 4.7), and the dynamic mode 1,3 (Fig. 4.8). Also shown in Fig. 4.6 are the results of a nonlinear analysis using SHELL93, the 8-node structural shell element, indicating that the thin plate does not exhibit membrane behavior. The higher order 8-node element would seem to be a better choice for a perforated plate analysis because it is well suited to model curvature around holes but results here show it inaccurately predicts the static behavior of a plate. Table 4.4 lists a summary of element convergence.

Two dimensional mode shape plots were also generated on the finite element (FE) software ANSYS® (see Fig. 4.9). Shell63, the 4-node element, was used to generate the mode shapes.

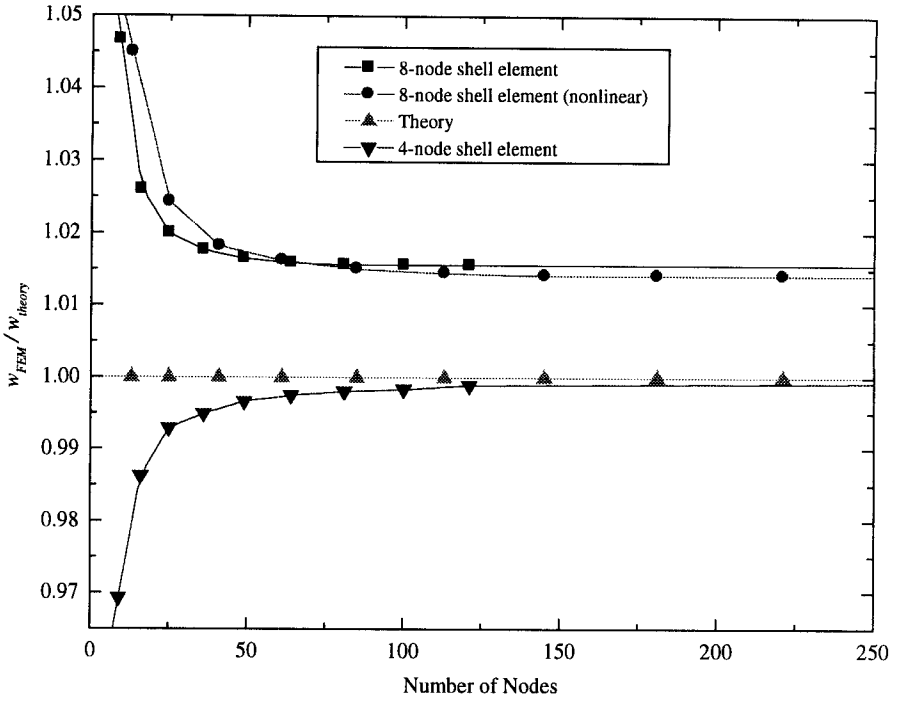


Fig. 4.6. Mesh convergence for static loading of solid plate.

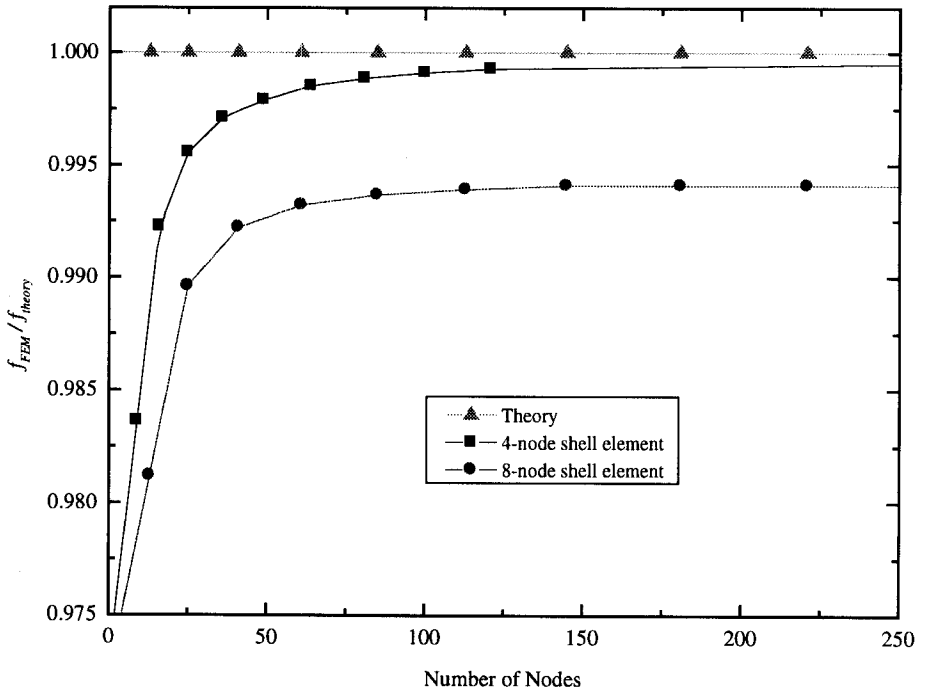


Fig. 4.7. Mesh convergence for fundamental mode of solid plate.

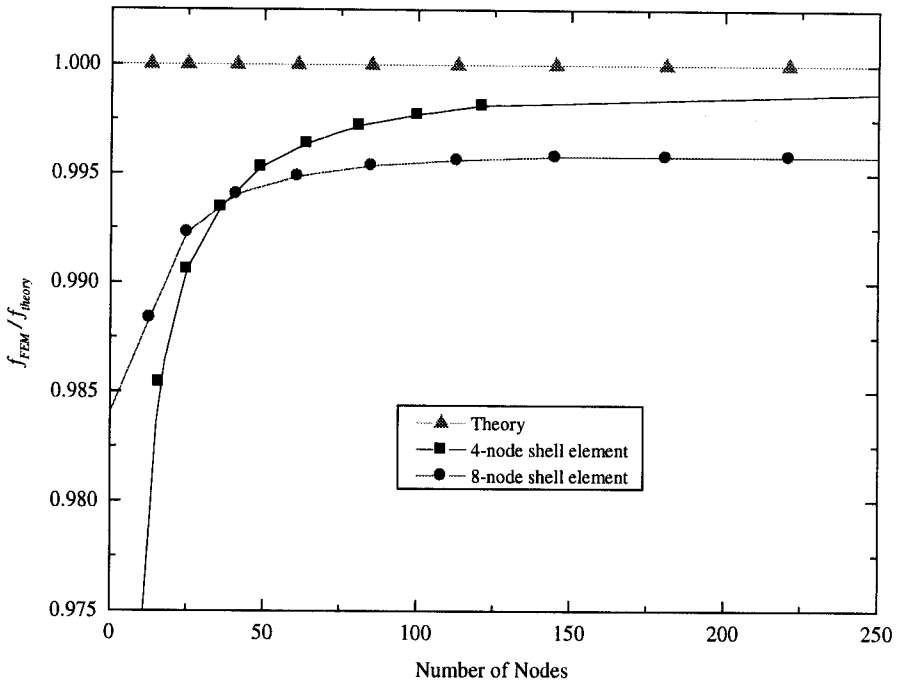


Fig. 4.8. Mesh convergence for mode 4 (1,3) of solid plate.

Table 4.4. FEM error convergence for solid plate models.

| Analysis Type | Element | Total Nodes | Percentage Error |
|---|---|---|---|
| Static | 4-node | 841 | 0.0215% |
| Static | 8-node | 841 | 1.5595% |
| Static | 8-node nonlinear | 841 | 1.3870% |
| Modal | 4-node (mode 1,1) | 841 | 0.0100% |
| Modal | 8-node (mode 1,1) | 841 | 0.5921% |
| Modal | 4-node (mode 1,3) | 841 | 0.0437% |
| Modal | 8-node (mode 1,3) | 841 | 0.4206% |

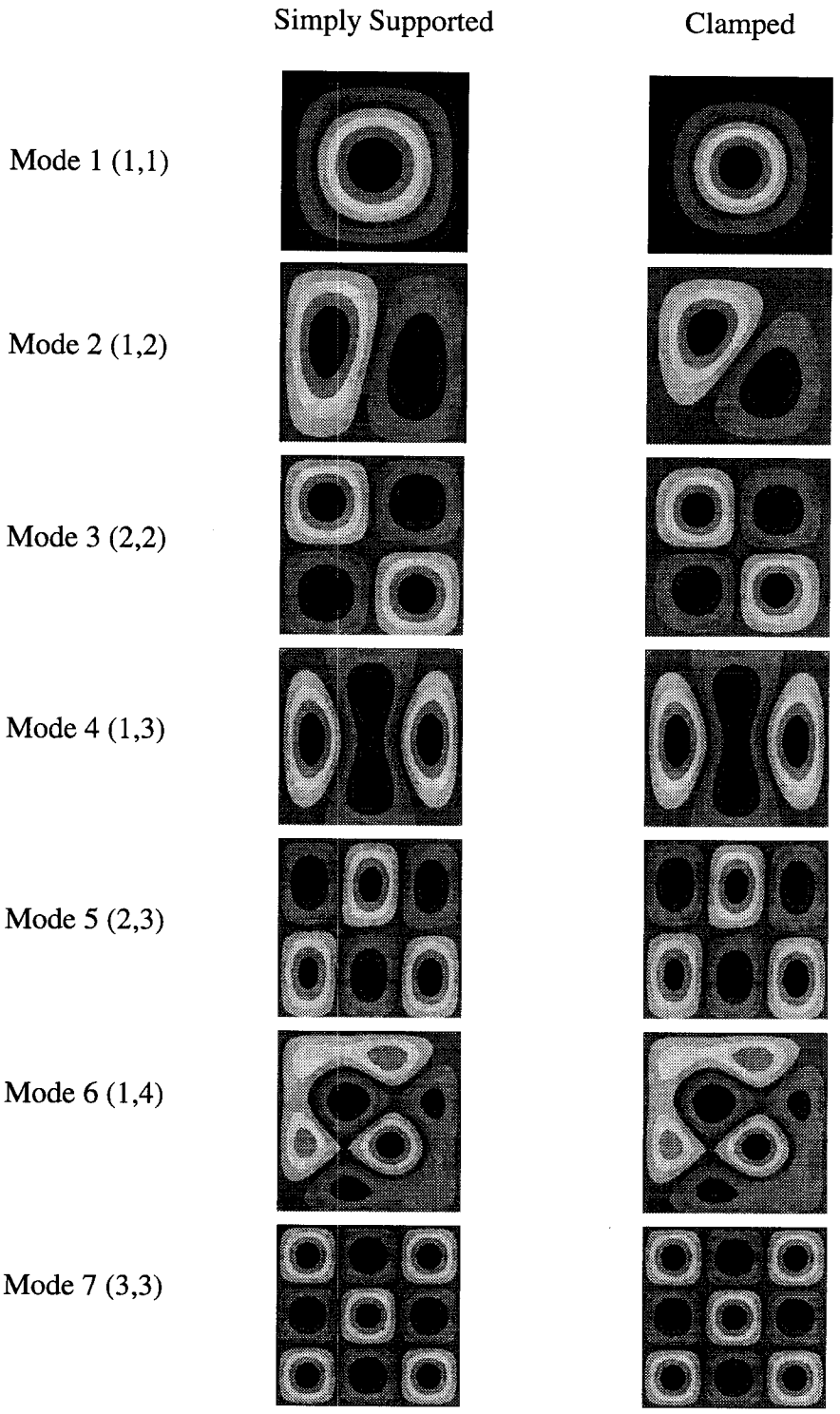


Fig. 4.9. Discrete mode shapes generated in ANSYS®.

## 4.4 Perforated Plate Theory

"Static" effective material constants, meant to be employed with perforated plates, are well documented and are commonly published in the form of design curves. They are denoted here as "static" because they were originally generated by subjecting the plate to a static structural load. All constants are plotted as a function of ligament efficiency, $\mu$, where the particular curve depends on parameters such as loading type, loading orientation, material thickness, and hole pattern. These design curve plots were developed, primarily through heat exchanger research, by graphing data from the experimental and/or numerical analysis.

Benchmarking FE models with published design curves is simplified by limiting the number of plate variables. For example, the previous work presented in this thesis (for the purpose of benchmarking) focused on thin, homogeneous, simply supported plates loaded in pure bending. Consequently, only the design curves on perforated plates subjected to pure bending are used for benchmarking the FE models.

## 4.5 Perforated Plate Analysis

### 4.5.1 Geometric Modeling and Meshing

Perforated plate models were also constructed within the FE software package ANSYS®. Each model was based on a basic solid plate model with the material properties and geometry listed in Table 4.2. A number of different models with perforations were generated from the basic model. Some of the parameters that were individually varied were Poisson's ratio, hole size, material density, and the perforation pattern. Varying the perforation hole size (see Table 4.5) indirectly varied ligament efficiency. It should be noted that the pitch, $P$, is held constant at a value of 2.0.

Table 4.5. Variations in ligament efficiency ($P = 2.0$).

| Hole diameter, $R$ | Ligament Efficiency, $\mu$ |
|---|---|
| 0 | 1.0 |
| 0.2 | 0.9 |
| 0.4 | 0.8 |
| 0.6 | 0.7 |
| 0.8 | 0.6 |
| 1.0 | 0.5 |
| 1.2 | 0.4 |
| 1.4 | 0.3 |
| 1.6 | 0.2 |
| 1.8 | 0.1 |

Once a solid model was defined the perforated plate models could be meshed in ANSYS® using the 4-node element SHELL63. A controlled mesh was constructed around a single hole using the most basic repeatable shape [4.8]. For example, the shape used in the square pattern is a square and the shape used in the triangular pattern is a hexagon (see Figs. 2.3 and 2.4). The basic shape, with a hole in the center, was then used like a building block to generate a plate with a number of perforations (see Fig. 4.10). Figure 4.9 is for illustration only and does not necessarily display an optimum mesh density.

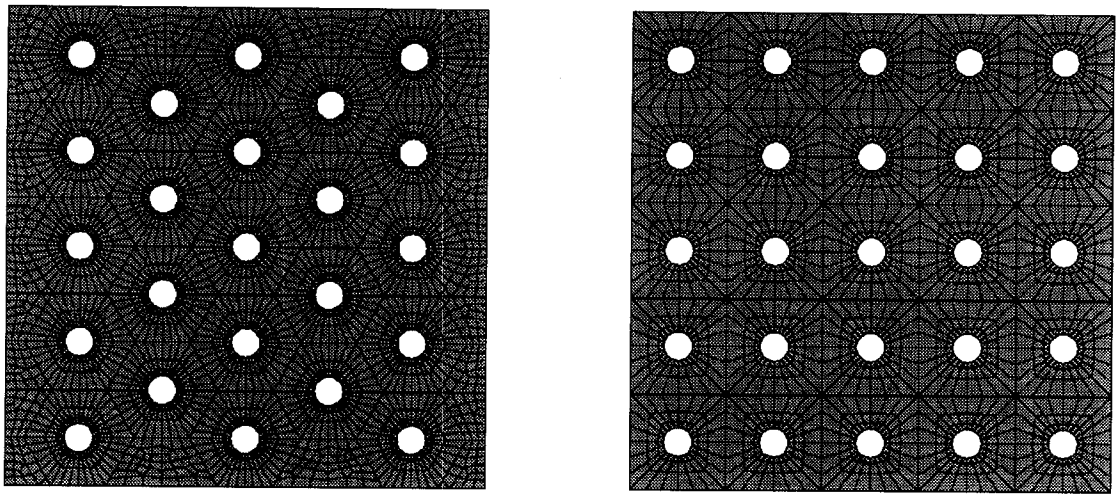

Fig. 4.10. Square and triangular pattern perforated plate models meshed with ANSYS®.

### 4.5.2 Nodal Static Loading

Consistent nodal loading vectors, defined in equation 4.6, were again applied as outlined in Section 4.3.2. When used correctly the deflection contours for the simply supported plate will look like the ones in Fig. 4.10. For reference, the consistent nodal loading for a 4-node element is shown in Fig. 4.5.

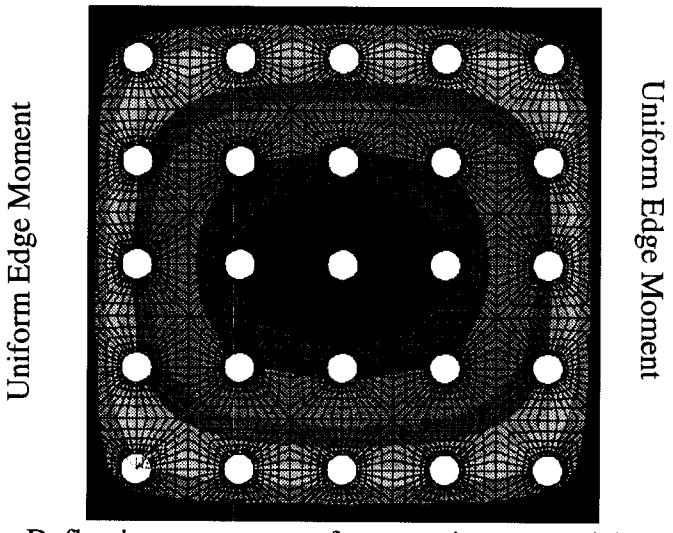


Fig. 4.11. Deflection contours for consistent nodal loading using perforated plate model. Edges are simply supported.

### 4.5.3 Finite Element Results

The FE results for the static deflection of two different perforated plates were compared to calculated deflections based on published data for static effective constants. The two plates were identical except for perforation hole size (also quantified as ligament efficiency). This procedure was repeated for the triangular and square mesh patterns to give two sets of data – two for each type of perforation pattern (Figs. 4.11 and 4.12). Using a 4-node shell element and mesh refinement, FE results with smaller ligament efficiencies converge to the published data. However, FE results become smaller than published data as ligament efficiency increases. The results from the square pattern show a 4.3% deviation and the results from the triangular pattern show a 3.3% deviation from effective material constant theory, both at a ligament efficiency of 0.20.

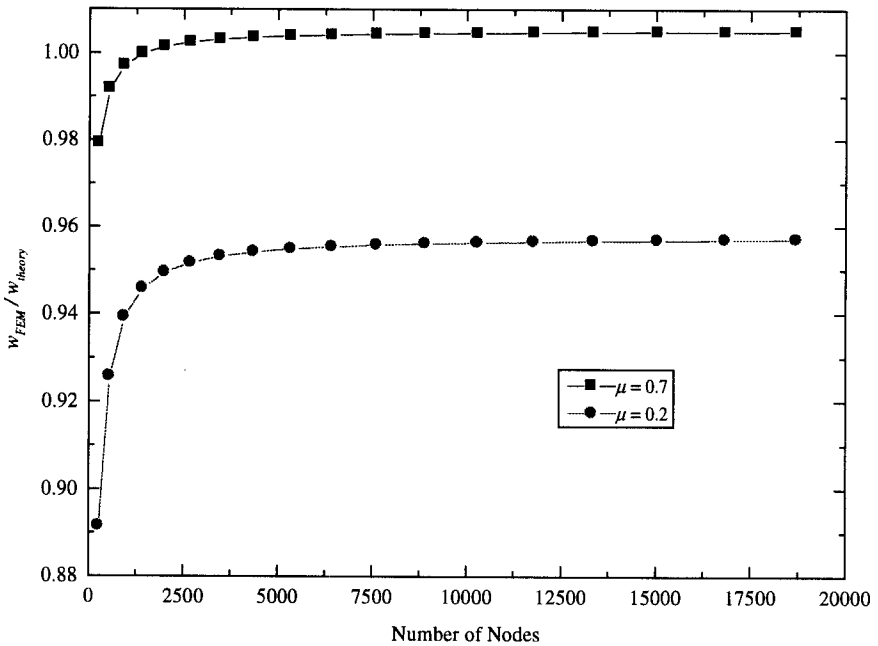


Fig. 4.12. Mesh convergence for static loading of plate perforated with square pattern and meshed with 4-node element (ANSYS® SHELL63).

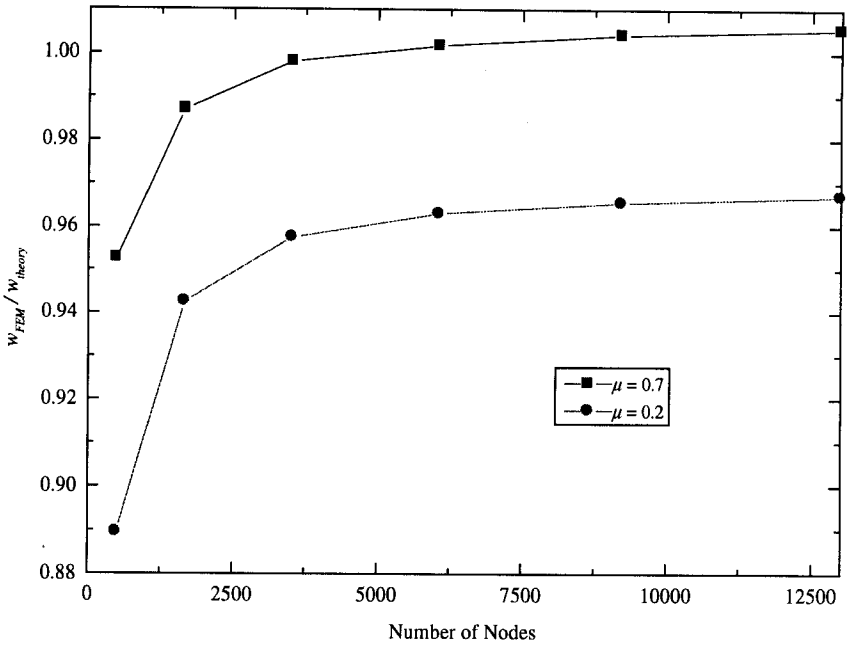


Fig. 4.13. Mesh convergence for static loading of plate perforated with triangular pattern and meshed with 4-node element (ANSYS® SHELL63).

## 4.6 References

[4.1] Ugural, A. C., *Stresses in Plates and Shells*, McGraw-Hill, Inc., pp. 75-77, 1981.

[4.2] Szilard, R., *Theory and Analysis of Plates: Classical and Numerical Methods*, Prentice-Hall, Inc., pp. 412-417, 1974.

[4.3] Mathematica® User's Manual, Wolfram Research, Inc., Version 2.2, 1994.

[4.4] Leissa, A. W., *Vibration of Shells*, NASA SP-288, pp. 58-65, 1973.

[4.5] ANSYS® Engineering Analysis Systems User's Manual, Houston, PA, Rev. 5.3, 1996.

[4.6] *ASM Specialty Handbook®* - *Aluminum and Aluminum Alloys*, ASM International, Materials Park, OH, pp. 685-686, 1993.

[4.7] Cook, R. D., Malkus, D. S., and Plesha, M. E., *Concepts and Applications of Finite Element Analysis*, Third Edition, John Wiley & Sons, Inc., 1989.

[4.8] Meguid, S. A., Kalamkarov, A. L., Yao, J., and Zougas, A., "Analytical, Numerical, and Experimental Studies of Effective Elastic Properties of Periodically Perforated Materials," *Journal of Engineering Materials and Technology*, Vol. 118, pp. 43-48, 1996.

# Chapter 5
# Dynamic Behavior of Perforated Plates

The dynamic analysis of perforated plates is based on the FE models developed in Chapter 4 and the concept of effective stiffness, $D^*$, presented in Chapter 2. Using ANSYS [5.1] to perform modal analyses with the FE models, natural frequencies and mode shapes were generated. The frequency results were then compiled and used to generate effective stiffness values for the respective plates.

## 5.1 Dynamic Effective Elastic Constants

Effective stiffness values are determined from backing out stiffness values from a governing equation where the all the parameters other than stiffness are known, including the response to loading. Known parameters include the overall dimensions of the plate, which is 10 in. × 10 in. × 0.125 in. As outlined in Chapter 2, the traditional way of determining the response was to statically load a plate and measure the deflection. In this thesis, however, modal frequencies generated through finite element methods (FEM) are used in conjunction with the frequency response equation to generate stiffness values. The resulting stiffness values are subsequently called the dynamic effective elastic constants.

### 5.1.1 Simply Supported Plate with Square Penetration Pattern

Finite element plate models were generated with a square perforation pattern and variable ligament efficiencies. Using simply supported boundary conditions, each model was analyzed and the modal frequencies computed. The resulting stiffness values from the first seven modes of vibration were plotted for the three different values of Poisson's ratio (see Figs. 5.1 – 5.3). For comparison purposes, the static

effective elastic constants are also shown on the plots. In addition to generating modal frequencies, mode shapes were generated for the first five modes of vibration (see Figs. 5.4 – 5.6). The shapes are only intended to supplement the stiffness values and therefore do not cover all seven modes used previously.

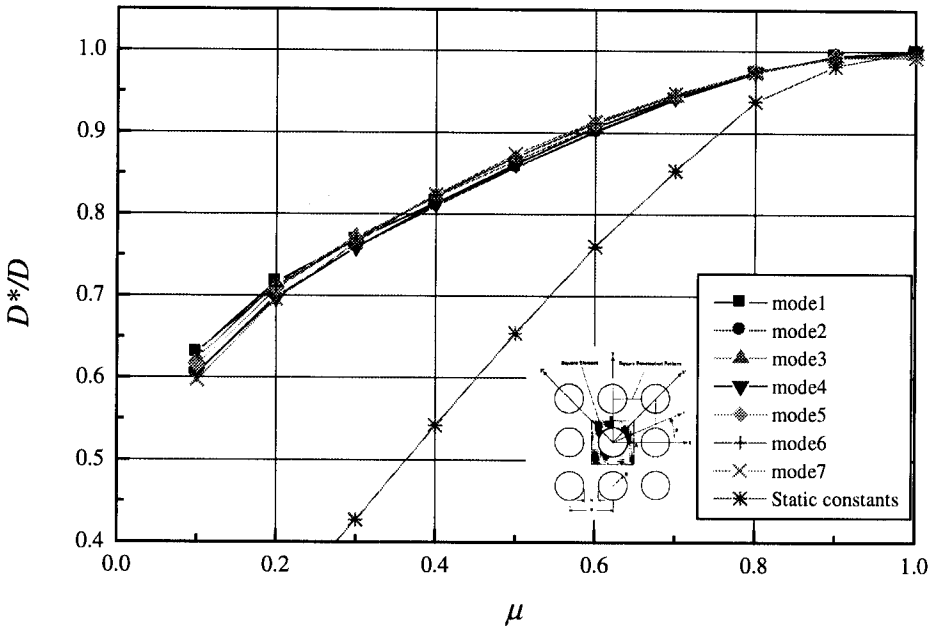


Fig. 5.1. Effective stiffness for square simply supported plate with a square perforation pattern ($\nu = 0.20$).

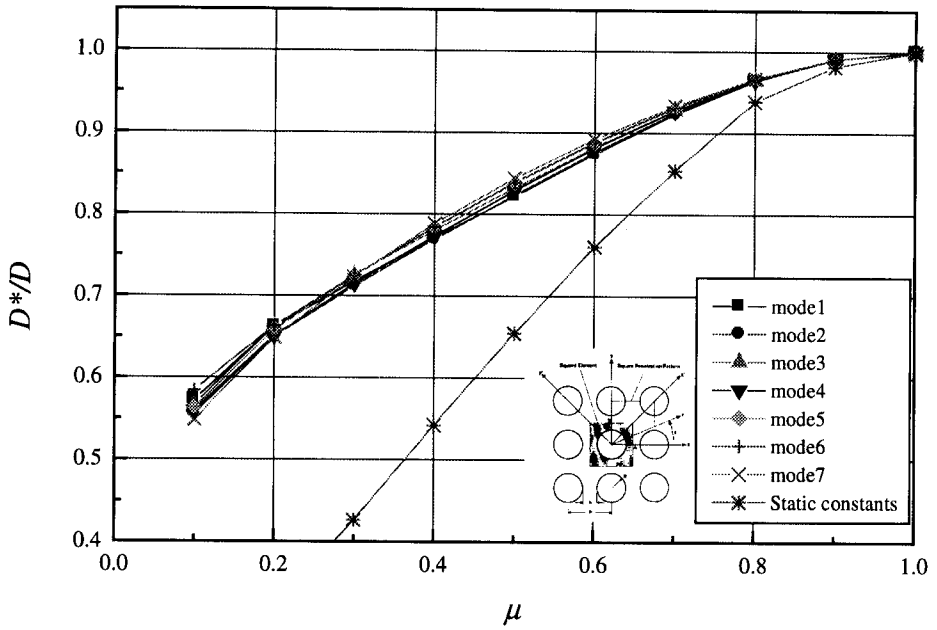


Fig. 5.2. Effective stiffness for square simply supported plate with a square perforation pattern ($\nu = 0.30$).

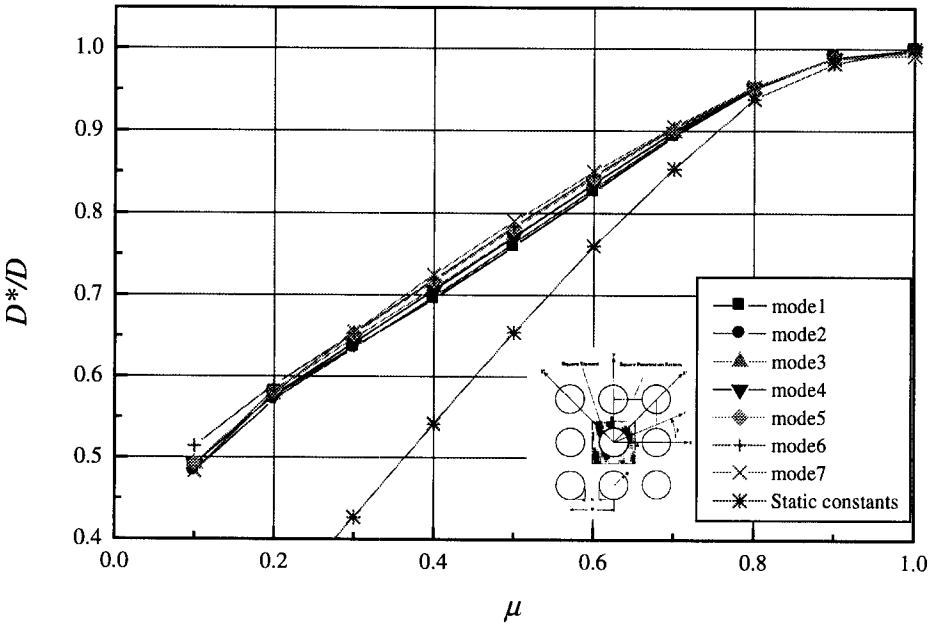


Fig. 5.3. Effective stiffness for square simply supported plate with a square perforation pattern ($\nu = 0.45$).

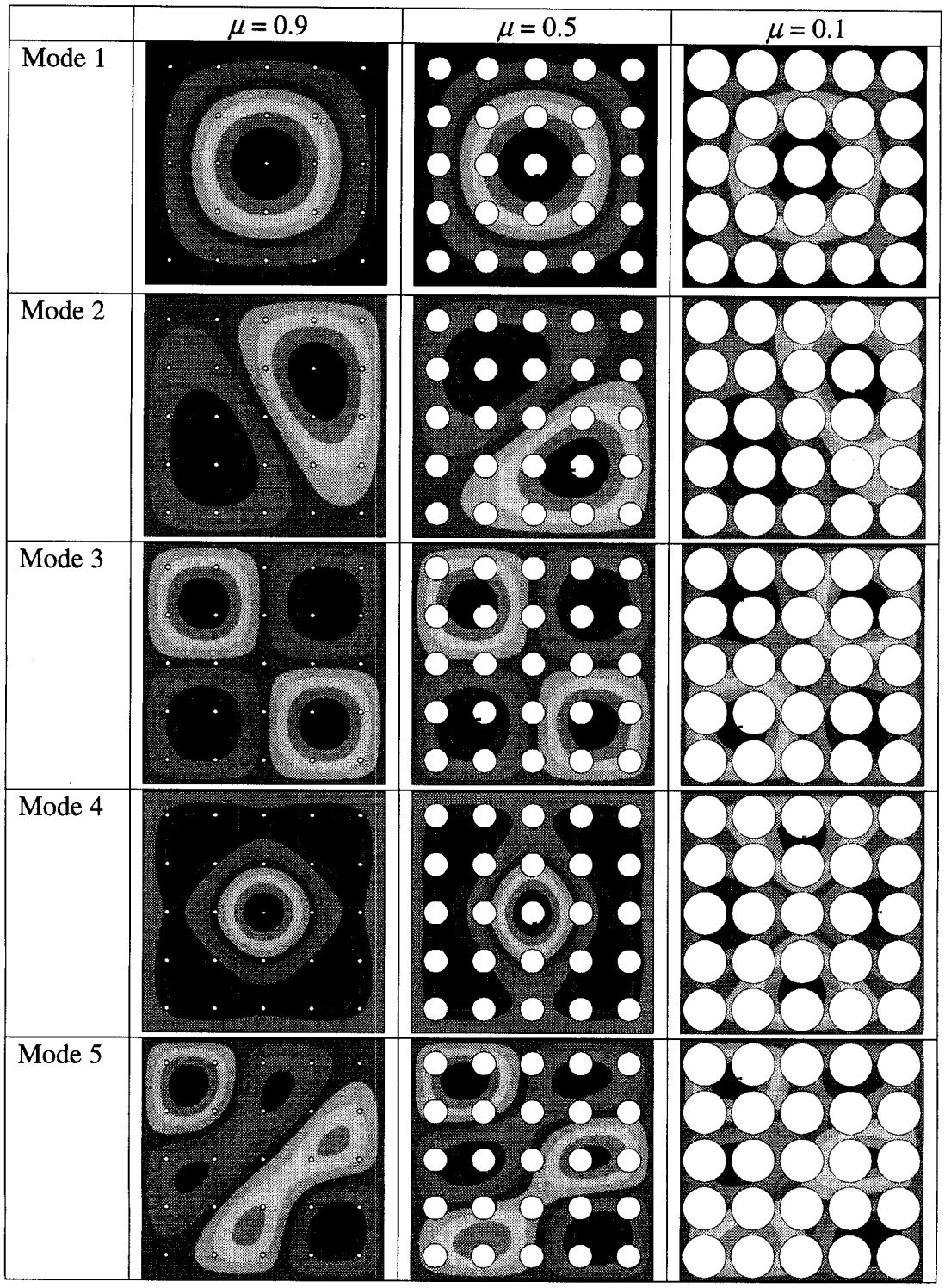


Fig. 5.4. ANSYS® output for simply supported plates with square perforation patterns ($P = 2.0$, $\upsilon = 0.20$).

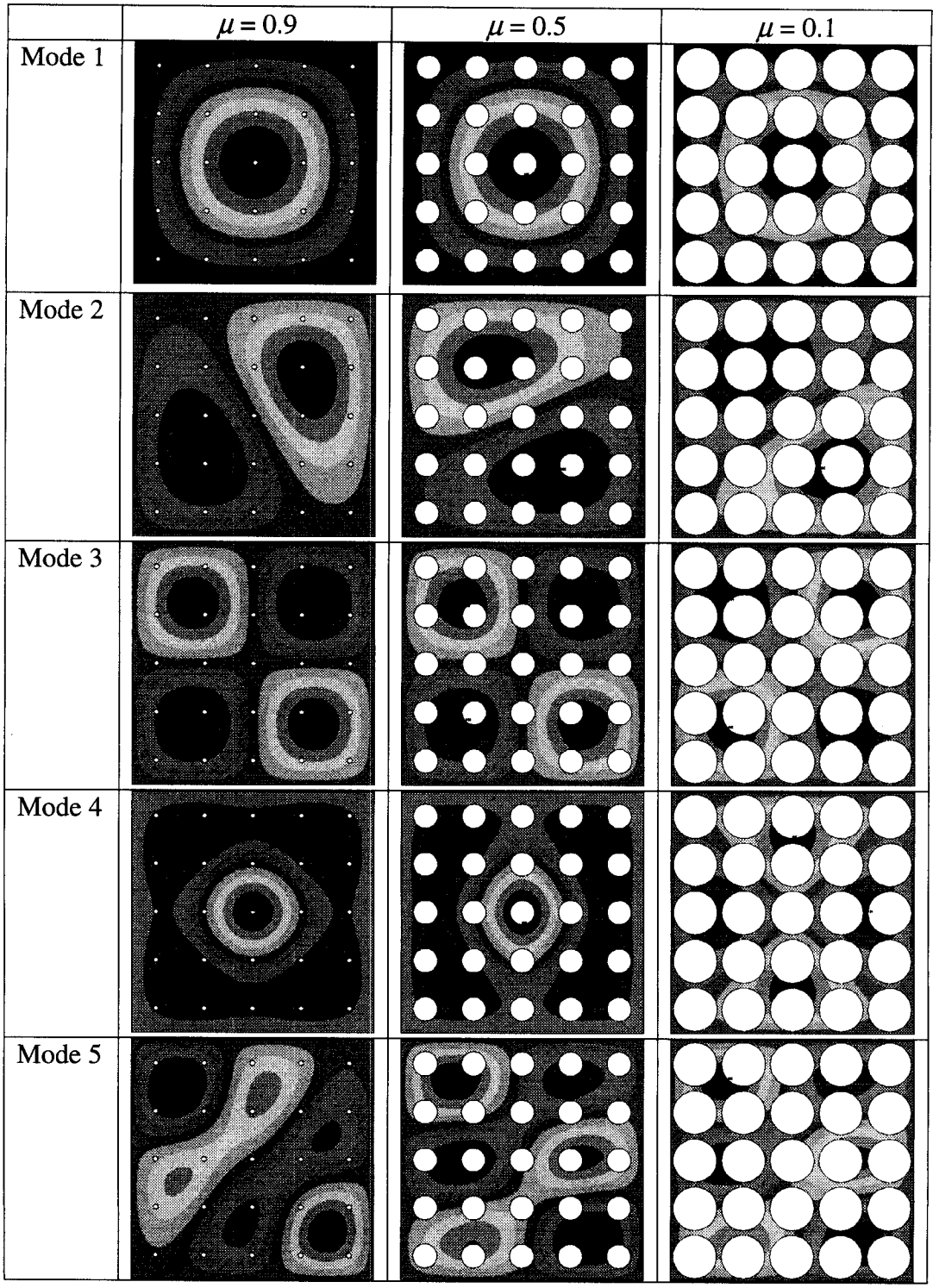


Fig. 5.5. ANSYS® output for simply supported plates with square perforation patterns ($P = 2.0$, $\upsilon = 0.30$).

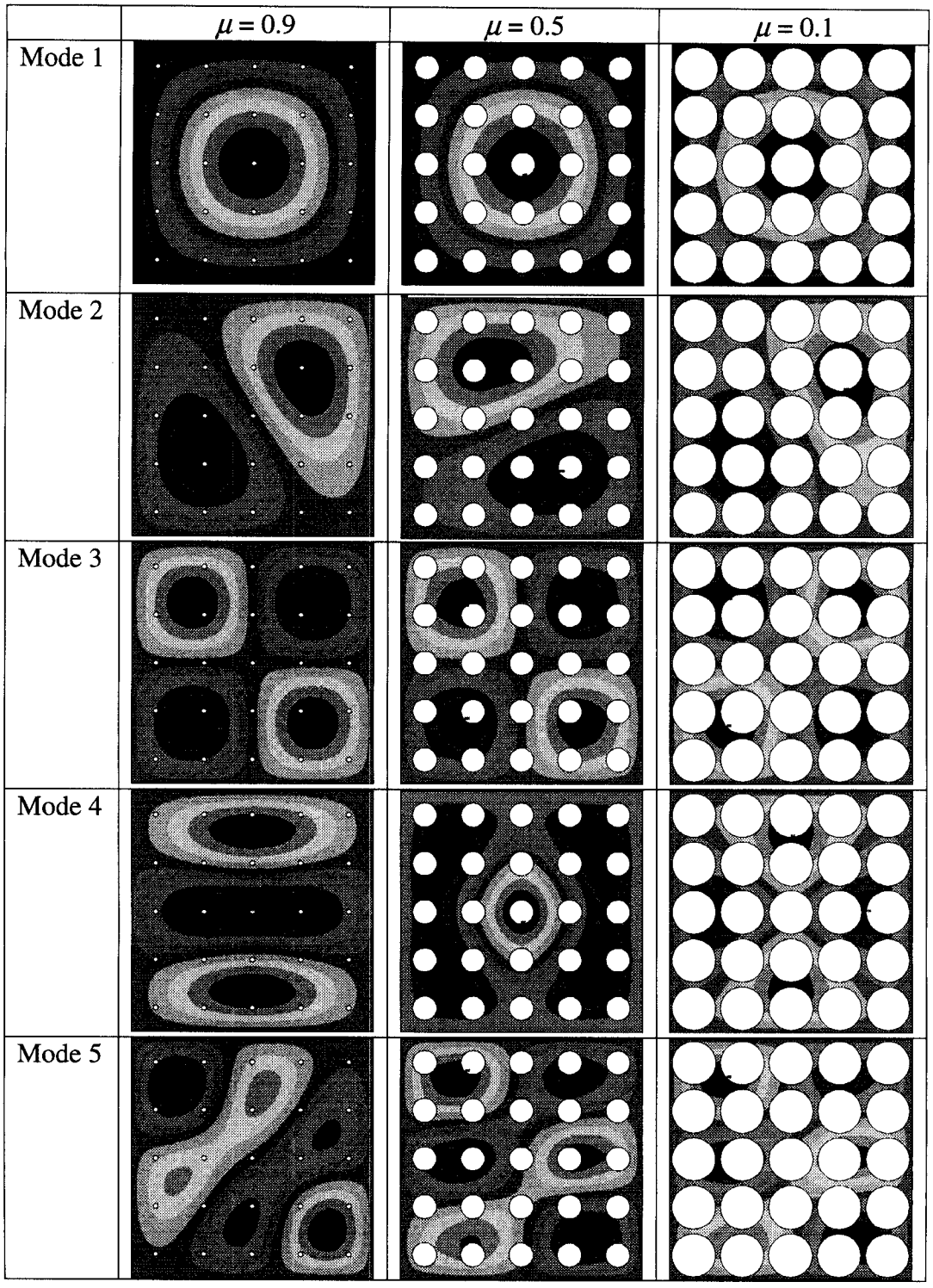


Fig. 5.6. ANSYS® output for simply supported plates with square perforation patterns ($P = 2.0$, $\upsilon = 0.45$).

### 5.1.2 Clamped Plate with Square Penetration Pattern

Finite element plate models were generated with a square perforation pattern and variable ligament efficiencies. Using clamped boundary conditions, each model was analyzed and the modal frequencies computed. The resulting stiffness values from the first seven modes of vibration were plotted for the three different values of Poisson's ratio (see Figs. 5.7 – 5.9). For comparison purposes, the static effective material constants are also shown on the plots. In addition to generating modal frequencies, mode shapes were generated for the first five modes of vibration (see Figs. 5.10 – 5.12). The shapes are only intended to supplement the stiffness values and therefore do not cover all seven modes used previously.

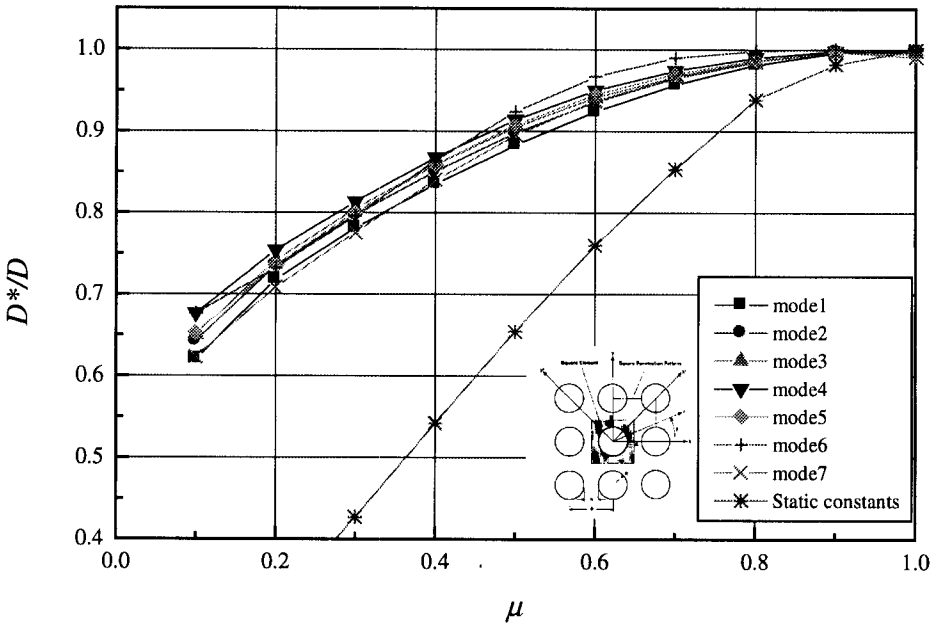


Fig. 5.7. Effective stiffness for square clamped plate with a square perforation pattern ($\nu = 0.20$).

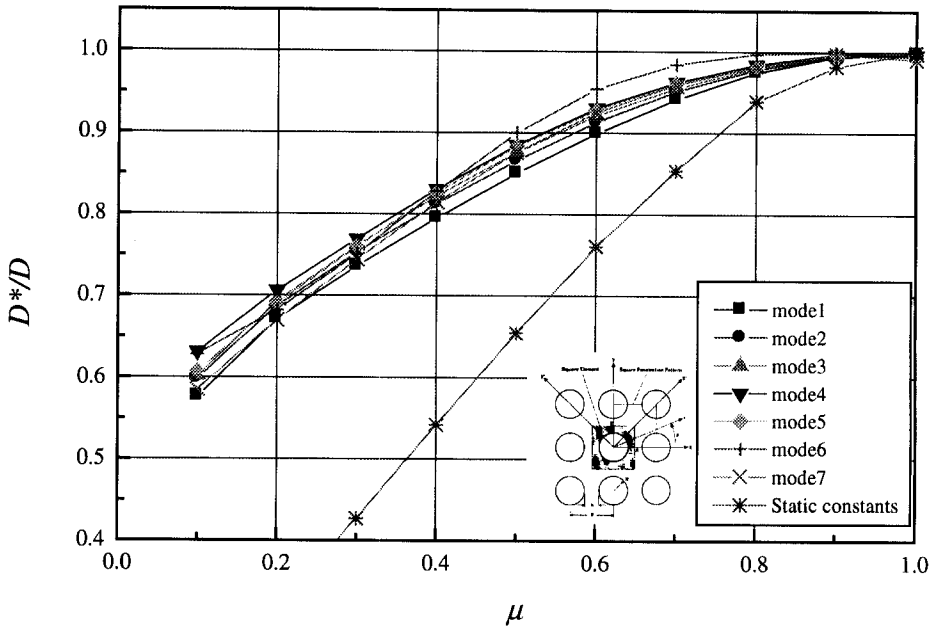


Fig. 5.8. Effective stiffness for square clamped plate with a square perforation pattern ($\nu = 0.30$).

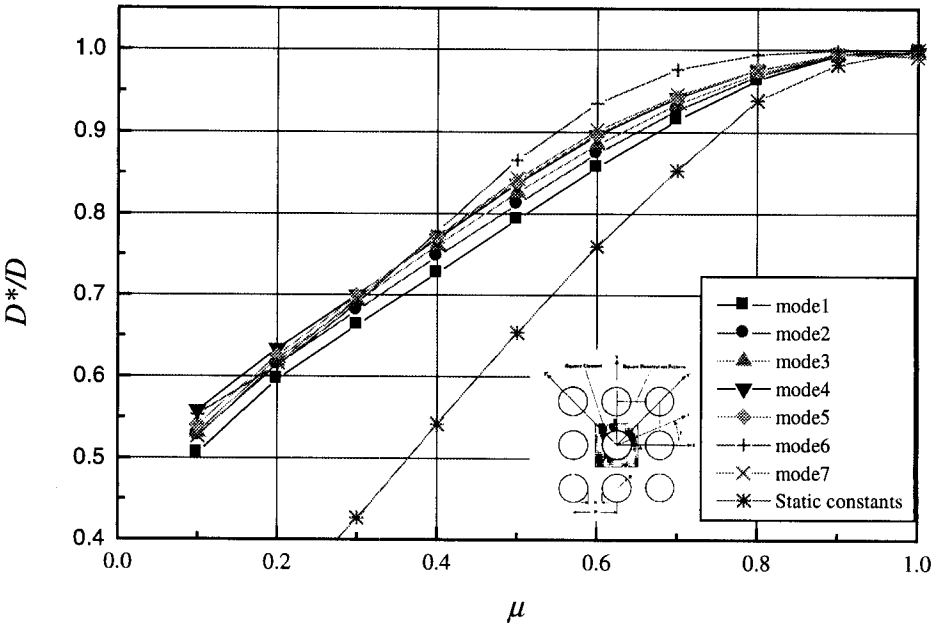


Fig. 5.9. Effective stiffness for square clamped plate with a square perforation pattern ($\nu = 0.45$).

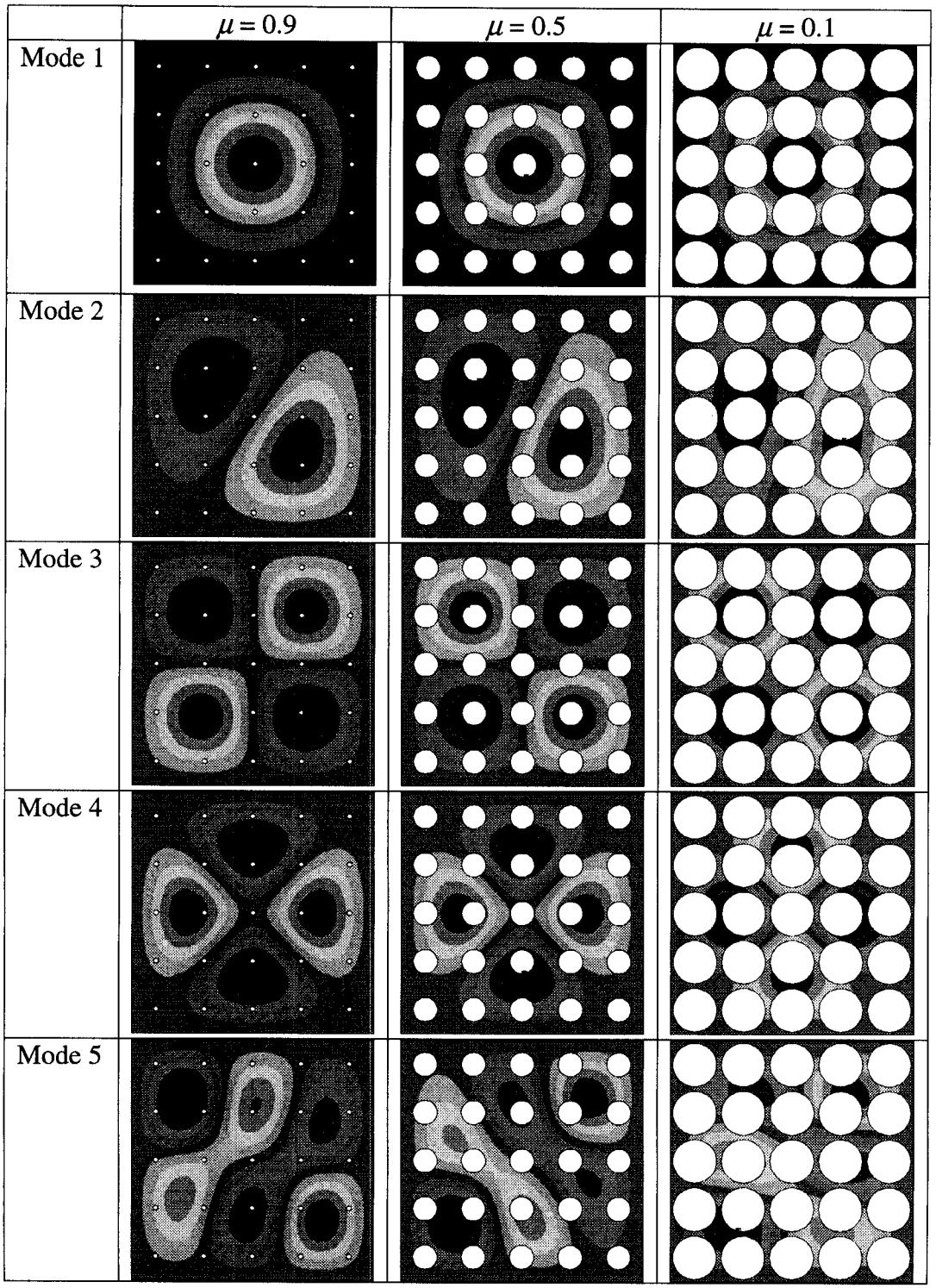


Fig. 5.10. ANSYS® output for clamped plates with square perforation patterns ($P = 2.0$, $\upsilon = 0.20$).

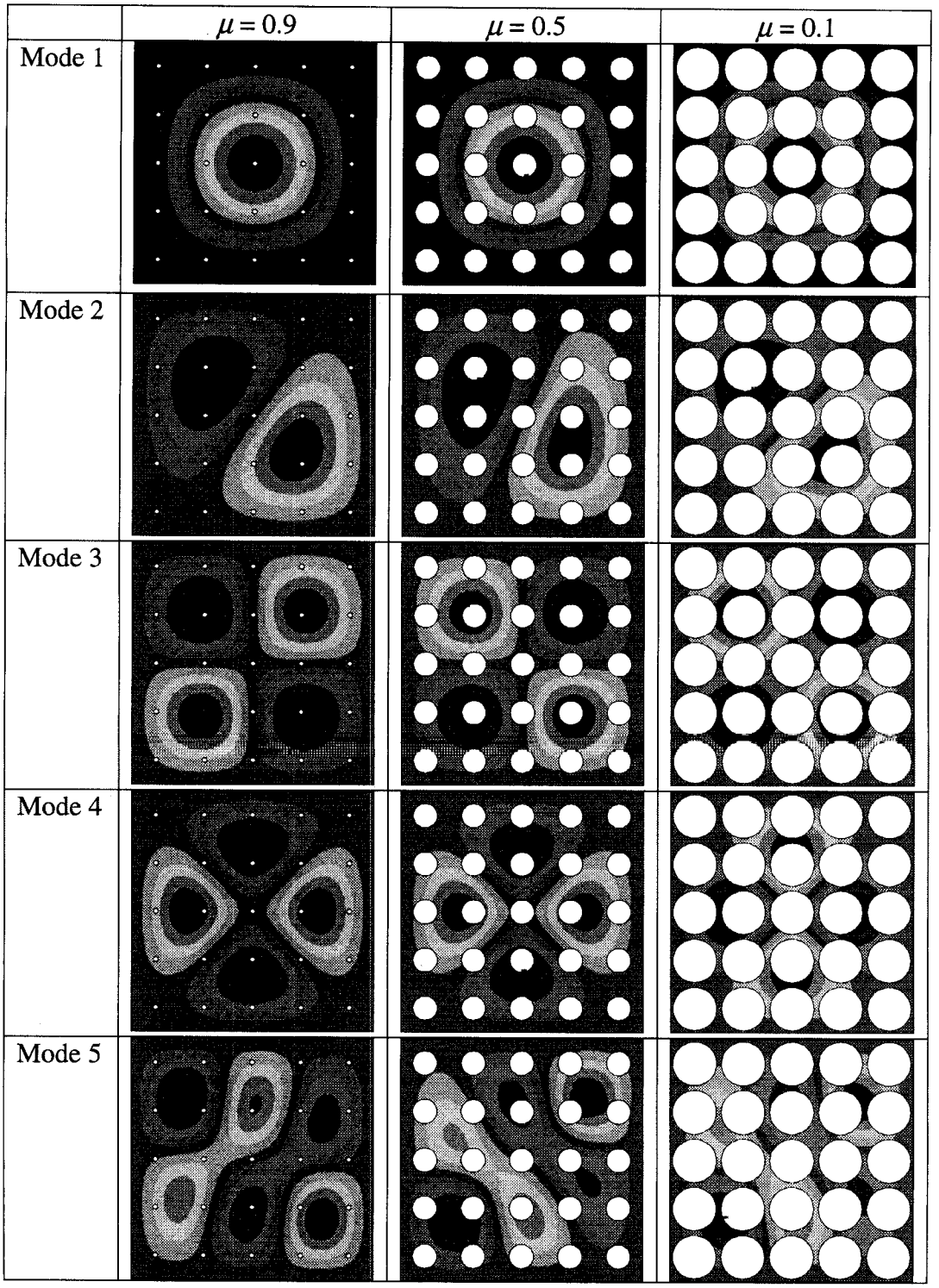


Fig. 5.11. ANSYS® output for clamped plates with square perforation patterns ($P = 2.0$, $\upsilon = 0.03$).

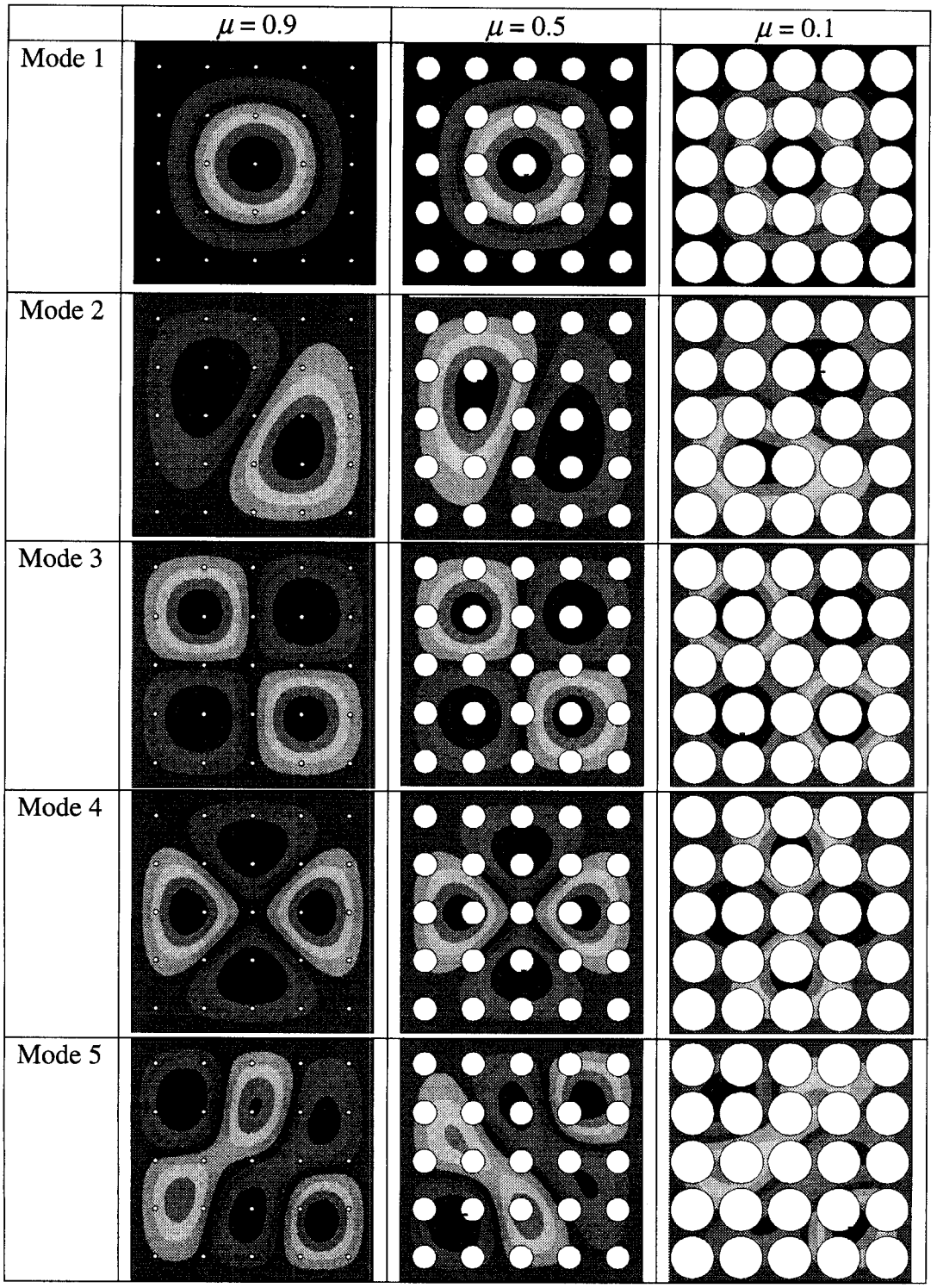


Fig. 5.12. ANSYS® output for clamped plates with square perforation patterns ($P = 2.0, \upsilon = 0.45$).

### 5.1.3 Simply Supported Plate with Triangular Penetration Pattern

Finite element plate models were generated with a triangular perforation pattern and variable ligament efficiencies. Using simply supported boundary conditions, each model was analyzed and the modal frequencies computed. The resulting stiffness values from the first seven modes of vibration were plotted for the three different values of Poisson's ratio (see Figs. 5.13 – 5.15). For comparison purposes, the static effective material constants are also shown on the plots. In addition to generating modal frequencies, mode shapes were generated for the first five modes of vibration (see Figs. 5.16 – 5.18). The shapes are only intended to supplement the stiffness values and therefore do not cover all seven modes used previously.

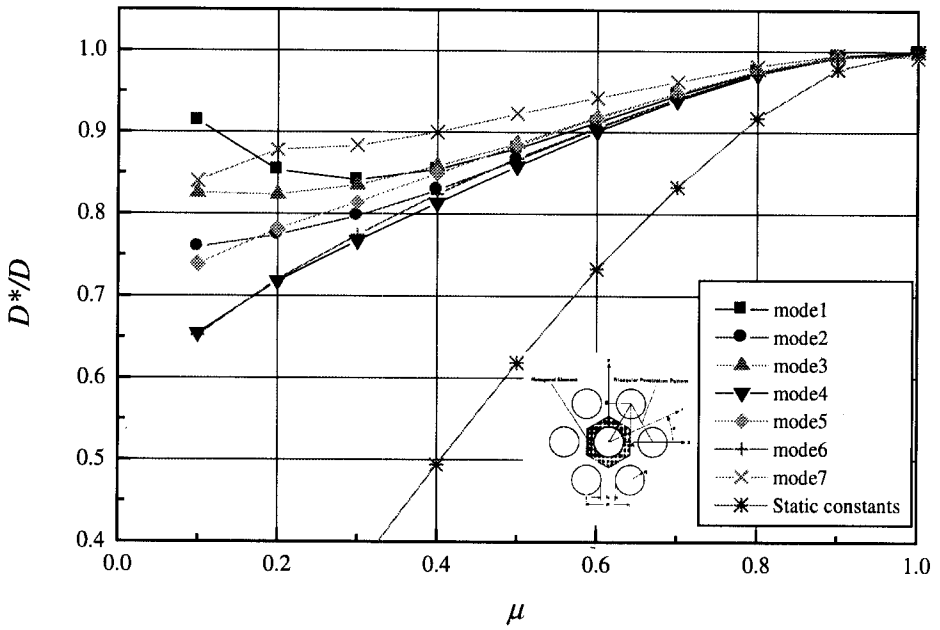


Fig. 5.13. Effective stiffness for square simply supported plate with a triangular perforation pattern ($\nu = 0.20$).

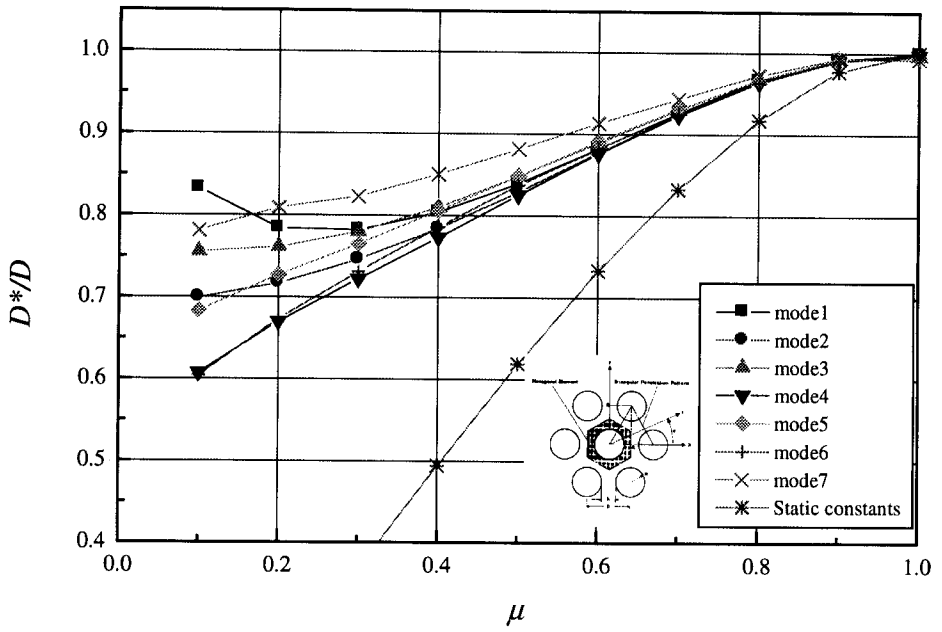


Fig. 5.14. Effective stiffness for square simply supported plate with a triangular perforation pattern ($\nu = 0.30$).

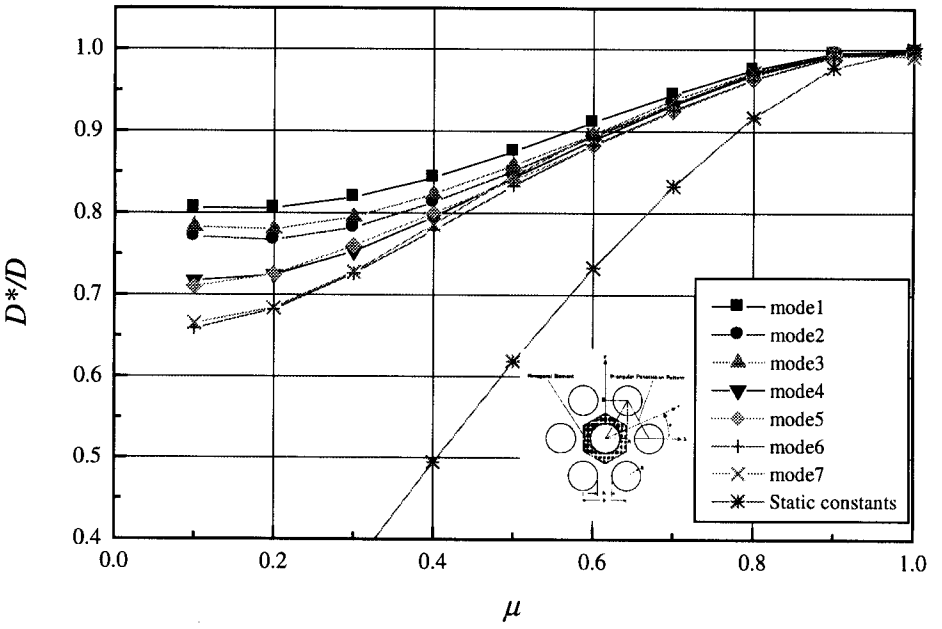


Fig. 5.15. Effective stiffness for square simply supported plate with a triangular perforation pattern ($\nu = 0.45$).

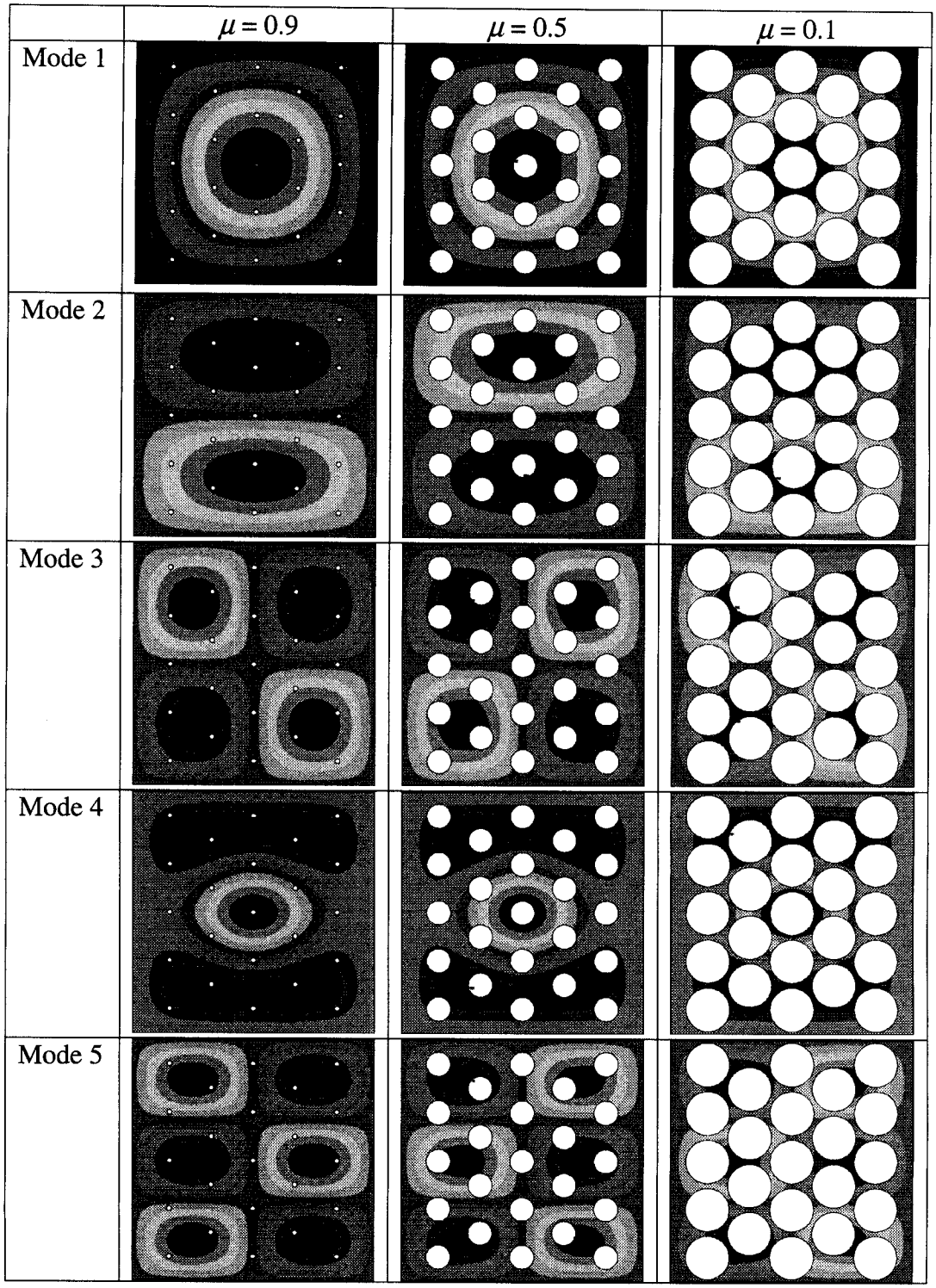


Fig. 5.16. ANSYS® output for simply supported plates with triangular perforation patterns ($P = 2.0$, $\upsilon = 0.20$).

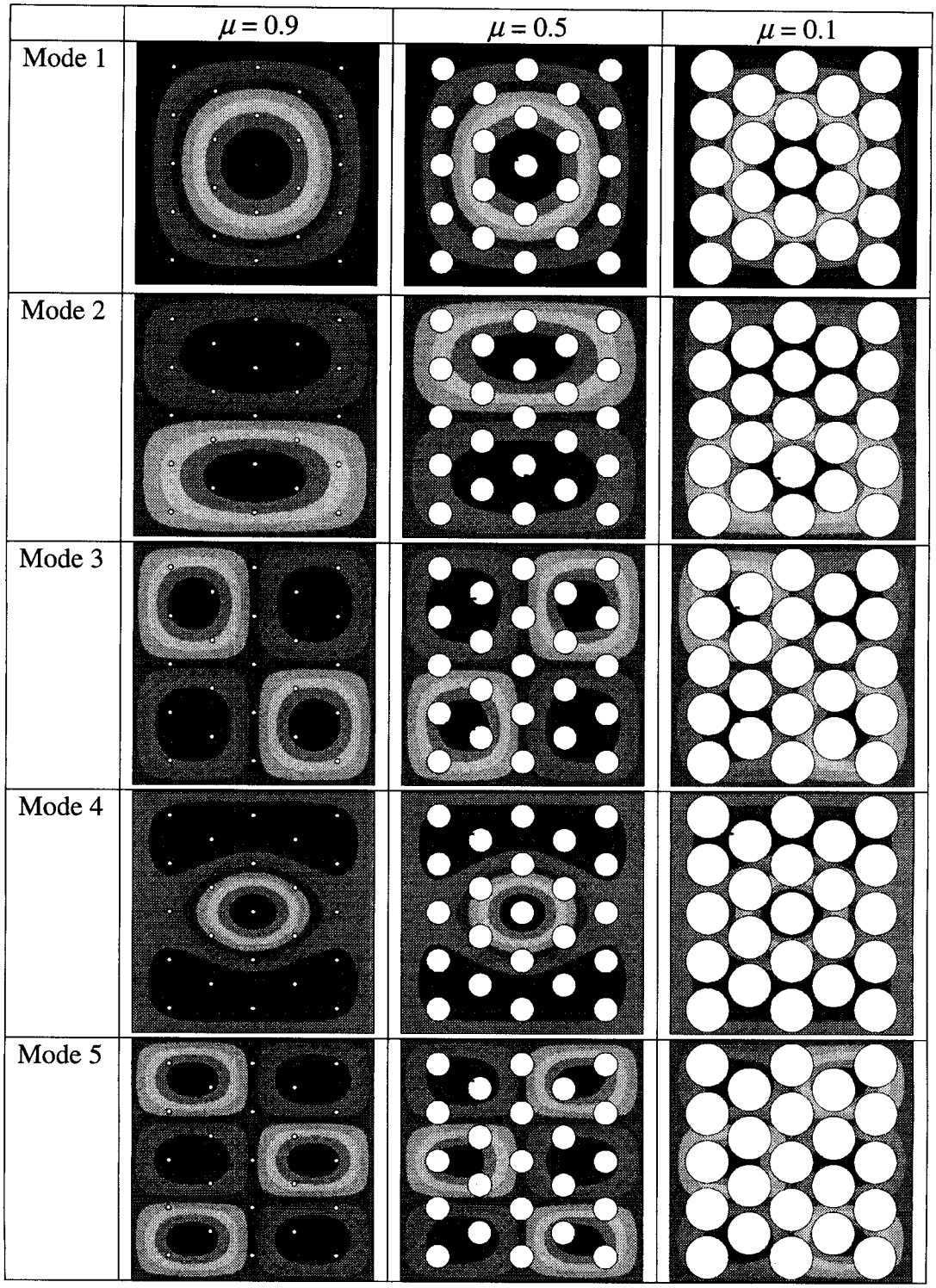


Fig. 5.17. ANSYS® output for simply supported plates with triangular perforation patterns ($P = 2.0$, $\upsilon = 0.30$).

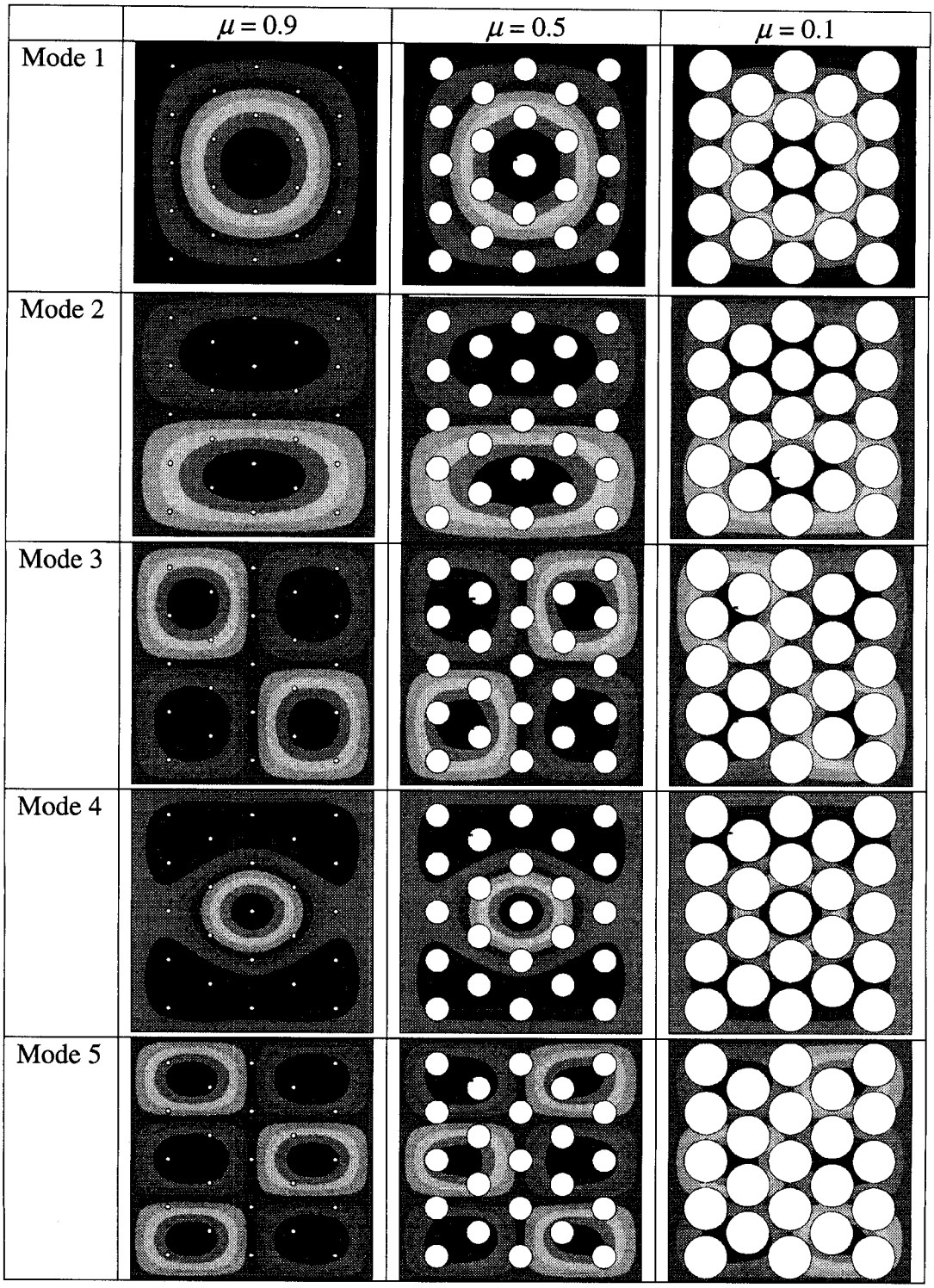


Fig. 5.18. ANSYS® output for simply supported plates with triangular perforation patterns ($P = 2.0$, $\upsilon = 0.45$).

### 5.1.4 Clamped Plate with Triangular Penetration Pattern

Finite element plate models were generated with a triangular perforation pattern and variable ligament efficiencies. Using clamped boundary conditions, each model was analyzed and the modal frequencies computed. The resulting stiffness values from the first seven modes of vibration were plotted for the three different values of Poisson's ratio (see Figs. 5.19 – 5.21). For comparison purposes, the static effective material constants are also shown on the plots. In addition to generating modal frequencies, mode shapes were generated for the first five modes of vibration (see Figs. 5.22 – 5.24). The shapes are only intended to supplement the stiffness values and therefore do not cover all seven modes used previously.

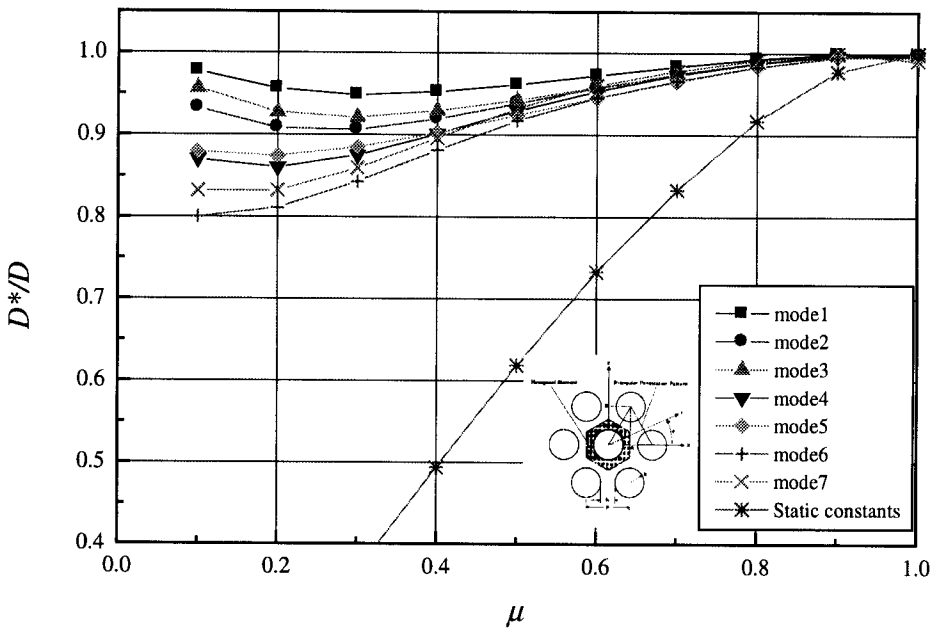


Fig. 5.19. Effective stiffness for square clamped plate with a triangular perforation pattern ($\nu = 0.20$).

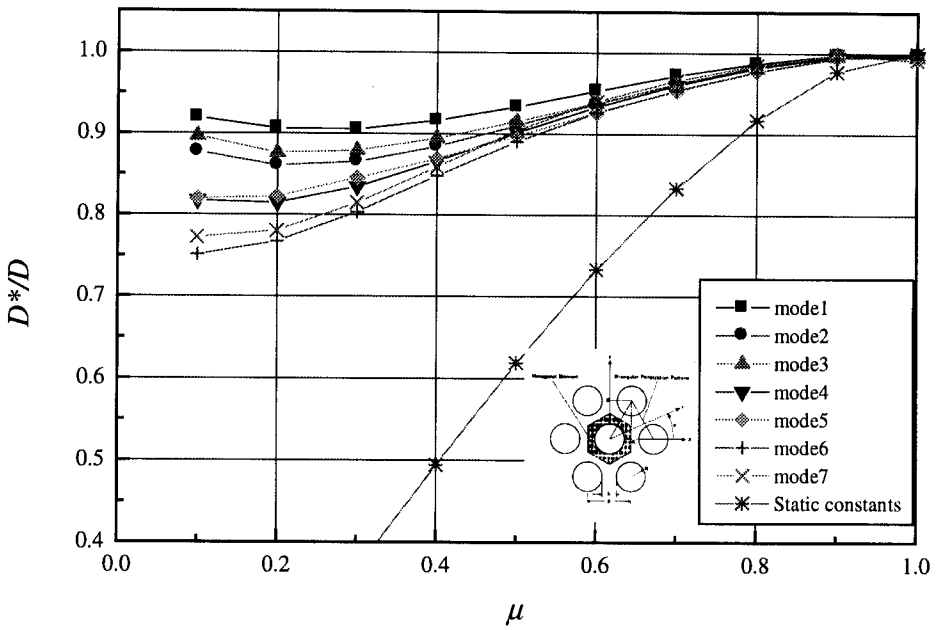


Fig. 5.20. Effective stiffness for square clamped plate with a triangular perforation pattern ($\nu = 0.30$).

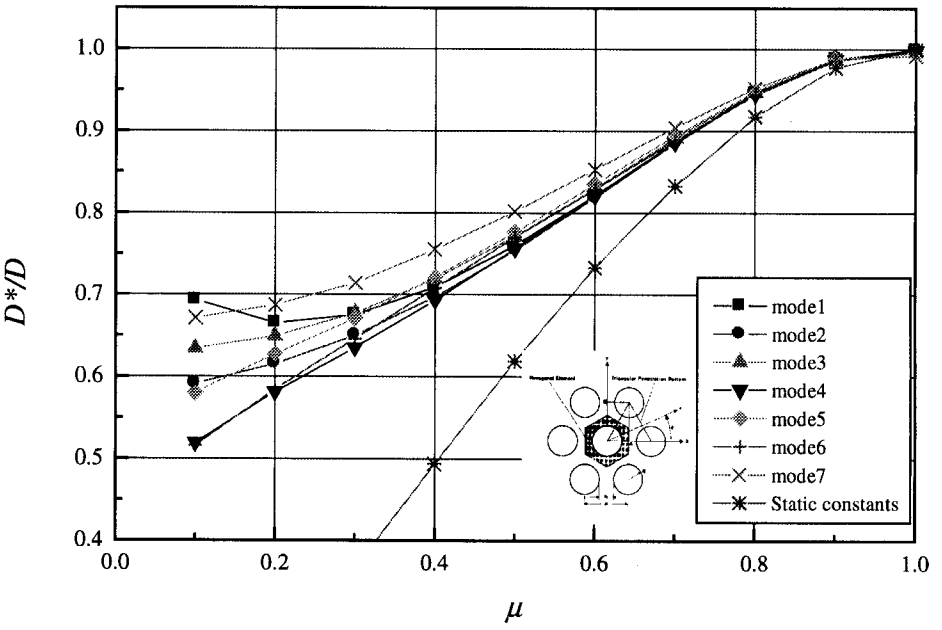


Fig. 5.21. Effective stiffness for square clamped plate with a triangular perforation pattern ($\nu = 0.45$).

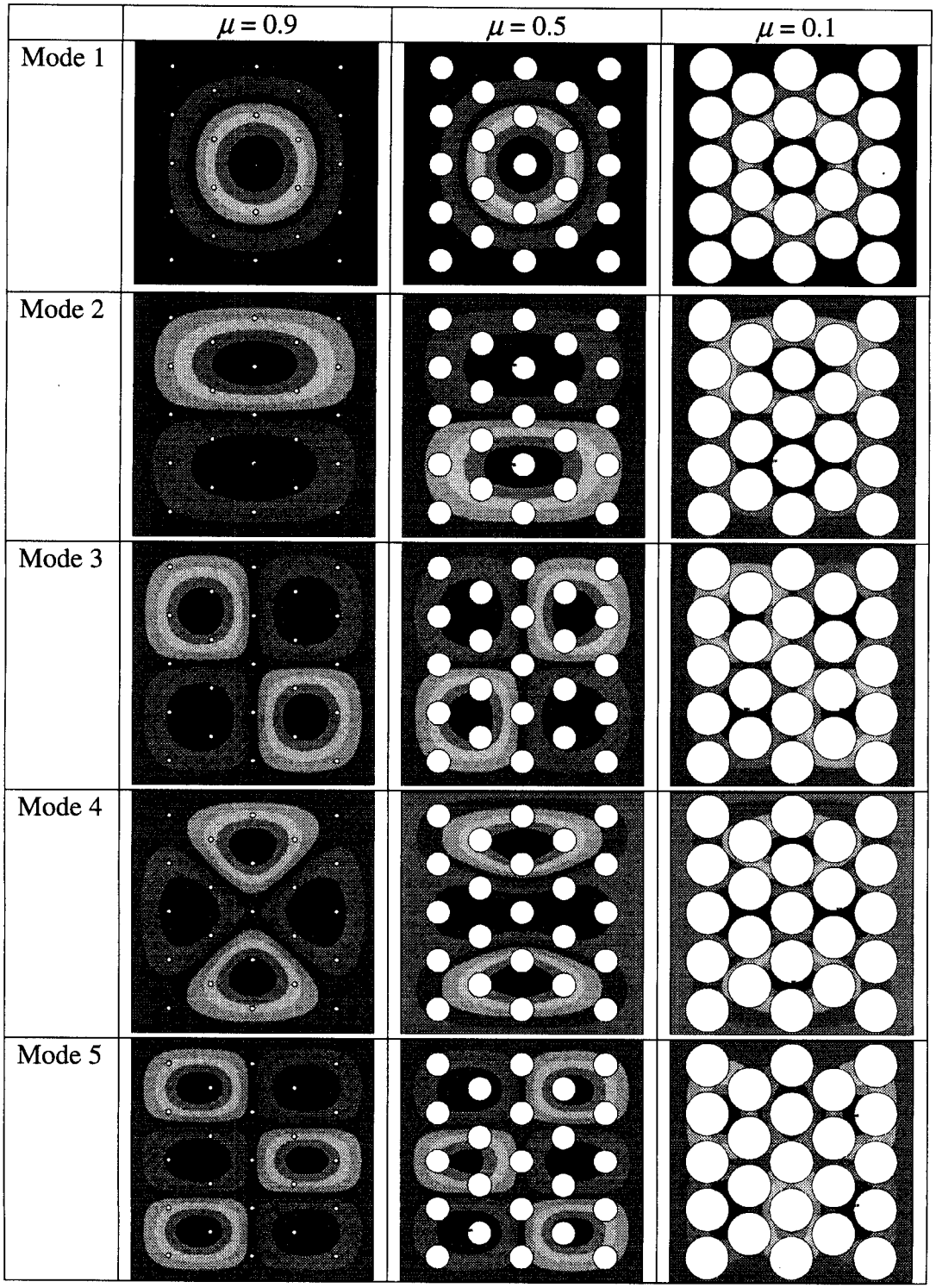


Fig. 5.22. ANSYS® output for clamped plates with triangular perforation patterns ($P = 2.0$, $\upsilon = 0.20$).

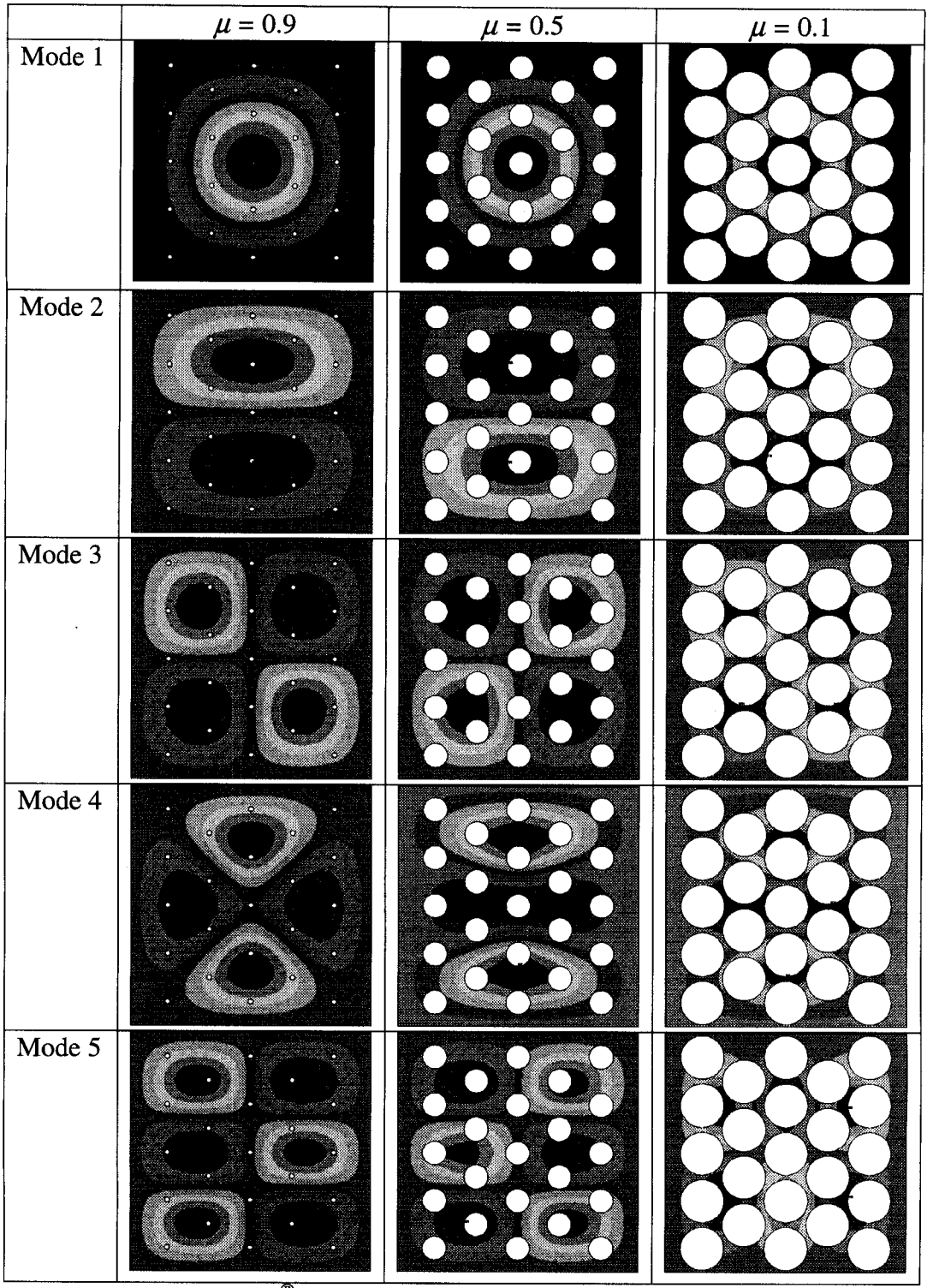


Fig. 5.23. ANSYS® output for clamped plates with triangular perforation patterns ($P = 2.0$, $\nu = 0.30$).

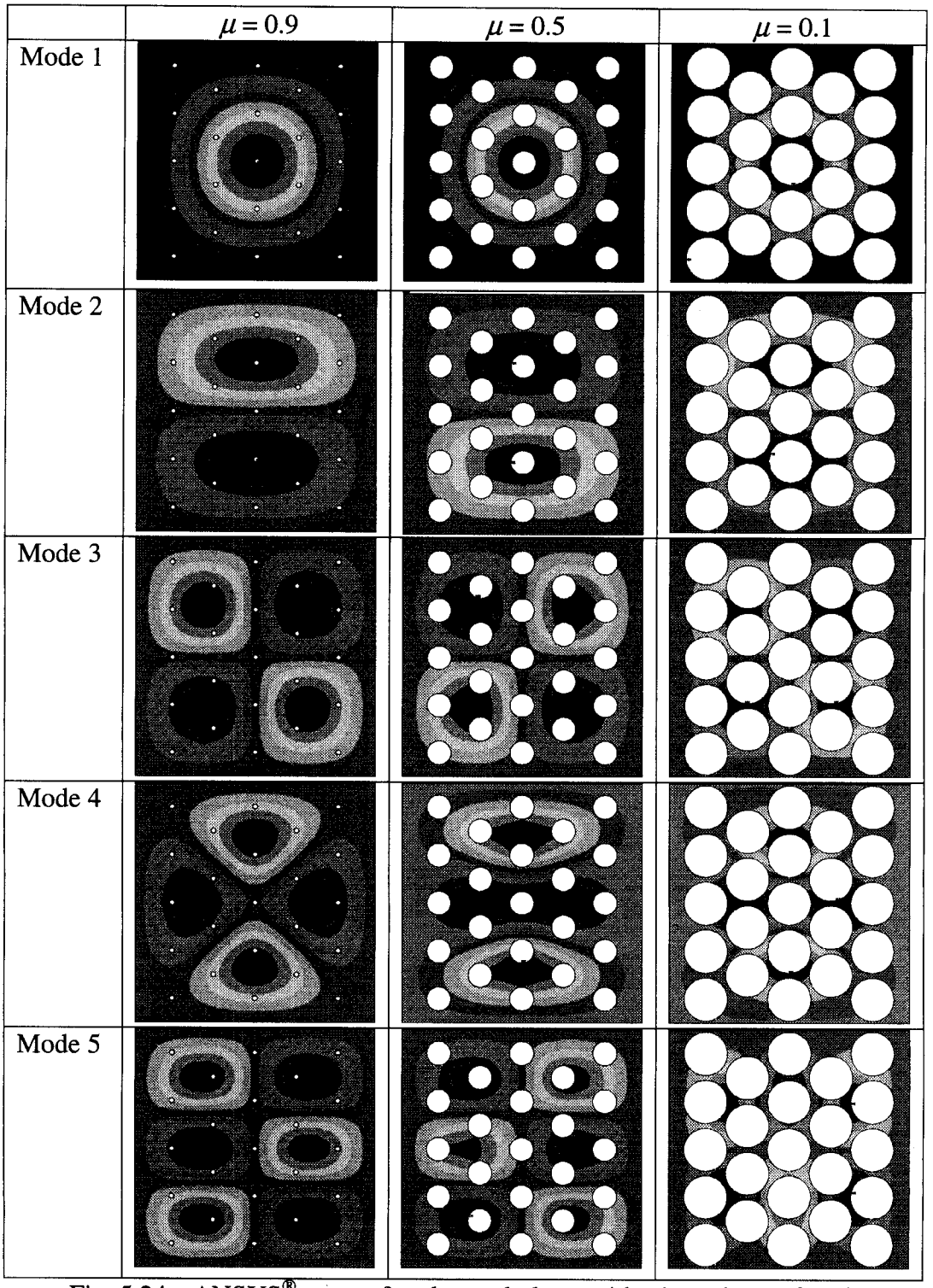


Fig. 5.24. ANSYS® output for clamped plates with triangular perforation patterns ($P = 2.0$, $\nu = 0.45$).

## 5.2 Poisson's Ratio

Dynamic effective stiffness is a function of Poisson's ratio and the sensitivity to Poisson's ratio is a function of boundary conditions. To show this, different configurations were analyzed, each with a different Poisson's ratio (Figs. 5.25 – 5.28). The resulting data is based on the fundamental frequency data for mode 1,1. Other modes were not considered.

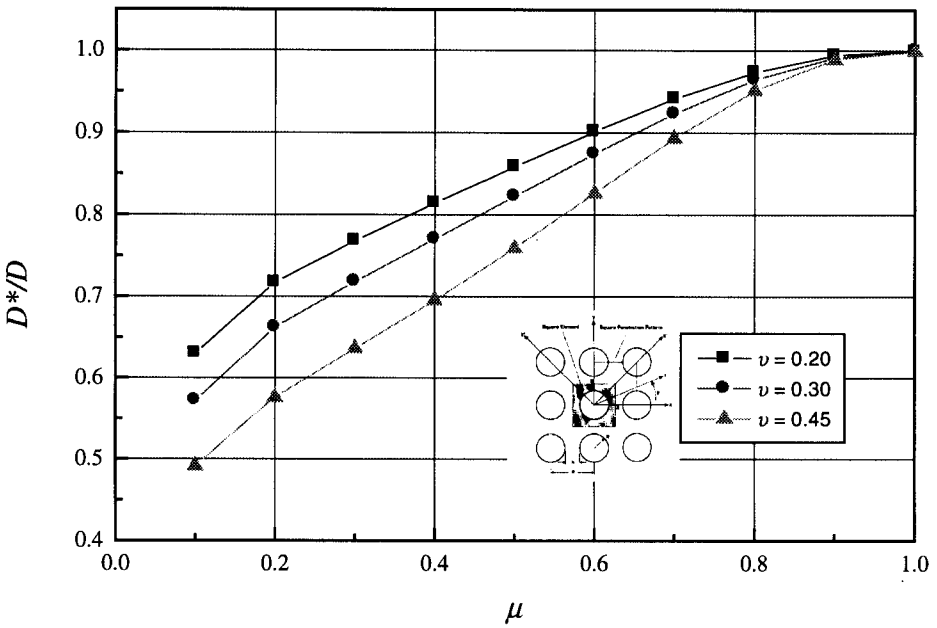


Fig. 5.25. Effective stiffnesses based upon the fundamental frequencies for simply supported square plates with square perforation patterns.

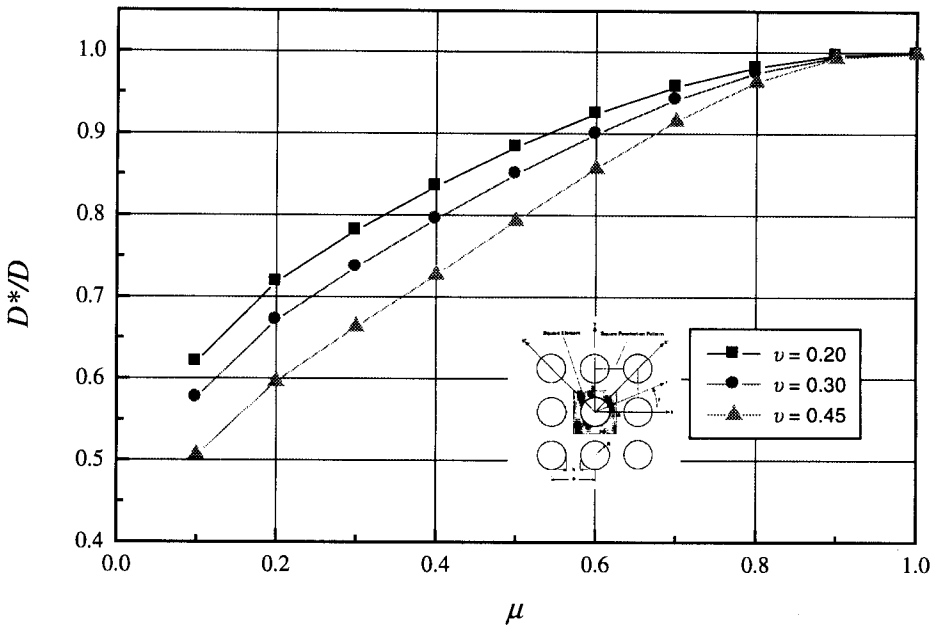


Fig. 5.26. Effective stiffnesses based upon the fundamental frequencies for clamped square plates with square perforation patterns.

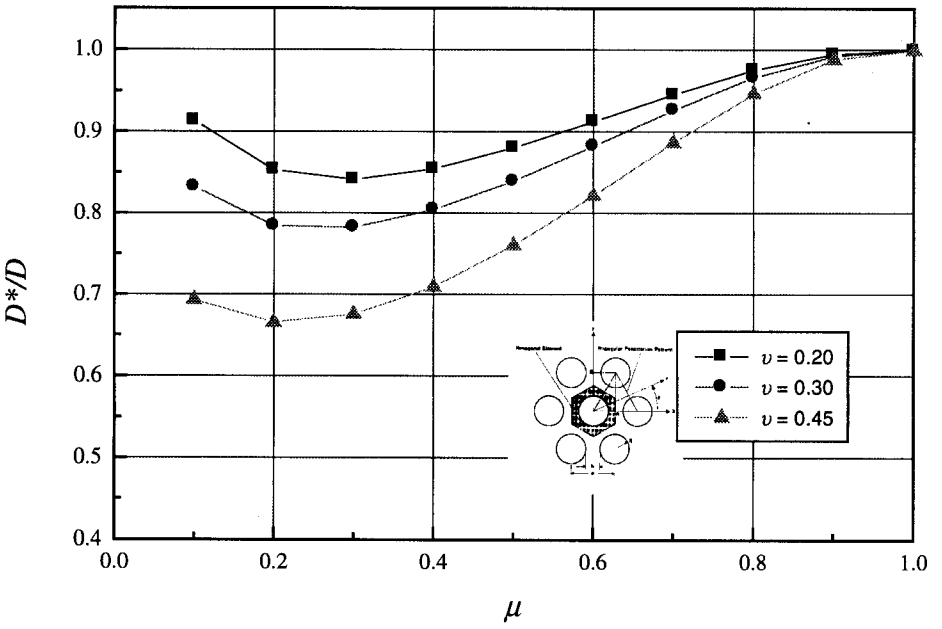


Fig. 5.27. Effective stiffnesses based upon the fundamental frequencies for simply supported square plates with triangular perforation patterns.

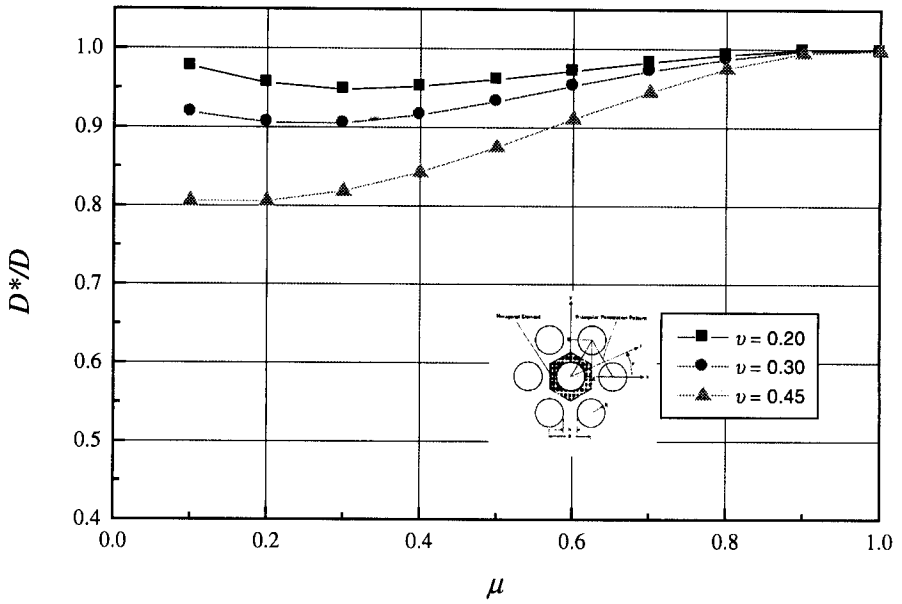


Fig. 5.28. Effective stiffnesses based upon the fundamental frequencies for clamped square plates with triangular perforation patterns.

## 5.3 Number of Perforations

All FE models were based on 23, or 25-hole penetration patterns depending on whether the pattern was triangular or square. The number of holes was assumed large enough to approximate an infinitely perforated plate. To verify this, the number of holes was varied with all other parameters held constant. Results are shown in Figure 5.29.

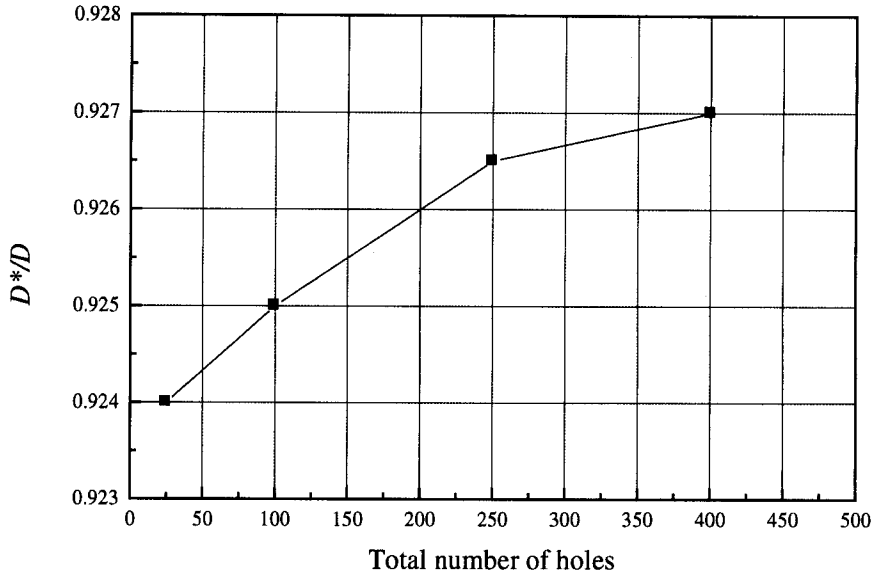


Fig. 5.29. Sensitivity of effective stiffness for fundamental mode to number of holes for a clamped perforated square plate with a square perforation pattern ($\nu = 0.30$, $\mu = 0.70$).

## 5.4 Plate Thickness

All FE models were based on plates having a 0.125-in. thickness. This thickness was chosen because a thin plate was desired. It was assumed that any thickness within the thin plate region, $\frac{t}{b} \leq \frac{1}{20}$, would yield the same results. To verify this assumption the thickness was varied with all other parameters held constant. Results show that the effective stiffness is not a function of the plate thickness within this thin plate region (see Table 5.1).

Table 5.1. Sensitivity of fundamental mode to plate thickness for a clamped perforated square plate with a square perforation pattern ($\nu = 0.3$, $\mu = 0.7$).

| Thickness $t$ [in] | $t/P$ | $t/b$ | Fundamental Frequency [Hz] | $D^*/D$ |
|---|---|---|---|---|
| 0.0625 | 0.03125 | 0.00625 | 114.88 | 0.926 |
| 0.125 | 0.625 | 0.0125 | 229.77 | 0.926 |
| 0.25 | 0.125 | 0.025 | 459.53 | 0.926 |
| 0.5 | 0.25 | 0.05 | 919.06 | 0.926 |

## 5.5 Material Density

All FE models were based on plates having a density of 0.000744 lb-s$^2$/in$^4$ [5.2]. The dynamic stiffness values, however, were assumed to be independent of material density. To verify this assumption, the density, $\rho$, was varied with all other parameters held constant. Results show that the effective stiffness is not a function of the material density (see Figs. 5.30 and 5.31).

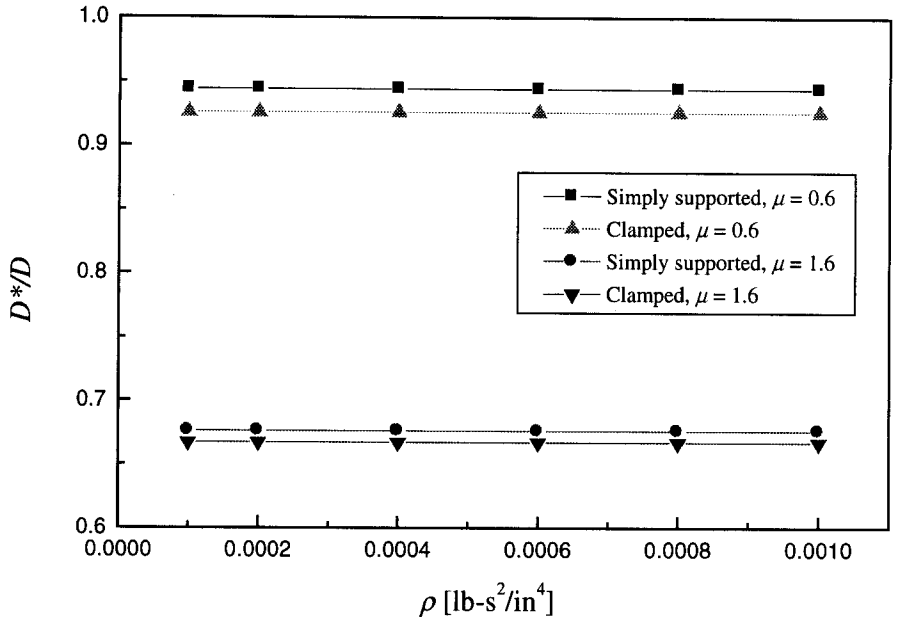


Fig. 5.30. Effective stiffness sensitivity to material density for fundamental mode of a plate with a square perforation pattern ($\nu = 0.30$, $\mu = 0.70$).

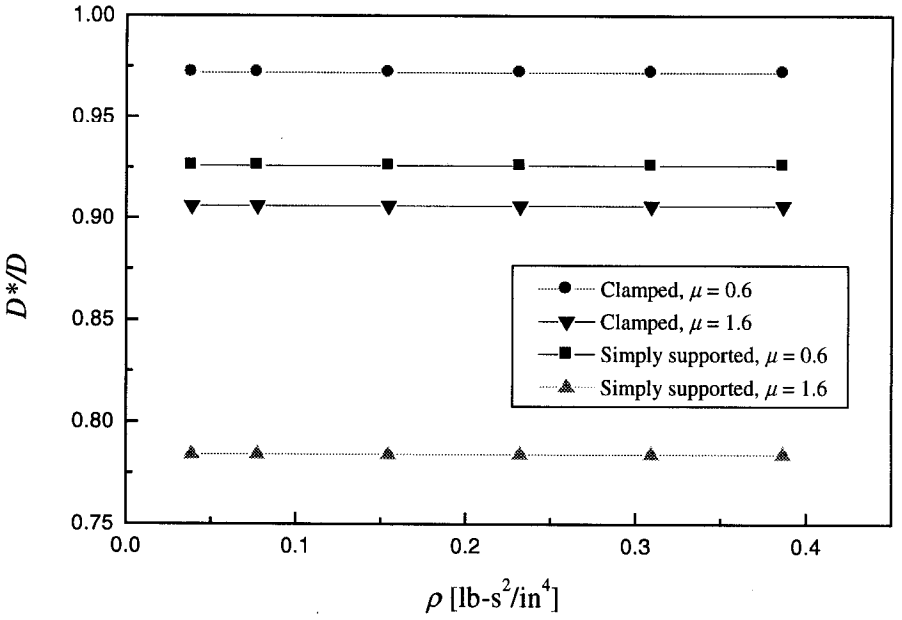


Fig. 5.31. Effective stiffness sensitivity to material density for fundamental mode of a plate with a triangular perforation pattern ($\nu = 0.30$, $\mu = 0.70$).

## 5.6 References

[5.1] ANSYS® Engineering Analysis Systems User's Manual, Houston, PA, Rev. 5.3, 1996.

[5.2] *ASM Specialty Handbook® - Aluminum and Aluminum*, ASM International, Materials Park, OH, pp. 685-686, 1993.

# Chapter 6
# Experimental Work

Chapter 5 describes the use of FE models to determine the dynamic effective stiffness of various thin plates perforated with square or triangular penetration patterns. The effective stiffness values were generated using, in addition to other constant parameters, the frequency data taken from a modal analysis. The results differ from previously developed effective material constants, presumably, because FE results are based on a dynamic analysis rather than a static analysis. To verify these results, an experimental investigation was carried out.

## 6.1 Plate Specimens and Plate Fixture

The FE work described in Chapter 5 employed many different plate configurations, yet each model had a number of common parameters. For example, the plates all had the same overall dimensions of 10 in. × 10 in. × 0.125 in. They also had variable perforation patterns, boundary conditions, and Poisson's ratios. The experimental work did not encompass the full range of parameters. To reduce the amount of work, all tests were done with 10 in. × 10 in. × 0.125 in. clamped plates made of 6061-T6 aluminum (see Table 4.2). The ligament efficiency and penetration pattern were the only experimental parameters that were varied (see Table 6.1).

A clamping fixture, also made of 6061-T6 aluminum, was designed to enforce the boundary conditions. Clamped boundary conditions were chosen because they could be replicated more easily and more accurately than simply supported boundary conditions. In addition to enforcing boundary conditions, the fixture served as an adapter between the plate and the experimental equipment. As an integral part of the dynamic tests, the fixture had to be made stiff enough so as to not exhibit any modes

of vibration under 2000 Hertz, the range of plate frequencies being studied. As an additional point of reference, the fixture was mounted onto an 1100-pound electromagnetic shaker for all tests.

Table 6.1. Experimental test specimens using 6061-T6 aluminum (geometric and material properties listed in Table 4.2) with clamped boundary conditions.

| Specimen Number | Perforation Pattern | Perforation Diameter, in. | Ligament Efficiency, $\mu$ |
|---|---|---|---|
| 0 | Solid plate | 0.0 | 1.0 |
| 1 | Square | 0.4 | 0.8 |
| 2 | Square | 0.8 | 0.6 |
| 3 | Square | 1.2 | 0.4 |
| 4 | Square | 1.6 | 0.2 |
| 5 | Square | 1.8 | 0.1 |
| 6 | Triangular | 0.4 | 0.8 |
| 7 | Triangular | 0.8 | 0.6 |
| 8 | Triangular | 1.2 | 0.4 |
| 9 | Triangular | 1.6 | 0.2 |
| 10 | Triangular | 1.8 | 0.1 |

Accurately manufacturing perforated plate specimens was a concern because the size and location of the holes were the only parameters varied. To achieve the desired degree of accuracy, the plates and fixturing were modeled and manufactured using computer technology. The solid modeling was done with the software ProEngineer® [6.1]. The model geometry was then converted to G-N code using the software EZ-mill [6.2], and finally, the code was loaded into a computer numerically controlled horizontal mill [6.3] (Fig. 6.1). This allowed for very tight tolerances and holes that were extremely accurate, both in placement and circularity (see Figs. 6.2, 6.3 and 6.4).

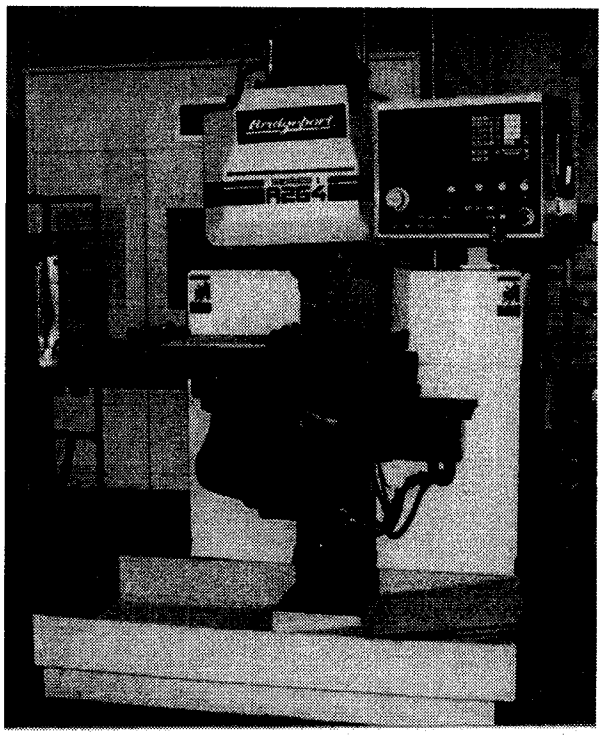


Fig. 6.1. Photograph of Bridgeport® R2G4 CNC horizontal mill.

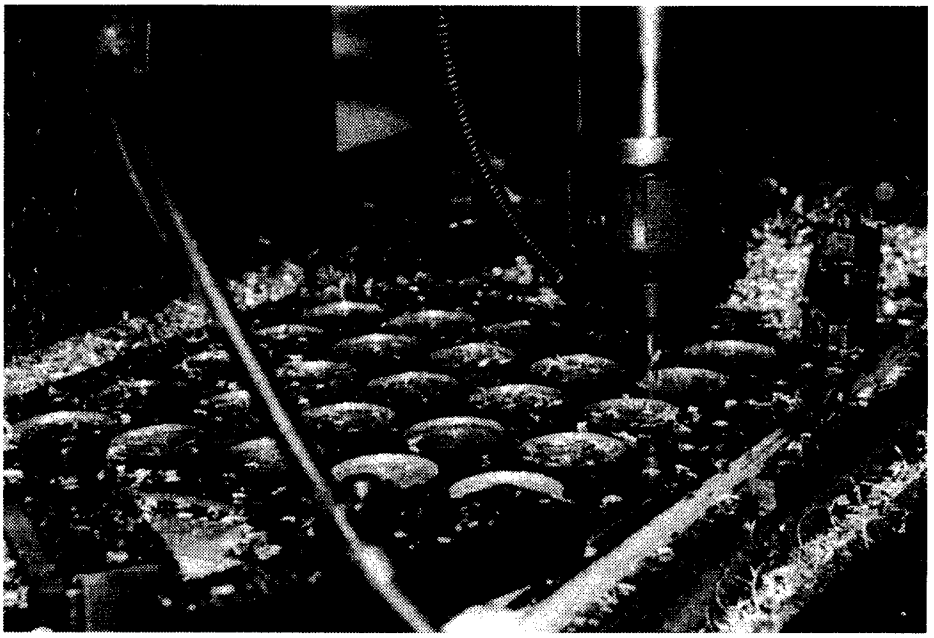

Fig. 6.2. Photograph of CNC mill cutting 1.6 in. holes in a square pattern.

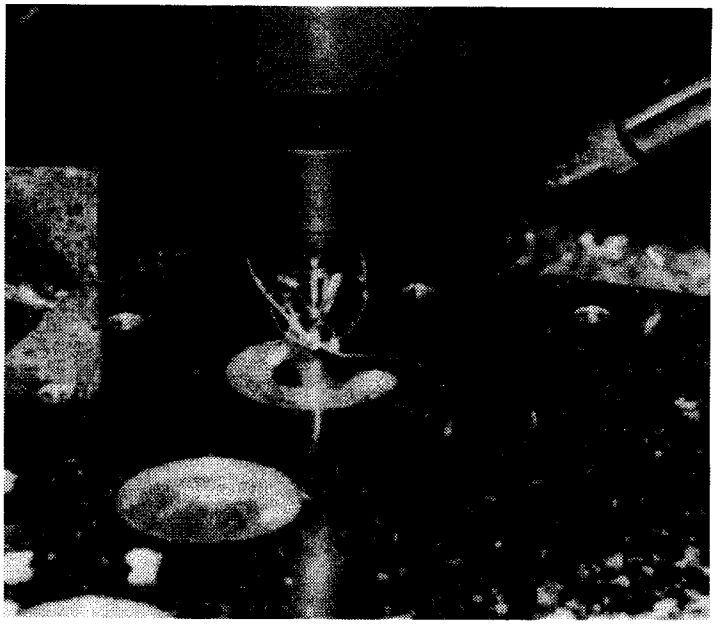

Fig. 6.3. Photograph of CNC mill using circular interpolation to cut an accurate perforation pattern.

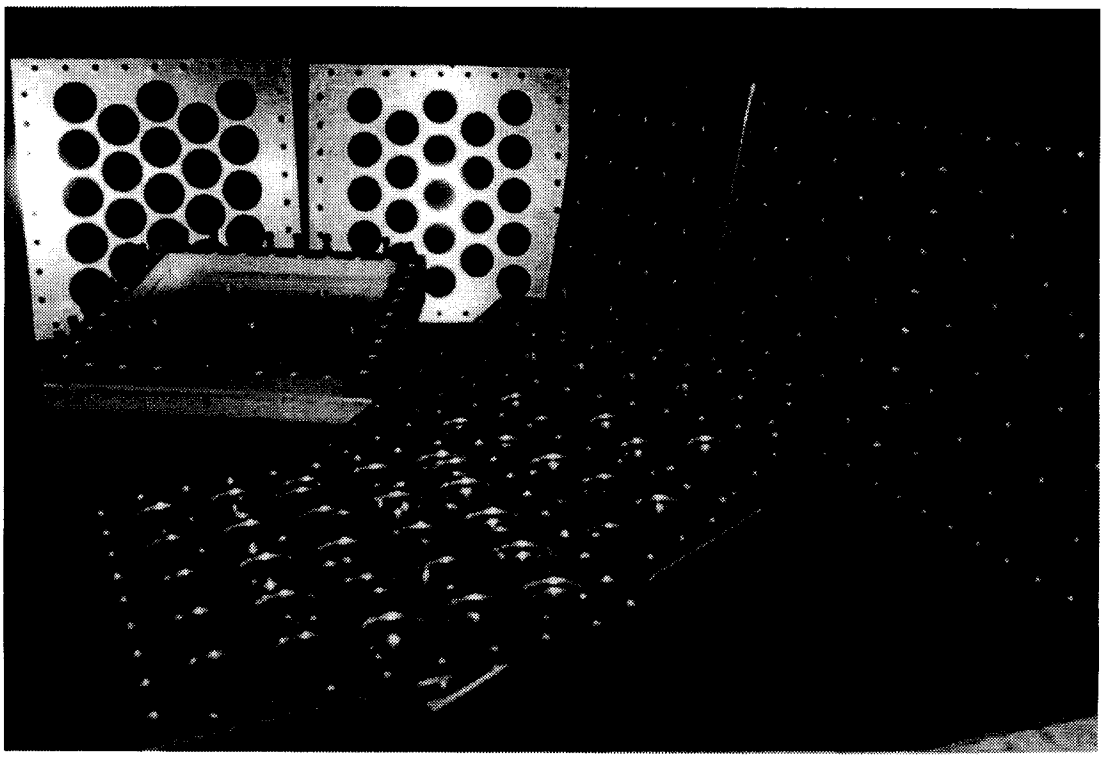

Fig. 6.4. Photograph of experimental specimens and clamping fixture.

## 6.2 Procedure for Impulse Testing

A number of resonant frequencies can be excited within a structure by applying an impulse. The range of frequencies that are excited depends on the amount of energy transferred to the structure, e.g., the type of hammer used and the duration of the pulse. In this study these parameters were adjusted to excite frequencies under 2000 Hertz.

An accelerometer, fixed to the structure with wax, recorded the structure's response to the impulse. Both the impulse and the accelerometer were orientated in the z-direction (perpendicular to the plate's surface). The data acquisition software SnapMaster [6.4] was then used to collect the data and convert it into the frequency domain using a Fast Fourier Transform (FFT). The equipment used for the impulse testing is listed in Table 6.2. Figure 6.5 shows a schematic of the experimental apparatus, while Figs. 6.6 shows a photograph of the actual setup.

Table 6.2. List of experimental equipment for impact tests.

| | |
|---|---|
| Computer | Pentium PC – 133 MHz |
| Data Acquisition Software | HEM – SNAPMASTER |
| Signal Conditioner/ Power Amplifier | Kistler Model 5128A |
| Digital/Analog Converter | IOTECH DAQBOOK 100 |
| Accelerometers | Kistler Piezomeam Model 8632C50 |

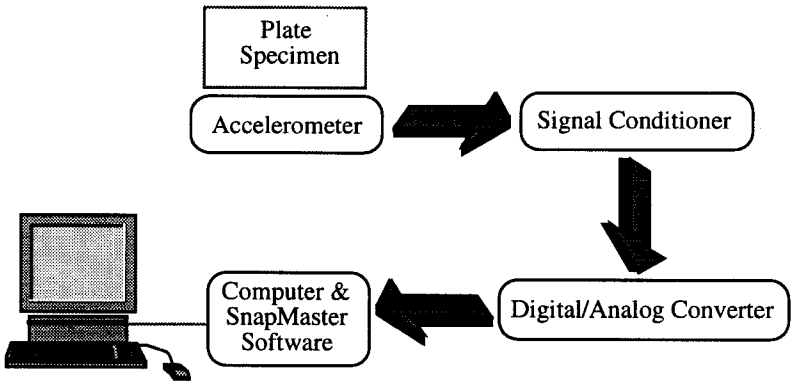

Fig. 6.5. Schematic of impact analysis setup.

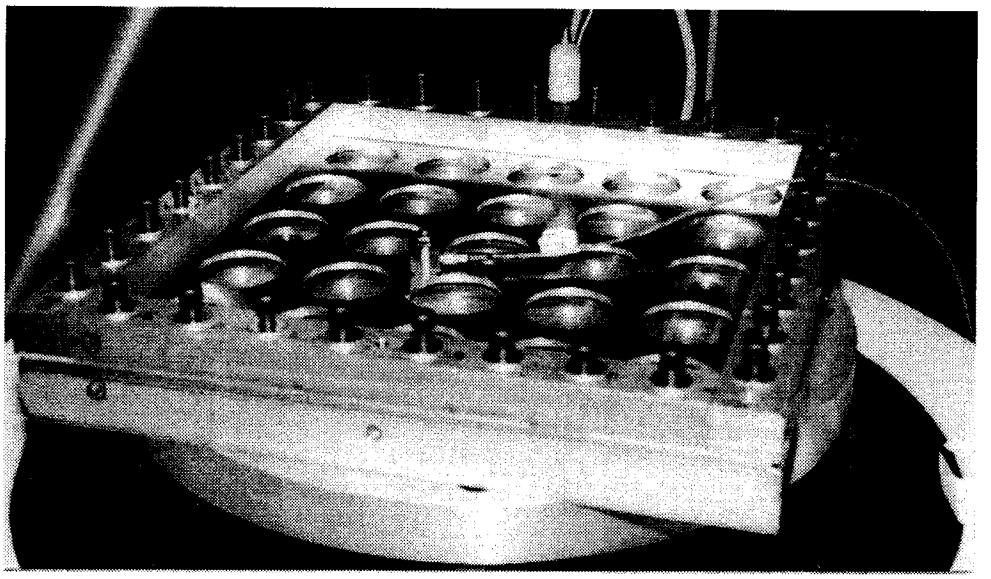

Fig. 6.6. Photograph of a perforated plate, clamped in the fixture, with an accelerometer attached.

## 6.3 Procedure for Optical Vibrometer Testing

Laser Doppler vibration sensing is a technique used to conduct non-destructive, non-contacting vibration measurements. When the laser is positioned normal to the vibrating surface it acts as an acceleration transducer, providing an analogue output directly comparable to that obtained from a conventional accelerometer charge-amplifier combination. In addition to single point data collection, full-field vibration patters (mode shapes) can be obtained by combining a laser Doppler vibration sensor, a beam scanning mechanism with signal processing and display system, and a central computer.

The Polytec® vibrometer system utilizes a single-beam backscatter arrangement based on the well-known Mach-Zehnder Interferometer [6.5]. The beam from the laser source is divided into an internal reference beam and an external measuring beam, the

latter being directed onto the moving test surface. Light that is reflected back from the test surface is shifted in frequency. This frequency change is known as the Doppler shift and although the shift in light from the test specimen is very small (typically 1 part in $10^8$ or less) it can be measured very accurately using optical interferometry. Optical interferometry enables the measurement of displacements much smaller than the wavelength of light by exploiting the sinusoidal relationship between the output of an interferometer and the difference in optical path lengths traversed by its beams.

Two different vibration measurement tests were run with the Polytec® optical vibrometer. First, impulse tests were run to verify the impulse testing described in Section 6.2. For these tests the Polytec® optical sensor and data acquisition system replaced the accelerometer and SnapMaster® software which were used previously. In addition to the impulse tests a series of forced vibration tests were performed with the 1100-pound electromagnetic shaker. By exciting the plate with a constant sinusoidal input while at the same time scanning the surface of the plate with the laser, mode shapes were generated graphically on the computer. The equipment used for the mode shape tests is shown in Table 6.3. Figure 6.7 shows a schematic of the experimental setup, while Fig. 6.8 shows photographs of the actual setup.

Table 6.3. List of experimental equipment for optical tests.

| | |
|---|---|
| Shaker | V830-335T air-cooled vibrometer by Ling Dynamic Systems LTD |
| Power Amplifier | SPA10K power amplifier by Ling Dynamic Systems, LTD |
| Shaker Control Software | Data Physics version 2.3 |
| Data Acquisition System | Polytec GmbH Optical Scanning Vibrometer, version 5.13a |

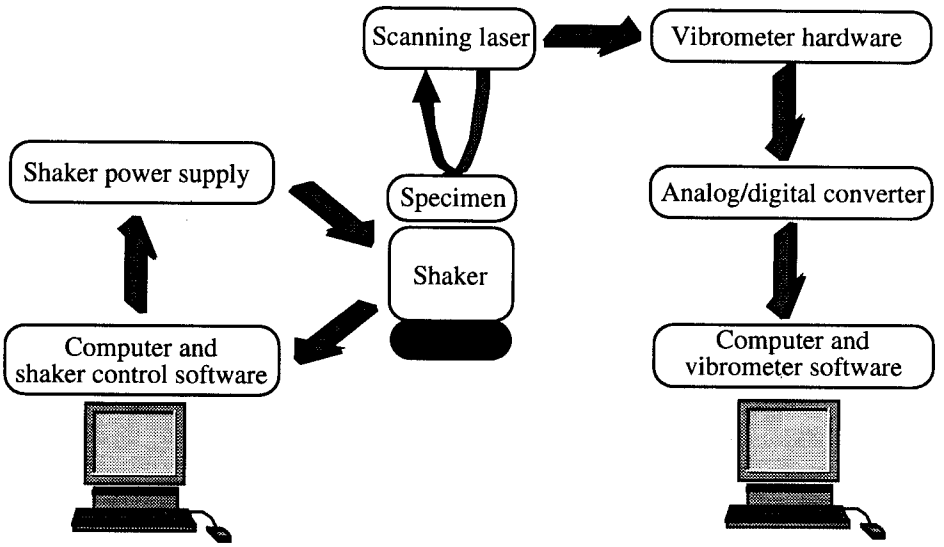


Fig. 6.7. Schematic of experimental modal analysis setup.

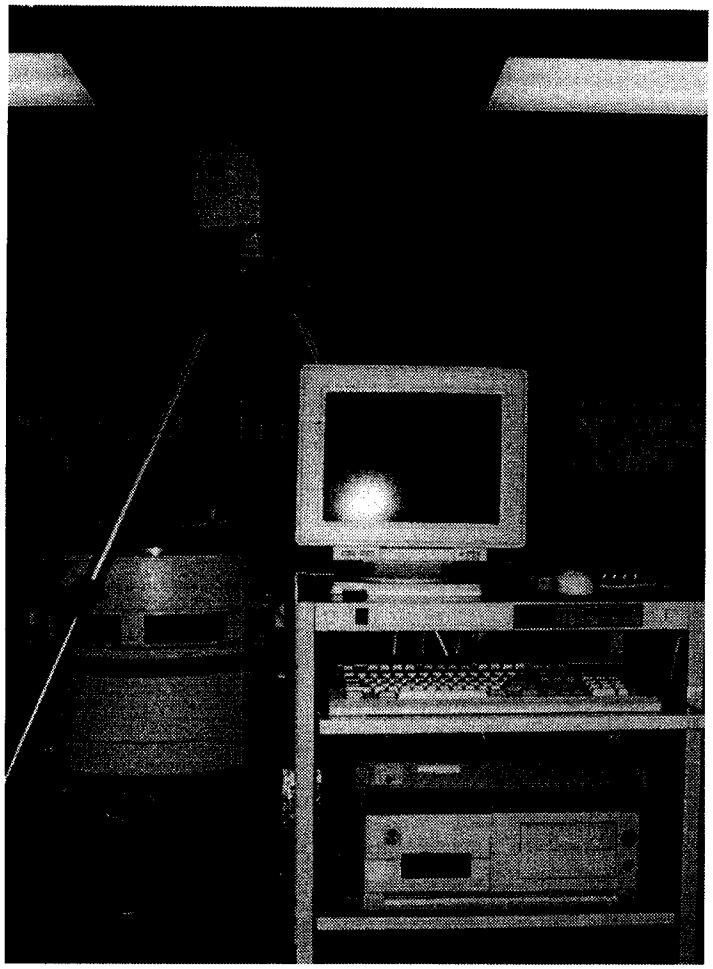

Fig. 6.8. Photograph of laser vibrometer test setup.

## 6.4 Resonant Frequency Results

Impulse tests were run with two different testing configurations. One test measured the plate's response with an accelerometer fixed to the plate's surface while the other test measured response via an optical sensor. Figures 6.9 and 6.10 show the results for the fundamental mode after being transformed to effective stiffness. Figures 6.11 and 6.12 compare FEM results to the experimental results. Figures 6.13 and 6.14 FEM effective stiffness results for the first two modes. The contents of Tables 6.4 and 6.5 summarize frequency results for the solid plate.

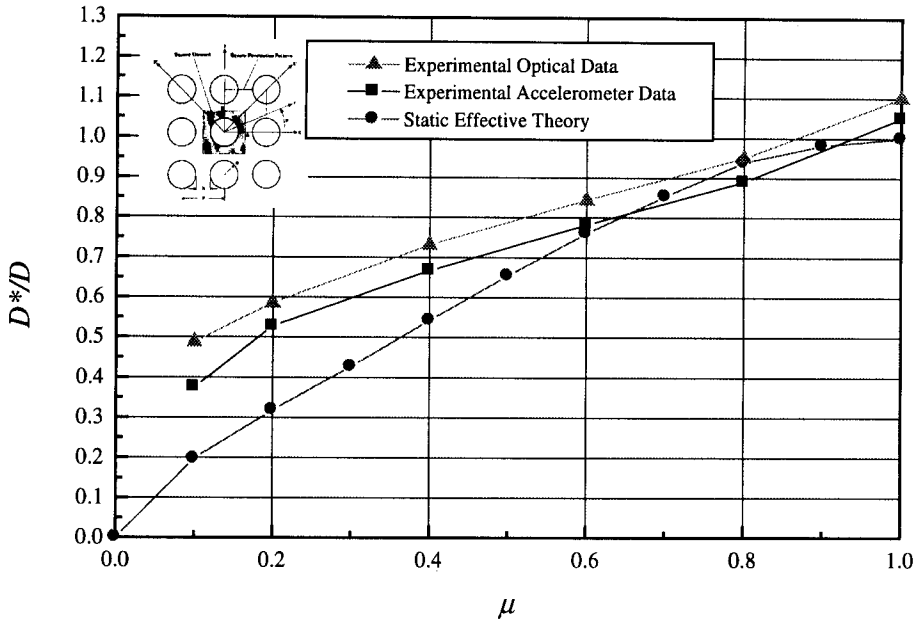


Fig. 6.9. Comparison of dynamic and static effective stiffnesses for clamped plates with square perforation patterns. Experimental data is based upon the fundamental frequency.

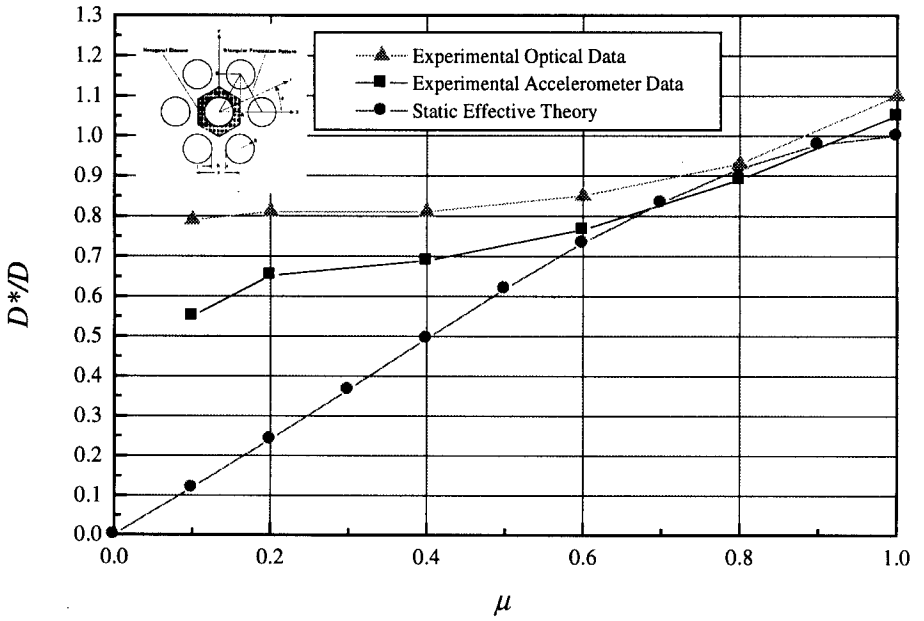


Fig. 6.10. Comparison of dynamic and static effective stiffnesses for clamped plates with triangular perforation patterns. Experimental data is based upon the fundamental frequency.

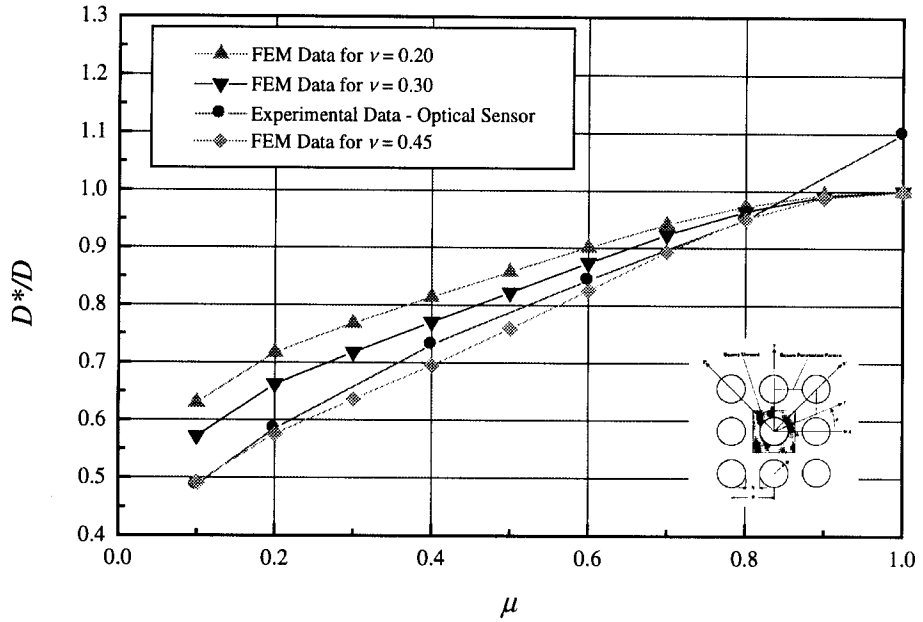


Fig. 6.11. Experimental and FEM dynamic effective stiffness results for the fundamental mode of clamped plates with square perforation patterns.

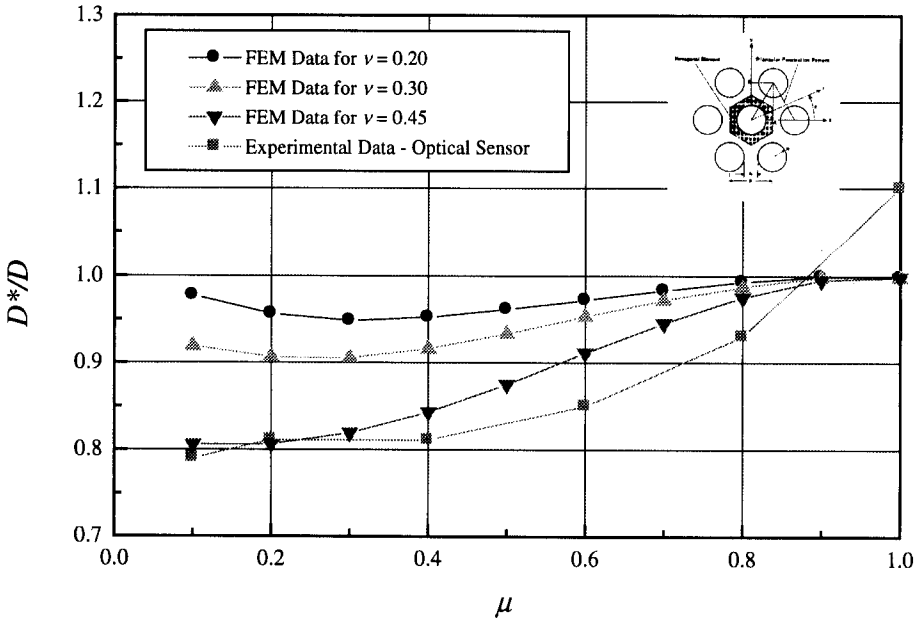


Fig. 6.12. Experimental and FEM dynamic effective stiffness results for the fundamental mode of clamped plates with triangular perforation patterns.

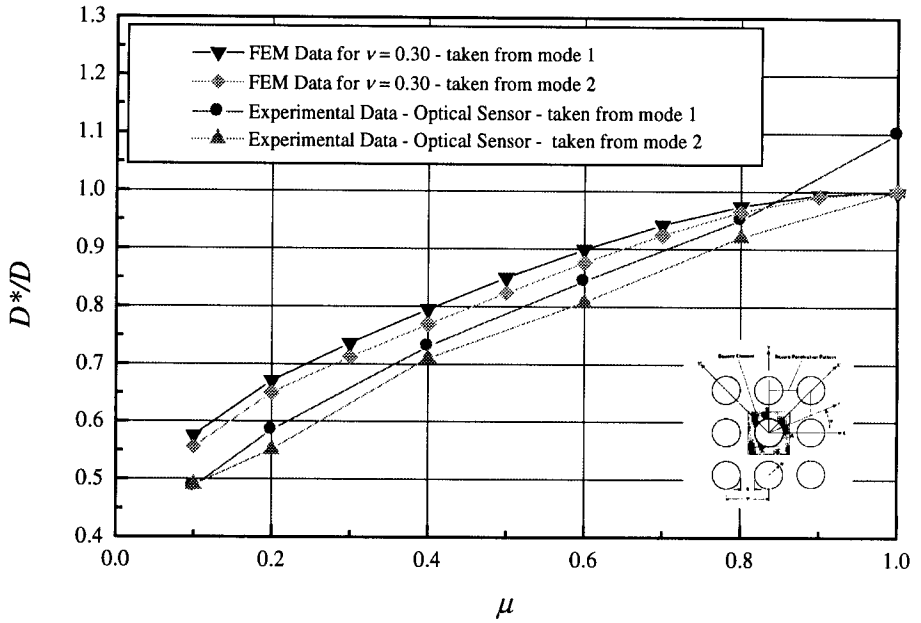


Fig. 6.13. Experimental and FEM dynamic effective stiffness results for the first two modes of a clamped plate with square perforation pattern.

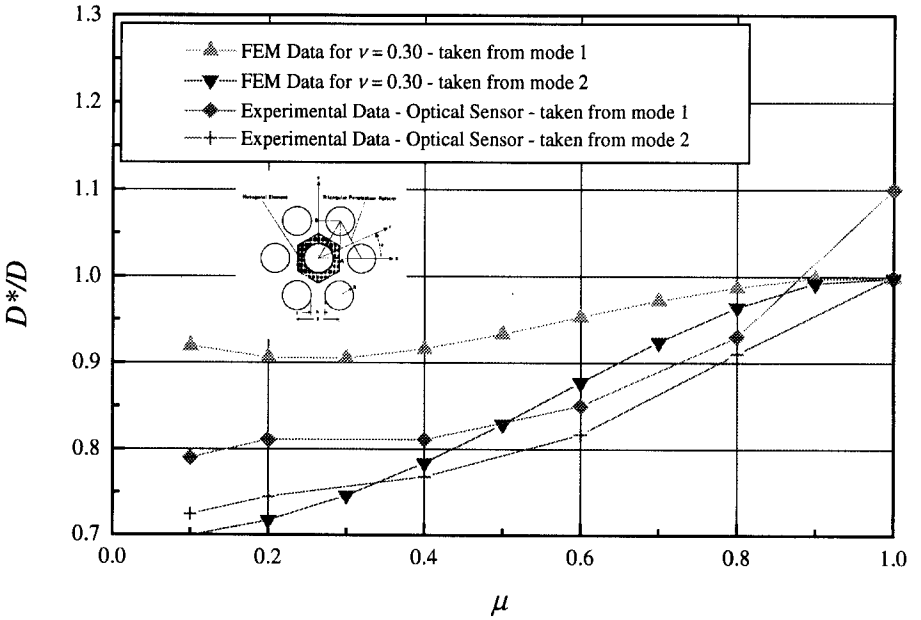


Fig. 6.14. Experimental and FEM dynamic effective stiffness results for the first two modes of a clamped plate with triangular perforation pattern.

Table 6.4. Fundamental frequency data for a clamped solid plate.

| Source | Fundamental frequency [Hz] |
|---|---|
| Classical plate theory | 432.8 |
| FEA | 432.0 |
| Experimental – accelerometer | 442.0 |
| Experimental – optical | 465.2 |

Table 6.5. Mode 2 (1,2) frequency data for a clamped solid plate.

| Source | Fundamental frequency [Hz] |
|---|---|
| Classical plate theory | 878.2 |
| FEA | 880.1 |
| Experimental – accelerometer | 853.5 |
| Experimental – optical | 880.0 |

## 6.5 Mode Shape Results

Mode shapes graphically illustrate the relative displacement of a structure at a specific frequency. The laser scanning system uses the Doppler effect to measure the relative acceleration of a number of different points on the plate, and thus, it is able to construct mode shape diagrams. The mode shapes of the experimental plate specimens correlated very well with the predicted FEA mode shapes. Because they were so similar only one experimentally scanned mode shape has been included. Figure 6.15 shows a scanned image for mode 2 (1,2). The image is applicable for every test specimen listed in Table 6.1.

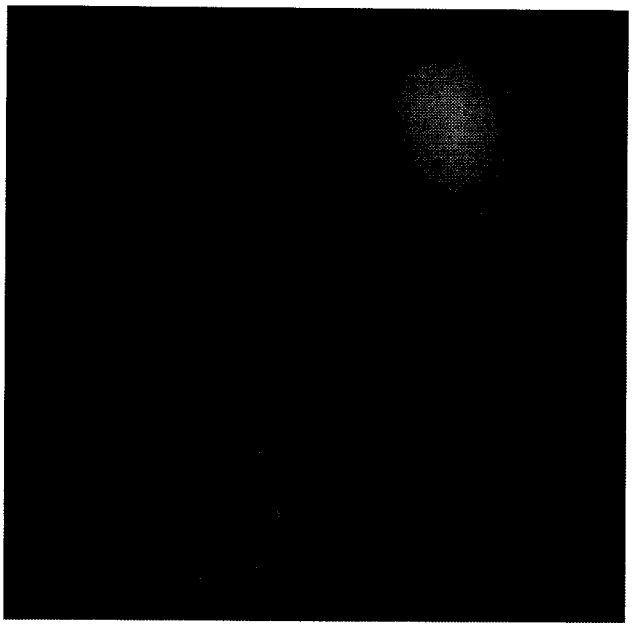

Fig. 6.15 Experimentally scanned mode shape for all clamped square plates tested.

## 6.6 References

[6.1] ProEngineer® User's Guide, Rev. 14, Parametric Technology Corporation, Waltham, MA, 1996.

[6.2] EZ-Mill, EZ-CAM package, Version 6.2.1, Bridgeport Machines, Inc., Bridgeport, CT, 1994.

[6.3] R2G4 3-axis CNC Vertical Mill with Fanuc 11MA controller, Bridgeport Machines, Inc., Bridgeport, CT, 1994.

[6.4] SnapMaster User's Guide, HEM Data, Southfield, MI, 1997.

[6.5] Operator's Manual for Polytec Scanning Vibrometer PSV-200, Software vs. 5.0, Polytec GmbH, Waldbronn, Germany, Chapter 5, 1997.

# Chapter 7
# Summary and Conclusions

The vibration characteristics of perforated plates are important when designing structures where resonance or fatigue are possible modes of failure. A literature review of methods for predicting perforated plate vibrations showed that no design curves for this analysis have been developed. Essentially, there are no analytical, numerical, or experimental data available which would enable a designer to predict dynamic response of perforated plates.

Two areas of study, indirectly related to perforated plate vibrations, have previously addressed the structural changes from perforations. They are (a) the effective elastic constants developed with either static deflection equations or experimental data and (b) the vibration characteristics of square plates with a single circular hole located at the center of the plate. Published results in these two areas cannot be accurately applied to the vibration of uniformly perforated plates.

For this thesis, finite element models were developed to determine the natural frequencies and mode shapes of perforated plates. In order to approximate an infinitely perforated plate a large number of perforations were used. Two basic models were then developed – one with a square penetration pattern and the other with a triangular pattern. Adjusting parameters on these models, such as boundary conditions and ligament efficiency, was computationally straightforward and thus this method of analysis was very effective.

Previous investigations on single-hole plates suggested that as ligament efficiency increases, the frequency of a perforated plate would decrease until a critical point was reached. At this critical point, the frequency would begin to increase as ligament

efficiency continued to increase. This two-fold mechanism of mass reduction and kinetic energy reduction (described in previous literature as strain energy reduction) was seen in the FEA results for plates with a triangular penetration pattern, but not for plates with a square penetration pattern.

Static effective elastic constants taken from the CODAP code did not correlate with the FEA results. In particular, there was a difference in effective stiffness values that quickly increased with decreasing ligament efficiency, reaching errors of about 100% at a ligament efficiency of 0.01.

The effects of other material properties were also investigated. Results show that by decreasing Poisson's ratio, the effective stiffness values increase. The general trend, however, remains constant. Material density, on the other hand, has no effect on the dynamic effective stiffness.

Experimental frequency data did support FEM results, especially at higher modes. However, the fundamental mode was a special case. As seen by the shifts in experimentally scanned mode shapes, the fundamental frequency of an experimental plate was very sensitive to boundary conditions.

Perforated plate mode shapes are essentially independent of perforation size and type. The analytical shapes determined from classical plate theory apply to all the perforated plates examined. The only effect the perforations have on the dynamic characteristics is via structural frequency change. Knowing this, it should be possible to predict the frequency of each mode for all perforated plates. This is an important first step toward understanding more complex problems where either the perforation pattern does not cover the entire structure, the holes are not circular, or the structure has curvature, such as a shell.